ABSTRACT

Title of Document: POLYMER BASED MINIATURE FABRY-PEROT PRESSURE SENSORS WITH TEMPERATURE COMPENSATION: MODELING, FABRICATION, AND EXPERIMENTAL STUDIES

Hyungdae Bae, Doctor of Philosophy, 2013

Directed By: Professor Miao Yu
Department of Mechanical Engineering

Miniature Fabry-Perot (FP) pressure sensors have been of great interest because of their advantages of small sizes, high performance, and immunity to electromagnetic interference. Most of these sensors are built with silicon/silica materials that have good mechanical, chemical, and thermal stabilities. However, due to the large Young's modulus of silica/silicon, developing a high sensitivity miniature sensor becomes difficult. In addition, fabrication of these sensors often involves high temperature fusion bonding and harsh acid etching. On the other hand, a polymer material becomes an attractive choice for high sensitive and miniature pressure sensors due to its small Young's modulus relative to that of silicon/glass. Moreover, polymer processes can be performed under ambient pressure and temperature without hazardous chemicals. However, a polymer-based sensor suffers from high temperature sensitivity, which must be compensated to obtain accurate pressure measurements.

In this dissertation, three types of polymer based FP miniature sensors for static or quasi-static pressure measurements are investigated through modeling, microfabrication, and experiments. First, co-axial and cross-axial FP sensors with a built-in fiber Bragg grating (FBG) for temperature measurement and compensation are studied. In both sensors, the FP cavity is precisely self-aligned with the optical axis by using the fiber as a natural mask, which eliminates the need for a photo mask and tedious optical alignments. Second, a FP sensor composed of a UV-molded optical cavity with a pre-written FBG is developed. For the first time, a UV molding process with an optical fiber based mold is developed for fabrication of miniature FP sensors. This process enables high accuracy optical alignment for UV molding. Taking advantage of the UV molding process, the third type of sensor features a hybrid dual FP cavity for simultaneous temperature and pressure measurements. A novel signal processing method is developed to retrieve the multiple cavity lengths with an improved speed, resolution, and noise resistance. Experimental studies show that these polymer based sensors have good pressure and temperature sensing performance as well as temperature compensation capabilities. In addition, blood pressure and intradiscal pressure measurements of a swine are performed, which demonstrates the feasibility of these sensors for biomedical applications.

POLYMER BASED MINIATURE FABRY-PEROT PRESSURE SENSORS WITH TEMPERATURE COMPENSATION: MODELING, FABRICATION, AND EXPERIMENTAL STUDIES

By

Hyungdae Bae

Dissertation submitted to the Faculty of the Graduate School of the
University of Maryland, College Park, in partial fulfillment
of the requirements for the degree of
Doctor of Philosophy
2013

Advisory Committee:
Associate Professor Miao Yu, Chair
Professor Balakumar Balachandran
Professor Bongtae Han
Associate Professor Teng Li
Associate Professor Adam H. Hsieh, Dean's Representative

Dedication

I lovingly dedicate this dissertation to my wife, parents, and parents-in-law, who supported me each step of the way.

Acknowledgements

Foremost, I wish to express my sincere gratitude to my advisor, Prof. Miao Yu, for her support for my Ph.D study and research. She has supported me with great patience, enhancing motivation, and in-depth knowledge for my research. It was such a great experience to do my Ph.D study under her supervision. Besides my advisor, I would like to thank the rest of my dissertation committee: Prof. Balakumar Balachandran, Prof. Bongtae Han, Prof. Teng Li, and Prof. Adam Hsieh for their insightful comments, helpful suggestions, and heartwarming encouragement. My research work has been greatly improved and enriched by all the helps and suggestions from them. I also thank my fellow labmates of the Sensors and Actuators Lab: Dr. Xuming Zhang, Dr. Yuxiang Liu, Dr. Haijun Liu, Dr. Cheng Pang, Felix Stief, Laith Sawaqed, Andrew Lisiewski, Zhijiang Zhang and Dr. Yongyao Cheng for their help, discussion, support, and friendship. My five years of study in the lab has been so meaningful and enjoyable because of them. I want to show my gratitude to intern students which worked with me: Laura Dunlap, James Wong, David Yun, Abisola Kusimo, and Syed Elahi for their help for my research work. Last but not the least, I really appreciate the support and encouragement of my wife, parents, and parents-in-law. If it were not for your help, I would never begin and go through my study.

Table of Contents

List of figures

Chapter 1 Introduction and Background

1.1 Problem of Interest

Miniature fiber-optic pressure sensors have become attractive choices for pressure monitoring in a confined space owing to their advantages of small size, high sensitivity, immunity to electromagnetic interference, and convenience of light guiding/detection through optical fibers [1,2]. These sensors usually exploit one of the following sensing mechanisms; i) extrinsic Fabry-Perot interferometry (EFPI) [3], ii) fiber Bragg grating (FBG) [4–9], and iii) surface plasmon or evanescent coupling [10–12]. Among the above sensing mechanisms, extrinsic EFPI is the most popular configuration for fiber-optic pressure sensors [13–30]. EFPI based pressure sensors have been widely applied to various applications, including biomedical (e.g., [31–35]), aerodynamic (e.g., [36–38]), acoustic (e.g. [39–42]), shock wave (e.g. [43–46]) and other industrial applications (e.g., [47–49]) where a minimal intrusiveness is required.

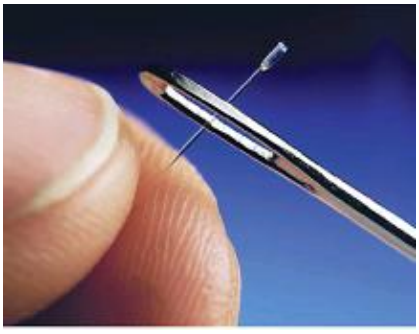

Figure 1.1: Commercially available fiber optic FP pressure sensor from FISO Technologies Inc. (http://www.fiso.com/).

A lot of research has been carried out to develop EFPI fiber-optic pressure sensors and some of these sensors are now commercially available (e.g., the miniature FP sensor from FISO Technologies Inc., as shown in Fig. 1.1). Most of these sensors make use of silica (or silicon) as the sensor housing structure material as well as the sensing diaphragm material [3,16,18,21–23,26,39,50–53]. Both glass and silicon materials have very good thermal/chemical stability, high elastic modulus, and relatively good biocompatibility. These inherent characteristics of the silica/silicon materials provide the sensors very good stability and reliability, especially, in harsh environments. However, the fabrication processes often use expensive equipment such as laser fusion bonding machine and involve dangerous etching processes such as hydrofluoric acid (HF) or potassium hydroxide (KOH) etching, making it difficult to fabricate these fiber optic sensors in batch, and thus, resulting in high manufacturing cost. In addition, the brittleness of the silicon and glass materials can hinder the applications of silica/silicon based sensors. For example, in biomedical applications, these sensors can be easily damaged while being inserted into or ejected out of a blood vessel or biological tissue.

On the other hand, there have been a few research groups working on design and fabrication of EFPI sensors based on polymer materials. Usually thermal and chemical stability as well as material strength of a polymer material is not as good as that of silica or silicon. However, there are a large variety of polymer materials that can be chosen according to specific requirement and application. For example, some polymer materials such as Polydimethylsiloxane (PDMS) or SU-8 has excellent

biocompatibility [54–56]. When polymers are used as the diaphragm material for a pressure sensor, the sensor can achieve much larger sensitivity than those made of silica or silicon because of the relatively low elastic modulus of the polymers. Furthermore, owing to the ductility of the polymer material, polymer based pressure sensors can endure large strain without failure and they cannot be easily damaged by a sudden pressure change or shock. A lamination of a thin metal film on a polymer substrate can increase rupture strain range even further [57]. Another advantage of polymer material is that the material properties of polymer such as mechanical strength, thermal/chemical resistivity, and optical property can be precisely designed and tuned to meet the system requirements. In addition, in the fabrication of polymer based sensors, high temperature process or hazardous chemicals are usually not involved, allowing for more eco-friendly processes. Since well-established semiconductor batch fabrication processes can be used, polymer based sensors can be fabricated with a low cost.

However, one of the most significant disadvantages of a polymer based pressure sensor structure is its large thermal expansion. The coefficient of thermal expansion (CTE) of polymer varies from 45 ppm/°C to 130 ppm/°C, which is about 5 to 15 times larger than that of glass. For a polymer based pressure sensor, this material property can result in large errors in pressure reading in a temperature varying environment. In order to obtain accurate pressure reading under temperature varying conditions, the temperature effect should be compensated properly [48,58–60].

This dissertation work is aimed to achieve an enhanced understanding of a polymer based miniature fiber-optic FP pressure sensor system for a static or quasistatic measurements including design, fabrication, and temperature compensation of the polymer based pressure sensors.

1.2 Literature Review

1.2.1 Fabry-Perot Interferometer

A Fabry-Perot interferometer (FPI) consists of two parallel mirrors facing each other and defining an optical cavity between them (Hodgson & Weber 1977). For simplicity, both mirrors are usually assumed to be flat and the incident light is to be normal to the mirrors. Monochromatic light entering the FPI with an intensity of I_0 or an electric field E_0 will be partially reflected from the first mirror. The partially transmitted light will then go through the optical cavity L and again partially reflected from the second mirror (Figure 1.2). If the reflection coefficients of the two mirrors are r_1, r_2, and the corresponding transmission coefficients are t_1, t_2, the reflected field E_r (or the transmitted field E_t) can be expressed by summating all the electric field components coming out from the first mirror (or transmitting through the second mirror) as

$$E_r = E_0\left[r_1 - t_1^2 r_2 \exp[\frac{i4\pi L}{\lambda}]\sum_{n=0}^{\infty}(r_1 r_2 \exp[\frac{i4\pi L}{\lambda}])^n \right], \tag{1.1}$$

$$E_t = -E_0 t_1 t_2 \exp[\frac{i2\pi L}{\lambda}]\sum_{n=0}^{\infty}(r_1 r_2 \exp[\frac{i4\pi L}{\lambda}])^n \tag{1.2}$$

where λ is the wavelength and L is the distance between the two mirrors.

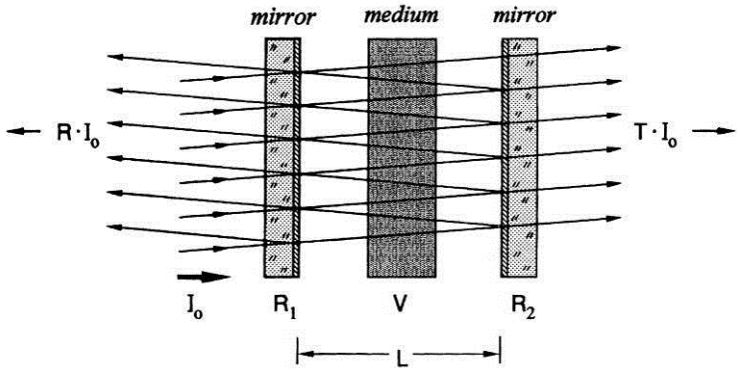

Figure 1.2: Plane-parallel FPI [61].

Based on equations (1.1) and (1.2), the intensity of the reflected and transmitted light can be derived. Furthermore, transmission T and reflection R as a function of the phase $2\pi L/\lambda$ can be calculated by obtaining the fraction of the reflected and transmitted intensity with respect to the incident intensity I_0. The calculated reflectance and transmission as a function of the phase are

$$R = \frac{[(\sqrt{R_1} - \sqrt{R_2})^2 + 4\sqrt{R_1 R_2}\sin^2(kL)]}{[(1 - \sqrt{R_1 R_2})^2 + 4\sqrt{R_1 R_2}\sin^2(kL)]}, \tag{1.3}$$

$$T = \frac{(1 - R_1)(1 - R_2)}{[(1 - \sqrt{R_1 R_2})^2 + 4\sqrt{R_1 R_2}\sin^2(kL)]}. \tag{1.4}$$

For fiber optic pressure sensors using a FP configuration, a cleaved or polished optical fiber endface acts as a fixed mirror and a diaphragm with or without a reflective coating serves as a transducer. For static pressure measurements, the diaphragm is deflected due to the pressure difference between the inside and outside

of the cavity. The deformation of the diaphragm can be optically demodulated through processing of the reflected or transmitted signal. Different methods of retrieving the FP cavity length will be discussed in Section1.2.3.

1.2.2 Fabrication Methods of Fiber-Optic Fabry-Perot Pressure Sensors

There have been many studies on design and fabrication of FP pressure sensors. In terms of sensor design and fabrication, FP pressure sensor can be categorized into the following categories: i) pressure probes fabricated by using conventional machining and assembly techniques, ii) all-silica pressure sensors fabricated by using splicing, fusion bonding, cleaving, and wet etching of the optical fiber, silicon diaphragm, and the silica tubes, iii) pressure probes fabricated using cleanroom microfabrication techniques such as photo lithography, etching, and bonding, and iv) pressure probes with a UV cured polymer diaphragm at the end of a hollow glass tube or other type of spacer. In all of these sensors, cleaved or etched optical fibers are used as one of the mirrors of the FPI. The pressure measurements are carried out by measuring the deflection of a thin diaphragm, which serves as the other mirror of the FPI. The sizes of these sensors range from one hundred to a few hundreds micrometers in diameter. According to sensor fabrication methods, some of the previous studies are summarized as follows.

All silica optical fiber sensors fabricated by fusion-bonding, cleaving, and wet etching

Silica optical fiber has many advantages because of its material properties. Because silica material has very good chemical/thermal resistance, the fabricated sensor can withstand harsh environments, such as in an acid based solution or solvent, or in a high temperature environment. The CTE of the silica material is much smaller than that of metal or polymer so that a sensor made of silica does not suffer from significant thermal drift when it is used for pressure measurements. A silica based sensor also has relatively good biocompatibility. However, the silica material cannot be easily wielded or etched due to its inherent properties. Therefore, high temperature fusion bonding or strong acid-based chemical etching is usually involved for processing the silica material. In addition, since silica has a relatively high elastic modulus, it is difficult to obtain a miniature sensor with a high sensitivity.

Donalgic and Cibula proposed an all-fiber pressure sensor with a silicon diaphragm [3] (see Figure 1.3 (a)). The sensor was fabricated at the end of a standard (SMF) with 125 μm diameter by splicing, precision cleaving, and chemical etching of a multimode fiber (MMF) (Figure 1.3 (b)). The formation of an FPI was accomplished by splicing a MMF of 62.5 μm core diameter to a standard SMF. Then, the MMF was cleaved around 40 μm from the end of the SMF and etched in the core of the fiber selectively using HF. Since the germanium-doped MMF core has 10 times higher etching rate than pure silica, selective etching is possible for defining an optical cavity in the MMF. In order to remove the core of MMF completely without

damaging the core of the SMF, light with a wavelength of 1310 nm was coupled into the fiber and the reflected signal was monitored while the etching was performed. Another piece of a SMF was spliced to the end of the MMF and cleaved roughly 10-50 μm from the top of the MMF cavity. This structure was inserted into a standard optical connector ferrule and polished until the thickness of the spliced SMF is reduced to a few micrometers. Since the diaphragm fabricated simply by a polishing process is not thin enough to ensure a good sensitivity for mid to low range pressure measurements, the thickness of the diaphragm was fine-tuned by using a buffered HF acid etching process. Throughout the etching process, the pressure sensitivity was measured for determination of the termination time of the process.

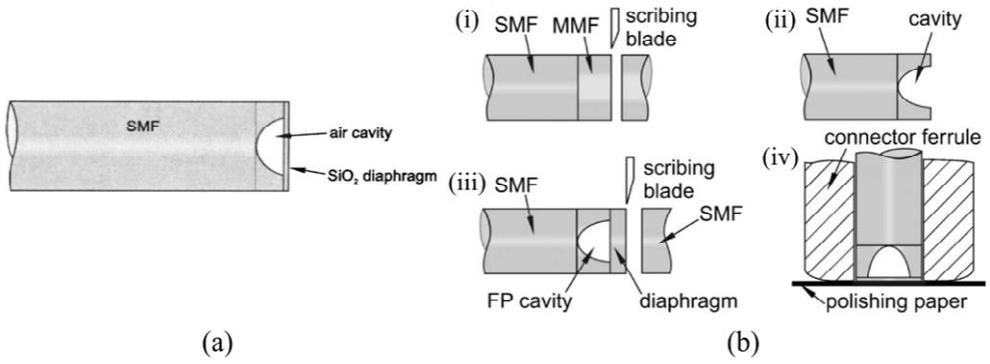

Figure 1.3: An all-fiber pressure sensor with a silicon diaphragm: (a) schematic and (b) fabrication process [3].

The maximum attainable sensitivity using this fabrication method was 23.4 nm/psi. The optical interrogation system was composed of a tunable laser, a 3 dB coupler, a power meter, and a photodetector. The tunable laser was used to set the FPI to a quadrature point and the reflected intensity from the sensor was directly

measured by using the power meter. The diameter of sensor was the same as that of SMF-28 (125 μm). However, splicing and cleaving such small segment of fiber require precise alignment and control under a microscope or an alignment system. The chemical etching of MMF cavity and silicon diaphragm needs to be monitored throughout the process by using an optical system. When etching the core of the MMF for defining the optical cavity, some part of the SMF core can be etched and degraded. This can adversely affect the signal-to-noise ratio (SNR) of the sensor. Moreover, the polishing process of the diaphragm is tedious and has a low yield. Although this sensor has many desirable attributes such as biocompatibility, robustness, small size, the fabrication process is expensive and involves dangerous chemicals.

Zhu *et al*. presented an all-fused silica optical pressure sensor [51]. Most of the fabrication process is quite similar to the sensor proposed by Donalgic and Cibula [3]. The sensor exploits spliced and etched MMF as an optical cavity and fusion-bonded silicon diaphragm. However, in this work, an additional MMF was spliced and cleaved with a length of 10 ~ 15 μm to serve as an etch-stop. This etch-stop layer can induce slight optical loss but it does not alter the sensor's interference pattern significantly (Fig. 1.4). Due to this etch-stop, the core of SMF can be protected from etchant and a flat enface can be obtained. This helps increase the quality of interference signal and the SNR of the sensor.

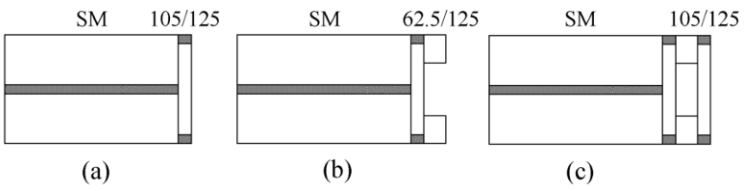

Figure 1.4: Fabrication process for an all-fiber pressure sensor with a SMF etch-stop [51].

In another work, Xu *et al*. developed another type of optical fiber tip pressure sensor that is fabricated by using a glass capillary tube covered with a silicon diaphragm for pressure and acoustic measurements [39]. The FP cavity was formed between a cleaved standard SMF endface and a fusion-bonded silicon diaphragm (Fig. 1.5). The sensor fabrication is simple, which includes cleaving, splicing (or fusion boding), and wet etching. A cleaved silica optical fiber with a 330 μm outer diameter (OD) was first spliced to the end of a fused silica capillary tube by using a fusion splicer. The fiber was then cleaved 10-30 μm away from the boundary between the glass tubing and the single mode fiber. Finally, the fiber was inserted into the glass tube and fusion bonded. Due to the dimensional changes in the fiber and the tubing, a gap distance with a 3 nm resolution can be obtained by using a CO_2 laser bonding technique. As it is hard to obtain a diaphragm thinner than 10 μm, the diaphragm was etched in HF for fine-tuning the thickness.

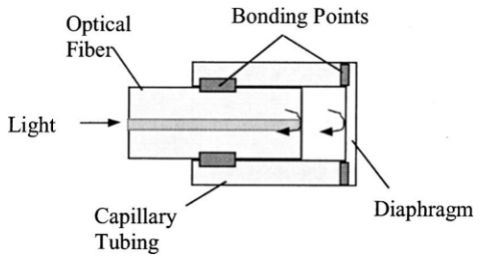

Figure 1.5: Schematic of an optical fiber tip pressure sensor constructed by using a glass capillary tube and a silica diaphragm [39].

For optical interrogation, an optical interrogation system (Micron Optics, Inc.) and spectrum analysis algorithm was used to demodulate the FP cavity length. The one peak tracking method was used to improve the measurement resolution up to ~0.005 psi. The measured sensitivity of the sensor was 3.98 nm/psi. The sensor was tested for acoustic pressure sensing by using a self-calibrated interferometric-based system. The sensor output signal showed a frequency component at 46.9 kHz with a SNR of ~19 dB, when an acoustic wave of 46.9 kHz with ~0.1 psi dynamic pressure was applied. The sensor configuration has passive temperature self-compensation capability since the thermal expansion of the optical fiber inside the capillary tube can be compensated by that of the capillary tube. Furthermore, the all-silica sensor structure has many advantages such as excellent reliability, high-temperature sensing capability, corrosion resistance, and biocompatibility. However, the fabrication process of this sensor requires a high power laser for fusion-bonding of silica tubing and harsh etchant for silicon etching. The application of the sensor is also limited due to the relatively large size of the sensor, which is from 330 μm.

Abeysinghe *et al*. proposed an all-silica optical fiber pressure and temperature sensor fabricated by self-aligned photolithography [50]. The sensor is composed of a wet-etched MMF (100/140 μm) and an anodically bonded silicon diaphragm. In this sensor, the optical cavity was defined by two different techniques. One utilizes self-aligned UV light through the optical fiber. The other exploits externally focused and aligned UV light. It is noted that the former fabrication method can eliminate the need for an expensive mask aligner and tedious aligning process due to its self-aligned characteristics. The fabrication process started with polishing of one endface of the fiber for the next lithography process. A thin layer of thinned photoresist was then applied by dipping method. For exposure of the deposited photoresist, two different exposing techniques were utilized. The first technique is coupling argon ion UV laser (λ = 457.9 nm) to the other end of sensing head by using a 5x microscope objective. The second technique is defining the area of exposure by using a high magnification objective (50x) with the same light source. This method requires optical alignment of the exposed light beam to the fiber outer diameter or core and precise control of the fiber position relative to the light beam. Comparison of the fabricated sensors shows that the latter method gives worse shape accuracy at the perimeter of the defined area because of diffraction effect. Both the exposed photoresist at the ends of the fibers were developed in a developer and etched in an etching solution NH4:HF (BHF) with an etch rate of 120 ± 6 nm on borosilicate glass fibers. The next step was to bond a thin silicon diaphragm (3-10 μm) onto the fiber endface using anodic bonding. To reduce the adhesion between the silicon diaphragm and the etched cavity bottom

surface, the temperature ramp method, an alternative method to the voltage shock method, was used. The optical interrogation system is composed of a broadband light emitting diode (λ = 850 nm), a 2 × 2 couple, a photodetector, and a photodetector with a high-pass optical filter. The measured sensitivity of one sensor was about 0.11 mV/psi with a deviation of ±0.01 mV/psi from the linear calibration curve. The sensitivity measured from another sensor that has the same dimensions except for the diaphragm thickness (3.4 μm) was found to be 0.20 mV/psi. The experimental results show a linear relationship between pressure and output photodetector voltage over the pressure range of 14-60 psi. The sensitivity of the sensors were much lower than the predicted values due to the power loss resulted from connecting two fibers with different diameters, higher order modes in the multi-mode fiber, surface roughness of the etched cavity bottom, and residual stress in the bonded diaphragm. The self-aligned photolithography using a fiber waveguide as a mask allows for low-cost sensor fabrication with a high accuracy However, it is very difficult to increase the cavity depth larger than 0.6 μm due to the limitation of the photolithography process, which can add constraints on the selection of optical demodulation methods. Furthermore, the low sensitivity of the sensor limits the application of the sensor to only high pressure measurements.

Wang *et al*. suggested a fabrication method of a miniature all-silica optical fiber pressure sensor with an ultrathin uniform diaphragm (Fig. 1.6) [52]. The basic structure and fabrication method is similar to that of the sensor developed by Donalgic and Cibula [3]. A simple and reliable way of fabricating and attaching a

thin silicon dioxide layer on top of etched housing structure was employed. The diaphragm was made out of a silicon wafer, which was oxidized to generate thin silica film on top of the silicon substrate. The silicon substrate was then etched away by using silicon deep reactive ion etching (DRIE), which uses the oxidized layer as an etching barrier. Through photo-patterning, a ring-shape silicon structure was left together with the silicon diaphragm for handling purpose. Further, the silica film was fusion-bonded to the prepared optical cavity at the end of the fiber. The sensor sensitivity was approximately 8.00 nm/psi. By using oxidation and etch-stop assisted wet-etching process, conventional polishing process can be eliminated. This fabrication process can help achieve much better reliability and uniformity of sensor fabrication.

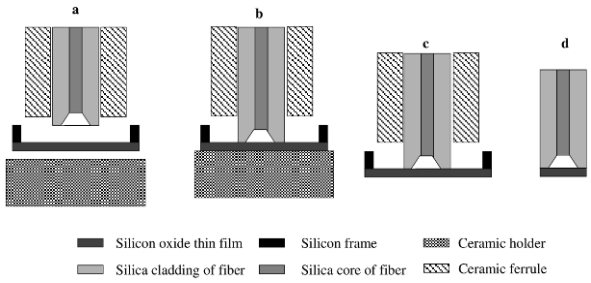

Figure 1.6: Schematic of direct bonding of silica thin film [52].

Ma *et al*. presented a fiber-optic pressure sensor that utilizes a few layers of graphene as a pressure sensing diaphragm [62]. The fabrication method of the sensor is shown in Fig. 1.7. The graphene layer was deposited on a nickel substrate whose thickness is around 0.71 nm (around 2-layer of graphene). By etching the metal layer below the graphene layer, the graphene was floated on water surface. Then, the

graphene layer was covered on a glass capillary tube based cavity structure, which was spliced to a standard optical fiber and cleaved to have desired cavity length, due to the Van der Waals force, the graphene membrane adhered to the cavity structure even without using any adhesive. This sensor shows a large pressure dynamic range, a high sensitivity, and a small form factor due to the inherent characteristics of the graphene layer. However, it is quite difficult to get a hermitic bonding between the graphene layer and the cavity because of the imperfection of the top surface of the cavity top. It was shown that there was leaking in the air FP cavity during a static pressure measurement. Therefore, this sensor can only be used for dynamic or quasi-static pressure measurement.

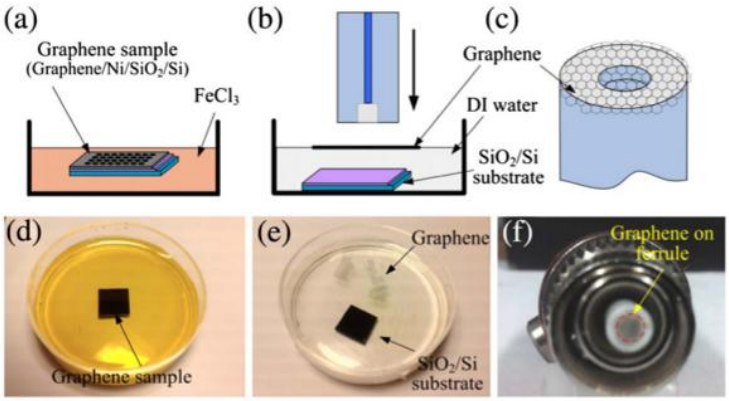

Figure 1.7: Fabrication process of the FP sensor with a graphene diaphragm: (a) etching off the Ni layer by immersing the sample into a FeCl3 solution, (b) transferring the graphene film floating on the water surface to the surface of the fiber-tip open cavity, (c) schematic showing the graphene film covering the fiber-tip microcavity, photographs of (d) graphene/Ni/SiO2/Si sample floating on FeCl3 solution, (e) graphene film floating on DI water, and (f) graphene film on the surface of the ferrule–fiber-tip microcavity assembly [62].

Pressure probes fabricated by using cleanroom microfabrication techniques: photo lithography, etching, and bonding

Various methods have been reported on fabricating an optical pressure sensor head by using cleanroom microfabrication techniques and assembling the sensor head at the end of an optical fiber. This sensor fabrication method is advantageous in several aspects. First, the well-developed microfabrication techniques can be used to build the pressure transducer structure with a high alignment accuracy and good material selection. Secondly, batch-fabrication of sensors can be achieved by using wafer scale fabrication, rendering multiple sensors with good device-to-device uniformity. One of the disadvantages of this fabrication method is that it requires tedious aligning and bonding processes after the wafer-scale sensor head is fabricated. This process is usually costly and has a low yield.

In an early work of using semiconductor process for optical pressure sensor fabrication, fabrication of an optical pressure sensor based on silicon micro-machining was carried out by Hälg [15]. A FP pressure sensor was built by using a glass substrate and a wet-etched silicon diaphragm (Fig. 1.8). The silicon diaphragm was formed by using anisotropic silicon etching to get the desired thickness. The diaphragm and the substrate were bonded together with a silicon or silicon dioxide spacer in between. The sensor diaphragm has a square shape with a thickness of 13 μm and edges between 0.5 mm and 1.5 mm. The sensing FP cavity distance is 1 to 3 μm. A light emitting diode (LED) and a photodetector were used to demodulate the phase difference with respect to pressure change. Light was coupled to the sensor

through a multimode optical fiber. The design of the sensor is similar to a conventional piezoresistive sensor except that the measurement was performed by using an optical detection technique. A fully integrated fiber optic pressure sensor was not obtained and the size of sensor head was much larger than that of an optical fiber.

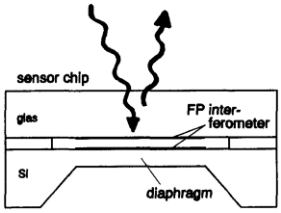

Figure 1.8: Schematic of an optical pressure sensor head fabricated by micromachining [15].

Wolthuis *et al*. also presented an optical pressure sensor fabricated by micromachining process [63]. The schematic of the sensor is shown in Figure 1.9. The sensor dimension is much smaller than that obtained in the previous work of Hälg because an etched optical cavity on glass wafer was used instead of using anodically bonded spacer structure. The sensors were machined on a wafer scale by using photolithography, metallization, wet etching, and anodic bonding processes. In order to get desired sensitivity, boron-doped silicon was anodically bonded to the etched cavity and undoped silicon was etched selectively. By using this method, around a 4 μm-thick diaphragm was obtained. Subsequently, the fabricated sensors in a wafer were diced to individual sensor heads. The completed pressure sensor was a small cube of glass with a dimension of 300 μm × 300 μm × 275 μm. A quarter-wavelength think film of titanium dioxide was deposited on the bottom of the etched

cavities to increase reflectivity of the first mirror. The cavity depth of the sensor was 14-17 μm. The diced sensors were glued to SMFs for optical interrogation. Light from a LED was coupled to the sensor. The reflected light was separated into short and long wavelength components. Pressure detection was performed by measuring the intensity ratio of these two different wavelengths in order to extend the linear range of the pressure response curve. In this work, even though the sensor size was significantly smaller than the previous work, it was still much larger than the outer diameter of a standard SMF. Moreover, the alignment and assembly of the fabricated sensor to optical fiber end is a tedious and costly process.

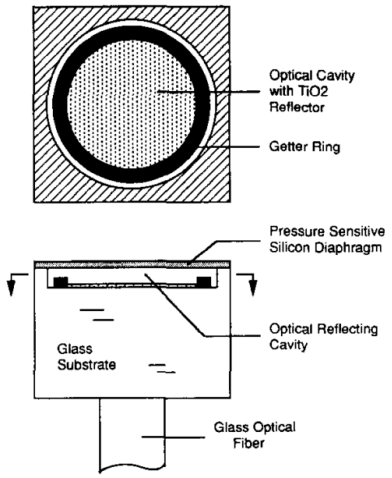

Figure 1.9: Schematic of an optical pressure sensor fabricated by micromachining [63].

Kim *et al*. presented a FP pressure sensor built by using silicon micromachining process (Fig. 1.10) [17]. Square holes were anisotropically etched through an n-type (100) silicon wafer for fiber alignment purpose. These holes also define the diaphragm size and act as fiber stop to prevent the fiber from touching the diaphragm.

Two mirrors that form the FP cavity were made of multi-layers of silicon dioxide and silicon nitride. Both top and bottom diaphragms (i.e., mirrors) were suspended by removal of the sacrificial layers through etch holes, rendering a 600 nm air gap between the two mirrors. A similar method has been used in another work done by Han [19]. In this work, releasing of the diaphragms was achieved through etching a hole in the bottom layer. The size of the bottom diaphragm was 100 μm × 100 μm. A MMF, with a core diameter of 100 μm and a cladding diameter of 145 μm, was used to couple the light from a 633 nm He-Ne laser the sensor. The disadvantage of this sensor design is that aligning and assembling optical fiber to the sensor is difficult. In addition, since the size of the sensor is limited by the dicing process, the sensor is not easy to be miniaturized.

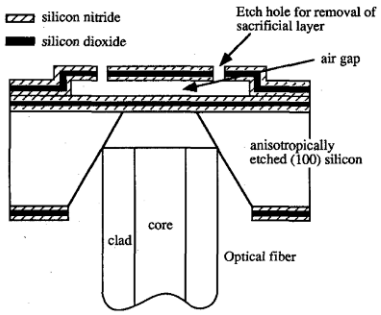

Figure 1.10: Schematic of an optical pressure sensor fabricated by using sacrificial layer etching process [17].

Gander presented a fiber optic FP pressure sensor that was fabricated by using micromachining for aerodynamics applications [37]. The schematic of the sensor and the fabricated sensor is illustrated in Figures 1.11 (a) and (b), respectively. This work is similar to the previous efforts that use microelectromechanical systems (MEMS)

fabrication processes and dicing of the sensors. However, the sensor developed in this work is easier to be assembled with an optical fiber since a circular hole with straight wall is used. Initially, a thin copper layer was deposited on the back surface of a silicon wafer (thickness 300 μm). And small holes (50 to 100 μm) that will serve as optical cavities were patterned and etched to a depth of approximately 25 μm by using DRIE, aligning with the circular copper dots. Finally, a second, larger diameter hole (125 to 140 μm) was etched on top of the first hole until the copper diaphragm was reached. While etching the larger holes using DRIE, the smaller holes were preserved due to the preferential etch direction of DRIE. This fabrication method can help achieve a flexible cavity size and depth to meet the sensitivity requirement. Because of the guiding holes at the bottom of the diced sensor, the assembling process became much more convenient than that used in previous work.

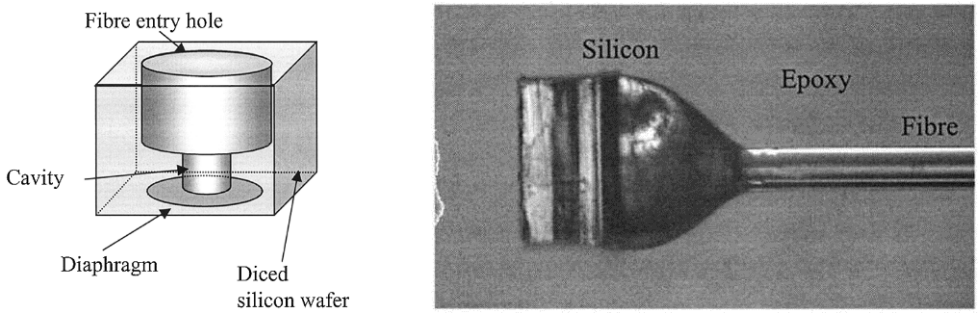

(a) (b)

Figure 1.11: (a) Schematic of diced micromachined silicon pressure and (b) fabricated pressure sensor assembled with standard SMF [37].

Totsu *et al*. proposed a fiber optic pressure sensor that was fabricated by micromachining and assembled with a glass capillary tube (Figure 1.12) [31]. In this work, a diaphragm was fabricated by chemical vapor deposition process of silicon dioxide, which adopts a mesa structure at its center to keep the mirror flat during the pressure measurements [24]. The active deflection region was kept very thin for high sensitivity requirement of biomedical applications. An aluminum layer was deposited on the mesa structure by using a lift-off process. A photosensitive-type polyimide (3 μm) was patterned as a spacer that defines the FP air cavity. The substrate of the fabricated sensor was then released by etching through the thickness of the silicon wafer with RIE. A thin chromium layer was coated as a partial mirror and the sensing element was bonded by aligning and heating both the fiber and the sensing element in a capillary tube. A glass ball lens was used to push the sensing element against the optical fiber during the heating process (Figure 1.12 (b)). This alignment method eliminates the need for tedious alignment using translational stages and an optical imaging system. However, each sensor head should be attached to a fiber endface individually. The size of the sensor is as small as a standard SMF. The sensor has a good sensitivity for measuring the internal dynamic pressure of heart and aorta.

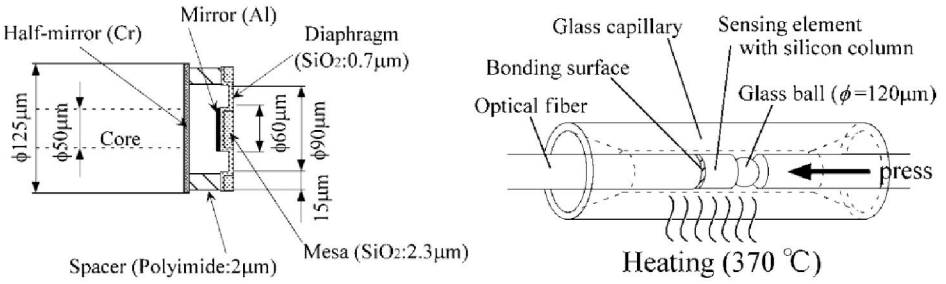

(a) (b)

Figure 1.12: (a) Schematic of micromachined silicon pressure sensor and (b) schematic of the bonding process of sensing element to optical fiber end [31].

Hill *et al*. presented a fiber optic sensor that makes use of a biocompatible polymer, SU-8, for building a FP cavity structure and diaphragm layer by using micromachining process [64]. The fabrication process is shown in Figure 1.13. The polymer was deposited and patterned first for defining the diaphragm, optical cavity, and fiber holder on a silicon substrate covered with a spun release layer (OmniCoat™). Reflective metal layer was then evaporated onto the whole wafer to increase reflectivity of the diaphragm mirror. After finishing sensor heads fabrication, optical fibers were inserted into the holes pre-made by using photolithography. After the fibers and sensor heads were glued together, the whole sensor structure was pulled off from the release layer by an optical fiber. This work is different from the previous work in terms of material used for the sensor. The polymer used in this work has good biocompatibility, thermal resistance, and manufacturability, so it can be a good candidate for pressure sensor material, especially, for biomedical applications. On the

other hand, polymer material has some drawbacks such as water-absorption and large thermal expansion, which can affect the pressure measurement adversely.

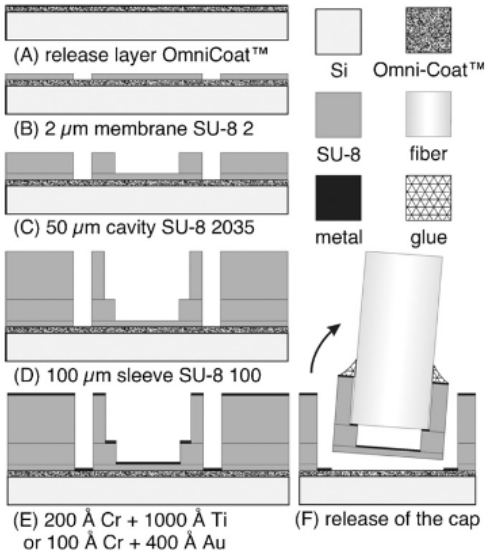

Figure 1.13: Fabrication process of SU-8 MEMS FP pressure sensor [64].

Wang *et al*. suggested a fiber optic pressure sensor design, which employs anisotropically etched V-grooves and a 45˚ angle-polished fiber [65]. In this work, the pressure sensor consists of two V-grooves having different widths, a diaphragm on the surface of the large V-groove, and a 45 ˚ angle-polished optical fiber. The schematic of the sensor is illustrated in Figure 1.14. The FP cavity length and its precision were defined by the fabrication process of photolithography and chemical etching process. The small groove was utilized for aligning the polished optical fiber. For assembling the fabricated silicon sensor head and the optical fiber, the rotational and longitudinal position of the fiber should be aligned and fixed. The sensitivity of the sensor can be easily controlled by changing the cavity diameter and the

diaphragm thickness in the pattering and etching processes. However, the size of the sensor is much larger than other reported fiber optic pressure sensors and the alignment of the fiber to the fabricated diaphragm can be tedious.

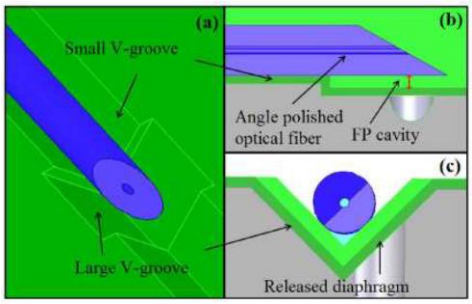

Figure 1.14: Schematic of the fiber optic pressure sensor fabricated by anisotropic etching with 45 angle-polished optical fiber [65].

Optical fiber sensor fabricated by conventional machining, electroplating, and assembly techniques

There are not many studies on fabricating fiber optic pressure sensors using conventional machining and assembly techniques. Usually optical fibers and optical cavity structures are too small to be machined or fabricated. It is hard to meet the requirement of tolerance, accuracy, and surface roughness using these conventional methods. Therefore, most of the sensors fabricated by conventional techniques are macro scale sensors.

Watson *et al*. presented a fabrication method of fiber optic pressure sensor, which exploits laser machining process and attaching an aluminized polycarbonate diaphragm [66], as shown in Figure 1.15. It is noted that an Arf pulse excimer laser

was used to ablate a cavity at the end of the optical fiber. The surface roughness of the ablated surface is one of the most critical factors, which affect the performance of the FPI. As the number of laser pulse increases for defining the optical cavity, the surface roughness becomes worse. In order to minimize the deterioration of the surface quality, the cavity depth was controlled to be smaller than 14 μm. The sensor diaphragm was prepared by thermal evaporation of aluminum on a 2 μm-thick polycarbonate film. The diaphragm was covered on the cavity under tension by using a UV curable epoxy. A FP cavity was thus produced between a laser-ablated fiber endface and a metal-polymer composite diaphragm.

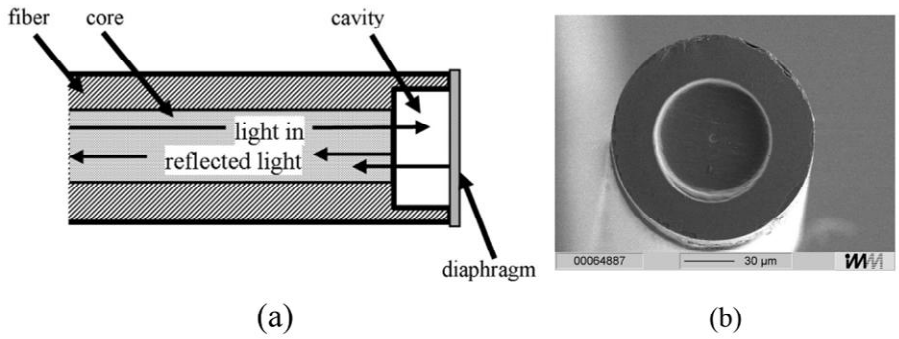

Figure 1.15: Fiber optic pressure sensor fabricated by using laser-machining: (a) schematic and (b) scanning electron micrograph of the machined cavity [66].

The sensor interrogation system consisted of three laser sources, 3×3 coupler, circulator, filter optics, and three photodetectors. Three different wavelengths were used to determine the phase of the sensor precisely. These three signals were recorded individually and combined for accurate phase retrieving using an algorithm. This method reduces phase ambiguities and eliminates the common-mode losses and noise,

which are common problems of an intensity-based measurement system. The sensor was tested in a shock tube experimental setup to evaluate its performance in terms of dynamic pressure change. It was demonstrated that the sensor exhibited a rise time of 3 μs in response to incident shocks on the order of 3 bars. Even though laser machining can be used to fabricate a miniature optical cavity with a good accuracy, the depth of the cavity is limited by this fabrication method and the diaphragm covering method is not reliable, which causes membrane tearing, delamination, and bulging.

Xu *et al*. presented a high-sensitivity FP pressure sensor with a silver diaphragm with a nanoscale thickness [67]. This sensor makes use of electroless-plated silver layer (~ 300 nm-thick) as the pressure sensing diaphragm. The schematic and a photograph of the sensor are shown in Figure 1.16. The silver layer was first plated on the inner surface of a glass beaker and relieved from the surface by etching the glass. The relieved silver film was then transferred to the endface of a zirconia ferrule. Next, an optical fiber was inserted through the other end of the ferrule and glued to the ferrule. Owing to the small thickness and low residual stress of the electroless plated layer, the sensor has a very high sensitivity of pressure measurement. However, the diameter of the sensor is relatively large due to the size of the zirconia ferruled used (diameter: 3 mm).

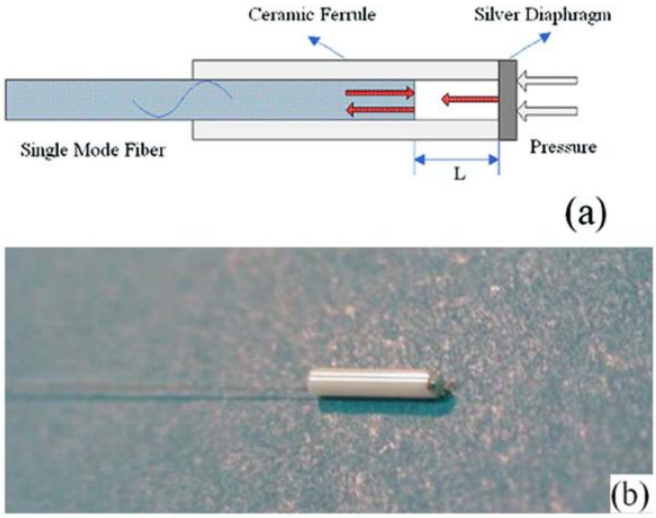

Figure 1.16: (a) Schematic of the high-sensitivity fiber optic sensor with electroless sliver plated diaphragm and (b) photograph of the sensor [67].

1.2.3 Optical Demodulation Techniques for Fabry-Perot Pressure Sensors

Technique based on intensity detection at a fixed wavelength

Interrogation of fiber optic pressure sensors can be carried out in many different ways, such as detecting the reflected intensity change from an optical sensor or demodulating FP cavity length. In this section, several techniques of optical interrogation will be briefly discussed. A FP cavity consists of two partial mirrors spaced with a gap between them. When light is coupled to the optical cavity, interference occurs in the FP cavity. In the case of a FPI, intensity as a function of the FP cavity length is given by [68]

$$I(\lambda) = I_0\left[1-\gamma\cos\left(\frac{4\pi nL}{\lambda}\right)\right], \tag{1.5}$$

where γ and L are the visibility of the interference spectrum and the optical cavity length, respectively. According to Eq. (1.5), intensity output of the interferometer varies with wavelength sinusoidally, and at a fixed wavelength, it is also a cosine-function of the FP cavity length. By using this relationship between the FP cavity length change and the intensity change, pressure variation can be detected. Cibula demonstrated pressure measurement with a miniature fiber-optic pressure sensor with a polymer diaphragm by using this detection method [20]. The wavelength spectrum of a sensor and calibration results from three sensors are shown in Figure 1.15.

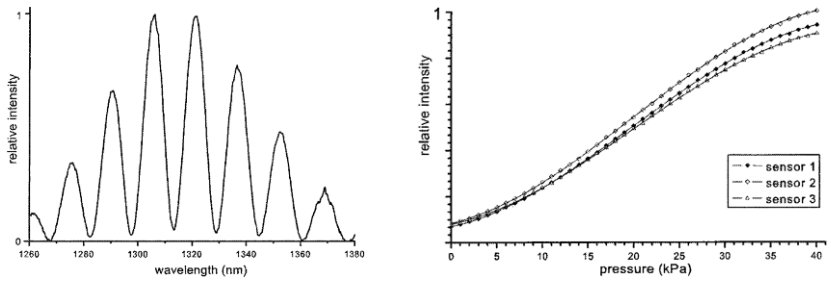

(a) (b)

Figure 1.17: (a) Measured spectrum of reflected light under LED illumination (λ = 1310 nm) and (b) relative intensity as a fuction of pressure for three fiber-optic pressure sensors with polymer diaphragms [20].

The interrogation system based on detecting intensity for measuring phase change (or FP cavity length change) is very simple, which comprises a light source, a photodetector, and a coupler. Data processing with this system is easy and fast because only intensity is measured, which can be converted to voltage signal by using the photodetector at a fixed wavelength. However, this measurement technique is

susceptible to intensity fluctuations resulting from random noise of the light source and vibration of the optical fiber. Furthermore, since the sensor dynamic range is limited by the linear range (less than $\pi/2$ in terms of phase), this method can only be used for detecting small pressure perturbations. In addition, the initial FP cavity length should be tuned to the quadrature point to ensure linear response of the sensor, which can be challenging due to the possible non-uniformity of batch fabricated fiber-optic pressure sensors.

Wolthuis *et al*. proposed another optical demodulation method based on the dichromatic ratio technique [63]. In this measurement scheme, the reflected light from the sensor was split into short and long wavelength components by a dichroic mirror. The intensity of those two light beams was measured by photodetectors with two different center wavelengths. Instead of detecting the phase variation by monitoring photocurrent from each detector, the ratio of optical power received from the two photodetectors was used. One benefit of this technique is that the dichroic ratio is relatively immune to the change in LED output intensity or fluctuation of light-handling components within the optical system. Another more important benefit of this technique is that the linear operating range of the pressure sensor can be increased by a factor of 3 to 4. The ratio was derived by getting the ratio of long wavelength intensity to sum of the both intensity. Figure 1.18 shows the comparison between these two different measurement results over the same pressure range.

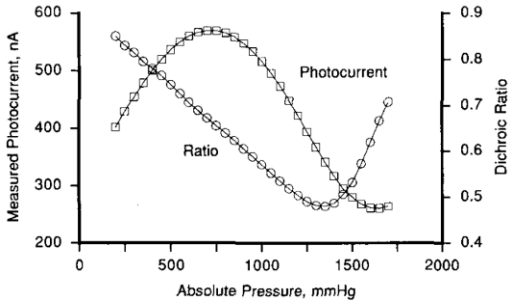

Figure 1.18: Measured sensor output in terms of photocurrent and the output from dichroic ratio signal analysis as a function of absolute pressure [63].

Technique based on spectrum analysis by using white-light interferometric

The dichromatic ratio technique can enlarge the linear range of fiber optic pressure measurement. However, there are still limitations in intensity-based measurement such as relatively small dynamic range in measurement and high accuracy requirement in sensor fabrication. There is another optical sensing technique that makes use of low coherence, broadband sources such as LEDs, multimode laser diodes, or halogen lamps. In this method, optical path length changes are observed through spectrum domain interferometric fringe pattern analysis. In the low coherence interferometric system, the output power spectrum is measured over the wavelength range of a spectrometer or an optical spectrum analyzer. The interference spectrum from a FPI sensor head can be represented as the following [69]:

$$I(\lambda) = 2I_s(\lambda)\left[1+\gamma\cos\left(\frac{4\pi d}{\lambda}+\varphi_0\right)\right], \tag{1.6}$$

where $I_s(\lambda)$ is the spectral power distribution of the light source, γ is the visibility of the interference spectrum, d is optical cavity length, and φ is the arbitrary initial phase difference. Figure 1.19 shows a typical interference spectrum. By analyzing the spectrum of the interferometer, the absolute cavity length can be retrieved. Note that any two adjacent peaks in the spectrum have a 2π phase difference. By using this relationship between two adjacent peaks, the FP cavity length L of the sensor can be calculated by using the following equation:

$$L = \frac{\lambda_1 \lambda_2}{2n(\lambda_2 - \lambda_1)}, \tag{1.7}$$

where λ_1 and λ_2 is two adjacent peak wavelength, $\lambda_1 < \lambda_2$, and n is refractive index of the FP cavity, respectively. This measurement method makes it possible to extend the dynamic range of the sensor in terms of the FP cavity length to millimeter range without ambiguity. This technique is also immune to the intensity fluctuations, and it is not sensitive to polarization of the light source and optical system. This is because the intensity fluctuation of the system usually affects the overall envelope of the spectrum not peak wavelength positions. Therefore, the frequency of the spectrum and the positions of the peaks are maintained even when the overall envelope of the spectrum changes. Furthermore, this method can help achieve absolute measurement of optical path difference as well as sensor multiplexing. However, in terms of measurement speed, this method is much slower than the previous-mentioned methods due to the large amount of data to be processed. To obtain the exact FP cavity length, all the data point in the wavelength range should be acquired and

analyzed through a peak finding process. Therefore, this technique cannot be used for high frequency dynamic measurements such as acoustic measurement or blast wave measurement.

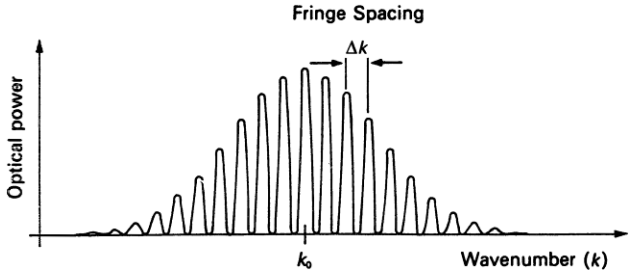

Figure 1.19: Plot of interference spectral fringes as a function of wavenumber [68].

Qi *et al*. presented a data processing technique for the white light interferometer, which can help achieve enhanced measurement resolution [69]. In a conventional two peak tracing method, more than two peaks of the intensity spectrum are used to demodulate the absolute length of a FP cavity in order to achieve a better accuracy. In this work, one peak of the spectrum is used to measure the relative variation of the optical path difference. The relation between FP cavity length and peak wavelength can be written as [69]

$$G = \frac{(m2\pi - \varphi_0)\lambda_m}{4\pi} = \frac{K_m}{2}\lambda_m, \tag{1.8}$$

where G is the FP cavity length, m is the spectral order, λ_m is the peak wave length at the spectral order m, and K_m is a constant for the given spectral order. To solve the ambiguity problem, the conventional two peak tracing method can be used for retrieving the FP cavity distance G. From the calculated G, a constant K_m for a

specific spectrum order can be calculated. By tracking the peak wavelength of the order, the FP cavity length can be retrieved. It is noted that this method gives much less relative error. For a central wavelength of 850 nm and the normal operating FP cavity length of 5 μm to 15 μm, the error of the two peak method is about 15 to 50 times larger than that of the one peak tracing method. Moreover, this method eliminates the need for multiple calculations of the FP cavity length and averaging of those. Therefore, this method is faster than the conventional two peak tracing method.

When multiple FP cavities are multiplexed, it is difficult to resolve each FP cavity length from the overlapped spectrum signal by using spectrum domain signal processing. By using frequency domain processing, these overlapped signals can be distinguished, and thus each FP cavity length can be obtained separately. Shen and Wang suggested an intensity spectrum analyzing method based on frequency-estimation with linear regression [70]. In this technique, the wavelength spectrum is converted to the wave number domain, which is used for the frequency estimation. For better result, the data is interpolated to make the wave numbers to be evenly spaced. And then the FP cavity length and the arbitrary initial phase difference are estimated by using the method of linear regression to minimize the error. One of the most important advantages of this technique is its multiplexing ability. A series of FP cavities can be connected and processed with one optical system by using this method. However, this method is computationally costly due to the linear regression or least square calculations. The other way of retrieving frequency information from the spectrum is using Fourier transform. As it was mentioned earlier, the intensity

spectrum of an FP interferometer can be described by Eq. (1.6). The fundamental frequency f_0 of the periodic function is determined by

$$f_0 = \frac{d}{\lambda^2}. \tag{1.9}$$

When the intensities of N number of FP cavities are superimposed, the total intensity in terms of the optical frequency ω can be described by

$$I(\omega) = \sum_{i=1}^{N}\left[E_{1,i}^2(\omega) + E_{2,i}^2(\omega) + 2e^{\left[-2d_i/l_c(\omega)\right]}E_{1,i}(\omega)E_{2,i}(\omega)\cos\left(\frac{4\pi d_i}{c}\omega\right)\right], \tag{1.10}$$

where E_1 and E_2 are the magnitudes of the electric fields of the reflected light, d_i are the FP cavity lengths, c is the light speed in vacuum, and l_c is coherence length. After carrying out proper filtering and Fourier transform of the pre-processed signal, the optical frequency of each cavity can be retrieved as long as those cavity lengths are not too close to each other. The absolute values of the cavity lengths can be uniquely measured from the corresponding frequencies in the interferogram, which can be described as [71]

$$d_i = \frac{c}{2}f_i = \frac{cf_{i,FFT}}{2(\nu_2 - \nu_1)} = \frac{\lambda_1\lambda_2}{2(\lambda_1 - \lambda_2)}f_{i,FFT}, \tag{1.11}$$

where $f_{i,FFT}$ is the fast Fourier transform (FFT) frequency, λ_1 and λ_2 are the starting and ending wavelengths in the spectrum, respectively. Based on Eq. (1.11), it is possible to retrieve multiple cavity lengths from the overwrapped spectrum regardless of data acquisition speed. In Figure 1.20 (a), the reflection spectra of two parallel-

multiplexed sensors are shown and in Figure 1.20 (b), the FFT results for the spectra are shown from the two sensors.

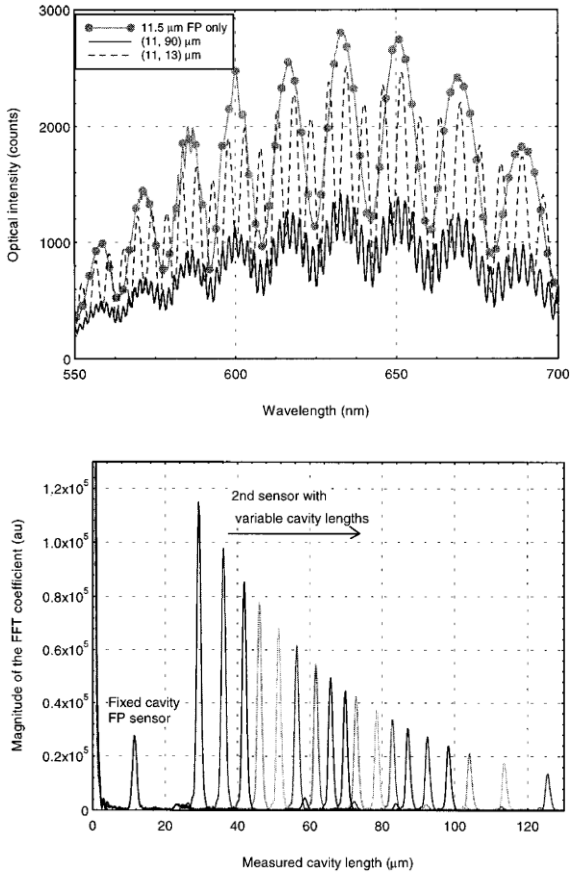

Figure 1.20: (a) Reflection spectrum from two parallel-multiplexed sensors and (b) FFT result from two multiplexed FP interferometers [71].

The optical demodulation method exploiting Fourier transforms offers the ability of signal multiplexing. However, it has much lower resolution than the wavelength-tracking method. Jiang *et al*. presented a way of enhancing the resolution of the Fourier transform white-light interferometry in retrieving the length of the FP cavity [72]. In this method, the carrier frequency is first calculated from the intensity

spectrum through the Fourier transform. The frequency of interest is then filtered and an inverse Fourier transform is carried out. Further, the phase is retrieved from the computed inverse transform by using a phase unwrapping algorithm. Finally, the FP cavity length *d* is obtained according to the following equation [72]:

$$d = \frac{\lambda_1 \lambda_2}{4\pi(\lambda_1 - \lambda_2)} \Delta\varphi(\lambda), \tag{1.12}$$

where λ_1 and λ_2 are the first and last wavelengths in the spectrum, and $\Delta\varphi(\lambda)$ is the unwrapped phase. Figure 1.21 shows the comparison of the cavity lengths obtained with finding the peak position of a Fourier spectrum and that obtained with the Fourier transform white-light interferometry (i.e., phase unwrapping of FFT spectrum method). The stage was moved by 10 μm at a time and the cavity lengths were calculated by using both methods. As can be clearly seen in the comparison, the phase unwrapping of FFT spectrum method has better resolution to resolve the movement of the stage.

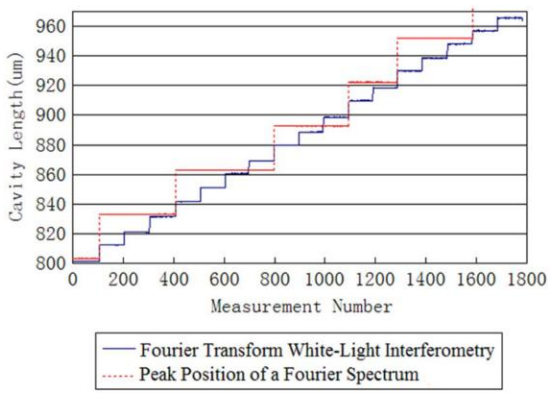

Figure 1.21: Comparison of the measured cavity lengths obtained with peak positioning and phase unwrapping of FFT spectrum methods [72].

Shen *et al*. presented a signal processing method for multiplex FP sensors based on frequency estimation [70]. The frequency-estimation is achieved through linear regression of the filtered spectrum. After pre-processing the signal with a bandpass filter, the frequency corresponds to each sensor cavity length can be obtained. This method can be used for a sensor with a relatively large cavity length and can be used to achieve sensor multiplexing. This method also enables absolute measurement of cavity length with a high resolution and a large dynamic range. Experimental results are shown in Figure 1.22. However, the calculation time is much longer than the previously reported methods since the method makes use of linear regression or least-squares estimation over a large range of wavenumber spectrum with many iterations of the calculation. Therefore, it is not suitable for a real time pressure or temperature monitoring.

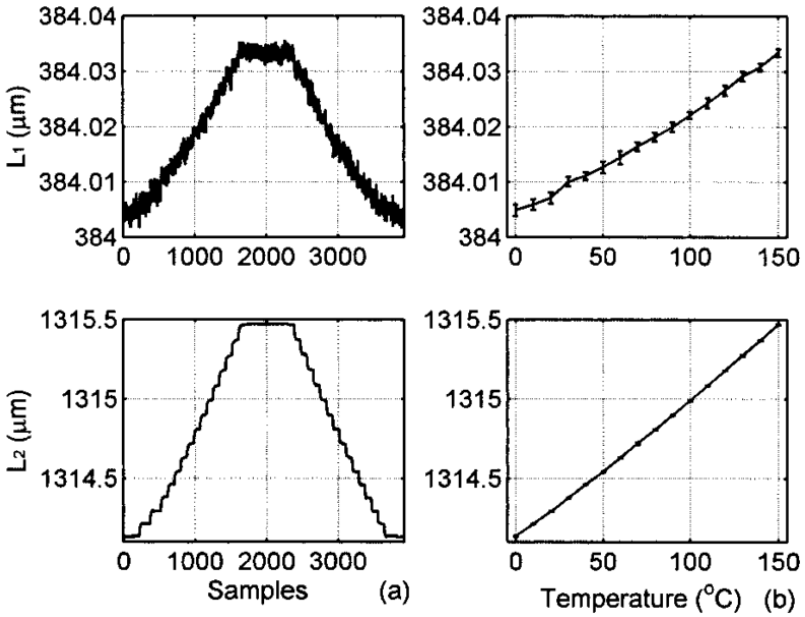

Figure 1.22: Temperature responses of the multiplexed FP sensors: (a) OPDs during the temperature cycle and (b) OPDs versus temperature [70].

1.2.4 Temperature Compensation for Fiber Optic Pressure Sensors

One of the most significant drawbacks of FP pressure sensors is their cross-sensitivity to temperature. Ambient temperature fluctuations can cause thermal expansion or shrinkage of an FP cavity structure and expansion of air in the cavity. These thermal effects will change the cavity length even under a constant pressure environment. This effect is due to the thermal expansion of sensor materials and the trapped air in the sensor cavity. Several techniques have been suggested to compensate the temperature effect of FP pressure sensors. There are two different categories of temperature compensation for a FP pressure sensor.

The first method is based on compensation of cavity length change by adopting an additional structure, which thermally expends in the opposite direction to that of the optical cavity. Xu *et al*. presented a miniature temperature-insensitive FP fiber optic pressure sensor fabricated by fusion bonding of optical fibers with different outer diameters and hollow fibers with different core sizes [59]. The schematic of the sensor is illustrated in Figure 1.23, which can be used to passively compensate the temperature effect. When the temperature increases, the optical cavity length increases due to thermal expansion of the hollow fiber. As the thermal equilibrium is achieved at the inner fiber, the fiber expands and decreases the cavity length due to thermal expansion of the inner structure. By choosing proper material and geometry of the inner fiber, the thermal effect can be minimized. However, since the pressure sensing is achieved by measuring the axial deflection of the hollow fiber, a reasonable pressure sensitivity can only be achieved with a relatively long gauge length. In order to ensure a reasonable sensitivity the gauge length of the sensor was designed to be 3.25 mm. The measured sensitivity was 0.316 nm/psi.

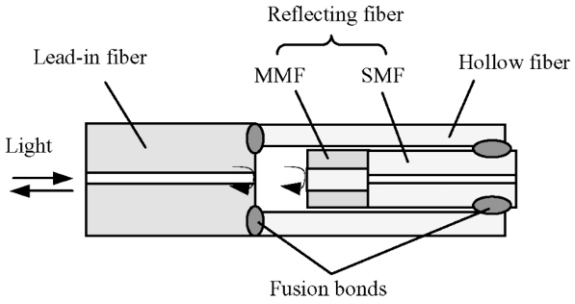

Figure 1.23: Schematic of a miniature FP fiber-optic pressure sensor with a dual layer for passive temperature compensation [59].

Wang *et al*. presented another type of temperature insensitive fiber optic pressure sensor [53], which employs a similar scheme as that of Xu *et al*. The sensor is composed of a fused silica ferrule, an optical fiber, and a fused silica diaphragm. The proposed sensor schematic is shown in Figure 1.24. The optical fiber is inserted through the ferrule and fusion bonded to the ferrule. The fused silica diaphragm is then fusion bonded to the top surface of the ferrule. The fiber inserted into the ferrule can elongate or shrink inside the ferrule with respect to the temperature change of the environment. Since the lengths of the ferrule and the fiber are kept approximately the same and the CTEs of those two components are the same, the total cavity length change with respect to the ambient temperature change can be minimized. However, the dimension of the sensor (diameter of 7 mm) is much larger than most of reported fiber optical pressure sensors.

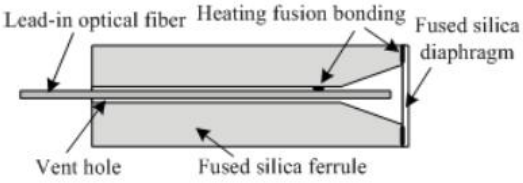

Figure 1.24: Schematic of the temperature-insensitive fiber optic sensor with silica ferrule and optical fiber [53].

The other method of temperature compensation is based on simultaneous temperature and pressure measurements. Wang *et al*. proposed a fiber-optic pressure and temperature sensor system for down-hole measurement. In this work, a FP pressure sensor and an FBG are connected in series and used in one optical system. In

the intensity spectrum, the interference signal and FBG peak are monitored simultaneously [60]. The pressure measurement and temperature measurement are performed by FP pressure sensor and the FBG, respectively. In order to retrieve the cavity length change induced purely by pressure variations, readings from both sensors are obtained and used in the following equation:

$$\begin{aligned} d &= d_0 + \Delta d_P + \Delta d_T \\ &= d_0 + \beta(T)P + \alpha(P)\Delta T\,, \\ &= a_1 PT + a_2 P + a_3 T + a_4 \end{aligned} \tag{1.13}$$

where Δd_P represents the pressure induced cavity length change, Δd_T represents the temperature induced cavity length change, d_0 is the initial length of the FP cavity, $\beta(T)$ and $\alpha(P)$ are coefficients that are considered to be linearly dependent on temperature (T) and pressure (P), respectively, and a_1, a_2, a_3, a_4 are constants that can be determined by a pressure and temperature calibration. By using this equation and the calibrated constants, the actual cavity length change due to pressure change can be obtained. Figure 1.25 shows the measured pressure after temperature compensation. It is noted that the measured pressure over the temperature range of 25.4 ˚C to 300.3 ˚C does not exhibits significant variation after the compensation.

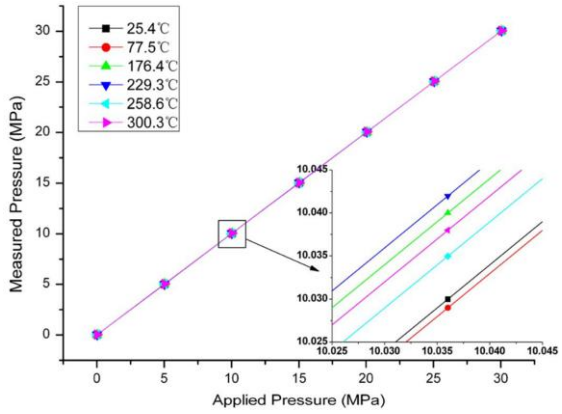

Figure 1.25: Pressure measurement result of the temperature compensated pressure sensor under different temperatures [60].

Bremer *et al*. presented a FP fiber optic pressure sensor design that makes use of an FBG as a temperature sensor in the vicinity of the pressure sensor head. A standard communication optical fiber with an FBG is inserted into a capillary tube (inner diameter of 133 μm and outer diameter of 200 μm) and fusion bonded. A 200-μm glass fiber is then spliced, cleaved, polished and wet etched to the open end of the capillary tube to form a silica diaphragm. For thermal effect compensation, the temperature and pressure dependencies of the two sensors are measured before the actual testing. Using the temperature and pressure coefficients from both sensing elements, a matrix equation can be constructed as [73]

$$\begin{bmatrix} \Delta\lambda_B \\ \Delta L \end{bmatrix} = \begin{bmatrix} S_{PB} & S_{TB} \\ S_{PFP} & S_{TFP} \end{bmatrix} \begin{bmatrix} \Delta P \\ \Delta T \end{bmatrix}, \tag{1.14}$$

where $\Delta\lambda_B$ is the Bragg wavelength shift of the FBG, ΔL is the cavity length change of the FP optical pressure sensor, S_{PB} and S_{PFP} are pressure sensitivities of FBG and FP

pressure sensor, respectively, and S_{TB} and S_{TFP} are temperature sensitivities of FBG and FP pressure sensor, respectively. The pressure difference (ΔP) and temperature difference (ΔT) can be retrieved by taking the inverse of the sensitivity matrix.

Pevec *et al*. presented a miniature, high-sensitivity, and all-silica FP fiber-optic sensor for simultaneous measurements of pressure and temperature [74]. The sensor is fabricated by using HF etching, fusion splicing, and cleaving processes. One of the FP cavities is formed between a fiber end surface and a flexible silica diaphragm, which locates at the end of the lead-in fiber. The other FP cavity is formed between the same SMF end surface and an in-fiber partial mirror created by an in-fiber air cavity made by chemical etching and splicing. Figure 1.26 shows the schematic of the sensor. In order to monitor the cavity length change of the pressure sensitive cavity, a low pass filter was applied to the optical spectrum and the cavity length was retrieved from the filtered spectrum. One peak tracing was used to retrieve the cavity length variation with respect to pressure change [69]. The temperature measurement was performed by tracing the high frequency peaks. The high frequency peak is a combination of two frequency components; the first corresponds to the silica FP cavity, and the second corresponds to the combination of the silica and air FP cavities. Since the silica cavity length is much larger than the air cavity, the two high-frequency components are too close to be isolated from each other by using a band-pass filter. Therefore, the temperature measurement was performed by subtracting pressure induced peak shift from the overall peak shift of the combined high frequency peak. The sensitivity of the sensor is relatively low (0.02 nm/psi) due to the

small size of the sensor and the high elastic modulus of the diaphragm material. Therefore, the sensor is only suitable for applications that require high pressure measurement with a large pressure range.

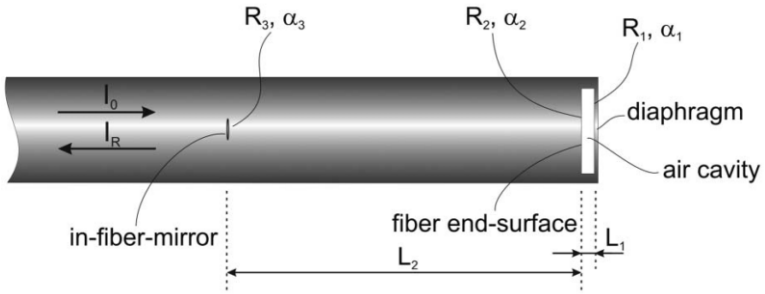

Figure 1.26: Schematic of the all-silica fiber optic sensor for simultaneous temperature and pressure sensing [74].

1.3 Objectives and Scope of Dissertation Work

The overall goal of this dissertation work is to achieve a fundamental understanding of a polymer based FP pressure sensor system and to develop high performance polymer based miniature FP fiber optic pressure sensors with temperature compensation capability. Specific objectives include the following:

1) Design, develop, and study miniature polymer based fiber optic FP pressure sensors

2) Develop novel sensor fabrication methods based on self-aligned UV lithography and UV imprinting lithography processes for achieving low cost, high repeatability, and high accuracy sensor fabrication

3) Investigate into the temperature effects of polymer based fiber-optic FP pressure sensors and develop temperature compensation methods for these sensors

4) Carry out modeling and experimental studies to obtain sensor design guidelines and characterize sensor performance

5) Explore new applications for the FP pressure sensors in emerging research fields.

In this dissertation work, polymer based FP pressure sensors with temperature compensation capability are investigated through both experimental and theoretical approaches. With the aim of biomedical applications, the sensors are developed to have abilities to respond to the pressure change of biological organs and tissues with biocompatibility. To better understand the characteristics of polymer material as a sensor structure, novel fabrication methods are investigated and different evaluation methods are used. This dissertation work is expected to enhance the current state of knowledge in the general area of fiber optic sensors, and to provide new understanding in fabrication of polymer based sensors and development of pressure sensors with temperature sensing and compensation capabilities.

1.4 Organization of Dissertation

The rest of this dissertation is organized as follows. In Chapter 2, a miniature FP fiber optic pressure sensor created with the self-aligned photolithography technique is discussed. A FBG is embedded in the vicinity of the pressure sensing cavity to measure the temperature and compensate the temperature effect of the pressure sensor.

Experimental studies of the sensor are also presented. In Chapter 3, a FP fiber optic sensor fabricated with a UV curable polymer process is discussed. A fiber based mold is developed, which helps provide a good optical alignment between the mold and the fiber with a good reliability of the replicated cavity. This sensor also has temperature sensing and compensation capabilities. Experiment studies of the sensor are discussed along with the optical measurement systems. In Chapter 4, a hybrid FP temperature and pressure sensor is presented. This sensor is made of one silica cavity for temperature sensing and another UV molded polymer cavity for pressure sensing. The sensor design eliminates the need for an extra temperature sensor and renders accurate temperature reading in the vicinity of the pressure sensing cavity. Temperature sensing and compensation capabilities of the sensor are discussed along with the experimental results. A summary of the dissertation, as well as contributions and future work, is provided in Chapter 5.

Chapter 2 Miniature Temperature Compensated Fabry-Perot Pressure Sensor Fabricated with Self-aligned Photolithography Process

2.1 Introduction

FPI is one of the most widely used fiber optic sensing technique. Fiber optic FP pressure sensors, which exploit a thin flexible diaphragm as the pressure sensing element as well as a mirror of the FP cavity and an endface or sidewall of the fiber as another mirror, are commonly used due to their high sensitivity, small form factor, and convenience of light guiding and detection [14, 22, 26, 33, 51, 75]. Fiber-optic FP sensors fabricated by using glass (SiO_2) and/or silicon (Si) materials have good mechanical and chemical stabilities. However, it is relatively difficult to obtain sensors with a small size and a high sensitivity due to the large elastic modulus (Si: 166 GPa, SiO_2: 70-75 GPa) [76,77] of the glass and silicon materials. On the other hand, when a polymer material is used in Fiber-optic FP sensors, a high sensitivity can be readily obtainable since it has low elastic modulus (0.2-4 GPa). Since there are many available processing techniques that can be used for polymer materials, sensor fabrication can be easy. In this chapter, FOFP sensors fabricated by using a self-aligned photolithography technique are presented. Instead of using the conventional mask and mask aligner for the photolithography process, an optical fiber waveguide is used to couple UV light for exposing and defining the optical cavity. This low-cost

fabrication technique offers self-aligned property for sensor fabrication. Optical analysis and sensitivity design are also discussed in this chapter.

In this chapter, a *cross-axial* and a *co-axial* type miniature pressure sensor are presented, both of which exploit maskless/self-aligned photolithography processing. The schematic of a coaxial sensor is illustrated in Figure 2.1(a), which consists of a cleaved or polished optical fiber with a pre-written FBG, a polymer housing structure, and a metal-polymer composite sensing diaphragm. This sensor configuration is called *co-axial* because the FP cavity shares that same optical axis with the optical fiber. Figure 2.1(b) shows the *cross-axial* sensor, which is composed of a fiber with a pre-written FBG and a 45 degree polished endface, a polymer housing structure, and a metal-polymer composite sensing diaphragm. This configuration is called *cross-axial* because the optical axis of the FP cavity is perpendicular to the axis of the optical fiber. The 45 degree polished fiber endface severs as a mirror to steer the light propagation direction [65]. A *co-axial* sensor is usually simpler in structure and easier to fabricate compared to a *cross-axial* sensor. However, a *cross-axial* sensor is much easier to mount on a surface when the sensing diaphragm needs to be aligned parallel to the substrate. This kind of configuration is useful in measuring static pressures without picking up dynamic pressures due to a surface flow [78].

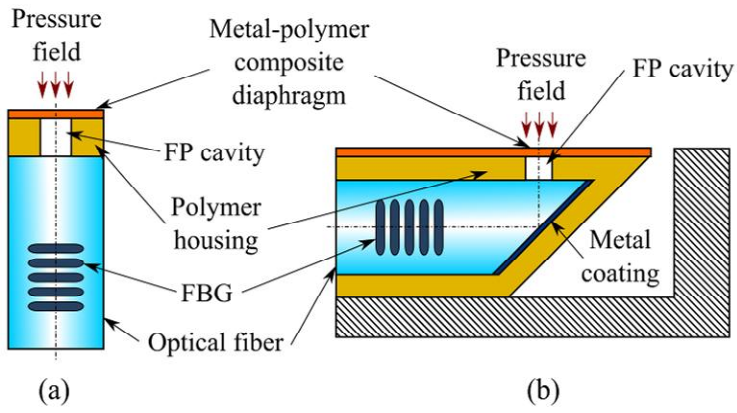

Figure 2.1: Schematic of polymer based FP pressure sensors with temperature compensation: (a) co-axial sensor and (b) cross-axial sensor.

2.3 Sensor Design and Fabrication

Based on Gaussian beam propagation through optical elements, optical modeling was performed to evaluate the performance of the *co-axial* and *cross-axial* sensors. In the *co-axial* sensor configuration, the first beam is reflected at the flat endface of the fiber. The second beam transmits through the endface, propagates along the cavity, reflects at the diaphragm, and finally returns to the fiber endface [see Figure 2.2 (a)]. The two mirrors constructing the FP cavity can be assumed to be a flat partial mirror and a total mirror, respectively. Therefore, this configuration can be simply modeled as a Gaussian beam traveling through a free space.

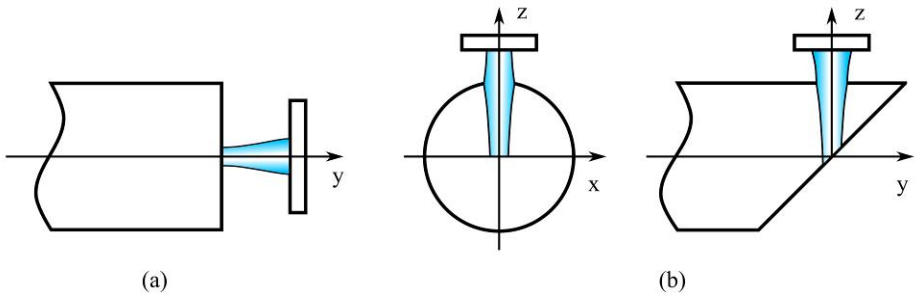

Figure 2.2: Schematic of the optics models for (a) co-axial configuration and (b) cross-axial configuration.

However, in the case of *cross-axial* configuration, the optical beam propagation inside the cavity cannot be simplified in the same way and the effect of the cylindrical interface needs to be considered. In this configuration, the light beams are reflected from and propagate through a cylindrical refractive surface, which is not rotationally symmetric (Fig. 2.2 (b)). In order to trace a light beam that goes through a non-rotationally symmetric optical element such as a cylindrical refractive surface, a four-dimensional ray vector is used. With a paraxial approximation assumption, the matrix optics method provides a good way to analyze not only a single optical element but also an optical system with many optical components [18]. The transfer matrix that describes beam propagation in a three dimensional space from State 1 to State 2 can be described by using a 4×4 ABCD matrix as the following [18]:

$$\begin{pmatrix} x_2 \\ y_2 \\ \alpha_2 \\ \beta_2 \end{pmatrix} = \begin{pmatrix} A_{xx} & A_{xy} & B_{xx} & B_{xy} \\ A_{yx} & A_{yy} & B_{yx} & B_{yy} \\ C_{xx} & C_{xy} & D_{xx} & D_{xy} \\ C_{yx} & C_{yy} & D_{yx} & D_{yy} \end{pmatrix} \begin{pmatrix} x_1 \\ y_1 \\ \alpha_1 \\ \beta_1 \end{pmatrix}, \tag{2.1}$$

where α_1 is the incident angles in y_1z plane, β_1 is the incident angle in x_1z plane, α_2 is the incident angles in y_2z plane, β_2 is the incident angle in x_2z plane, and A_{xx}, A_{xy}, A_{yx}, A_{yy}, B_{xx}, B_{xy}, B_{yx}, B_{yy}, C_{xx}, C_{xy}, C_{yx}, C_{yy}, D_{xx}, D_{xy}, D_{yx}, D_{yy} are the matrix elements for the optical system, respectively.

The above equation can be rewritten in the form of

$$\begin{pmatrix} r_2 \\ \gamma_2 \end{pmatrix} = \begin{pmatrix} A & B \\ C & D \end{pmatrix} \begin{pmatrix} r_1 \\ \gamma_1 \end{pmatrix}, \tag{2.2}$$

where $r_i = (x_i, y_i)$, $\gamma_i = (\alpha_i, \beta_i)$, $i = 1, 2$, and A, B, C, D are 2×2 matrices.

Each element of the optical system can be described by using an ABCD matrix to obtain the final transfer matrix. The final transfer function can be derived through cross-production of each ABCD matrix for all elements in the optical system. The generalized Collins integral is used to find the electric field of the output beam (E_2), which can be written as [19]

$$\begin{aligned} E_2(x_2, y_2) = (-j\exp(jkL)) / (\lambda\sqrt{\det B}) \iint E_1(x_1, y_1) \\ \cdot \exp[j\frac{\pi}{\lambda}(r_1 A B^{-1} r_1 + r_2 D B^{-1} r_2 - 2 r_1 B^{-1} r_2)] dx_1 dy_1, \end{aligned} \tag{2.3}$$

where E_1 is the electric field of the input beam, j is the imaginary unit, k is the wave vector, L is the propagation distance, λ is the wavelength, B^{-1} is the inverse of matrix B, and det B is the determinant of the matrix B.

In this analysis, the input beam is assumed to have a wavelength of 1550 nm. The beam waists ω_x, ω_y are considered to be 4.6 μm. Based on the Snell's law, the reflectivity of the interface between air and fiber cladding material is calculated to be 0.036, while the reflectivity of the polymer-metal composite diaphragm is assumed to be 1 for simplicity.

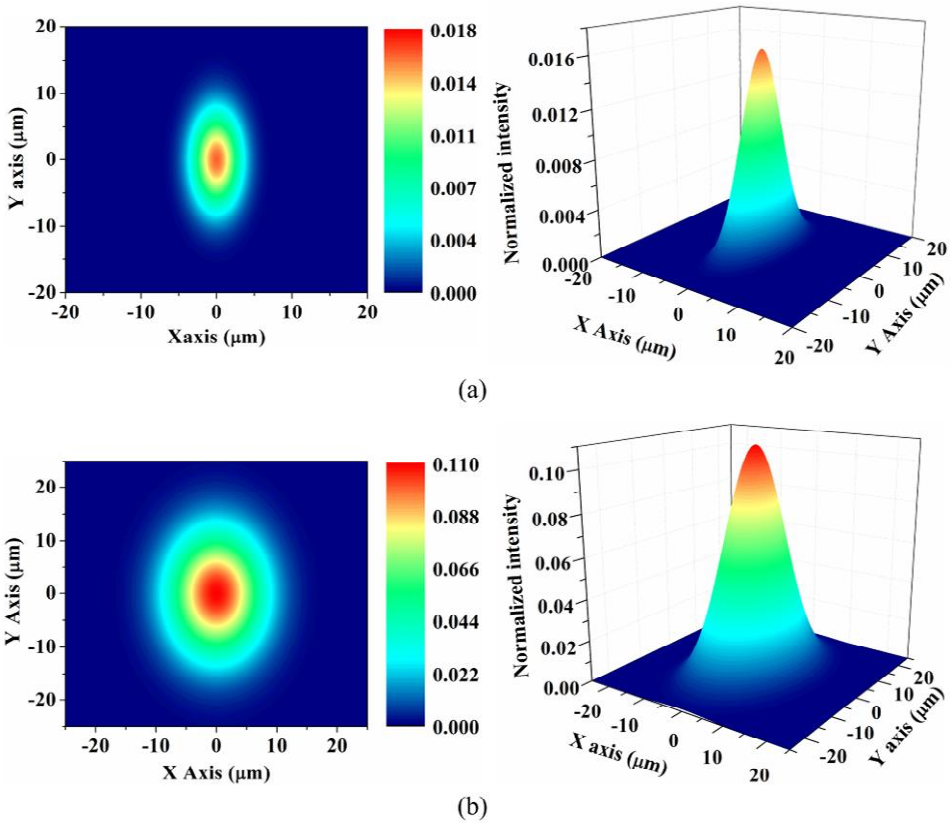

Figure 2.3: Simulation results for the cross-axial sensor: (a) intensity profile of the beam reflected from the first interface and (b) intensity profile of the beam reflected from the second interface.

The intensity profiles of the beams reflected from the first and second mirrors of the *cross-axial* sensor are shown in Figure 2.3. It can be seen that the beam waists along the *x* and *y* axes are different. Note that compared with that in the *co-axial*

sensor, the normalized intensity (see Table 2.1) of both reflected beams are smaller due to the fact that the light travels a longer distance. However, the curved optical fiber surface acting as a cylindrical partial mirror can help focus the light in the *x* direction, which helps reduce the intensity difference between the two reflected beams, resulting in a better visibility of interference, as shown in Table 2.1. The visibilities are calculated based on the relative intensity values of the beams reflected from the first mirror and the second mirror for both *co-axial* and *cross-axial* sensors.

Table 2.1 Comparison of co-axial and cross-axial sensors (The intensity is normalized by the intensity of the input beam.)

	Cross-axial sensor	Co-axial sensor
Relative intensity of the first reflected beam	0.036	0.016
Relative intensity of second reflected beam	0.715	0.109
Visibility	0.43	0.67

For both *co-axial* and *cross-axial* sensors, the optical fibers can serve as a waveguide as well as a natural mask, enabling high accuracy optical alignment and a simple, low cost fabrication process. The fabrication method of using a waveguide as a photo mask has been presented in a previous work [50], where the photoresist has been used as an etching mask for the subsequent etching process. The present work differs from the previous abovementioned work in that the photoresist itself serves as a housing structure of FP cavity. In addition, the FBG is employed as an integral part

of the sensor to compensate temperature effect, which also endows the sensor with the ability of simultaneous pressure and temperature measurements.

The *co-axial* and *cross-axial* sensors share a similar fabrication process, which is illustrated in Figure 2.4. First, an optical fiber (SMF28, Corning) with a FBG (Bragg wavelength of 1540.52 nm) written close to its one end is prepared by striping [Figure 2.4 (a)], cleaving (or polishing), and chemical treatment [Figure 2.4 (b1)]. The optical fiber is stripped and cleaved (or polished with a 45° angle for the *cross-axial* sensor) at one end prior to going through a general fiber cleaning process. The fiber is then chemically treated with an organosilane to obtain a better adhesion between the optical fiber endface and the photoresist. Next, the cleaved (or polished) end is deposited with positive photoresist (AZ 4620, Shipley) by using a 3-axis translation and rotation stage through a dipping method. The deposition process is monitored under an optical microscope (Olympus) and a digital camera (CFW-1308C, Scion Corporation). Soft baking is then carried out at 95 °C for 8 minutes. During the second stage of the process, the deposited photoresist is exposed to UV light, whose illumination area defines the area of the cavity. Instead of using a conventional aligner system, a UV light source (Blue-Wave 50S, DYMAX) is coupled into the optical fiber by using a collimating lens and the 3-axis translation stage. When exiting from the end of the fiber, the coupled UV light that is self-aligned along the optical axis is used to define the cavity area [Figure 2.4 (c1)]. Therefore, by using the fiber as a natural mask, high accuracy aligning and exposing can be achieved in a simple process. As it is well known, UV light has a rather high transmission loss in a SMF-

28 fiber. However, since the length of the optical fiber is relatively short (< 500 mm) and the input power of the UV light is high enough, a reasonable level of intensity that is sufficient for the photolithography process can be obtained. The UV light source has a very short coherence length and a broad spectrum from 240 to 400 nm, and thus, it is expected that many different modes are averaged in a random manner when propagating inside the fiber. After exiting from the sidewall, the light defines a circular cavity with good repeatability when a properly-cleaved fiber endface is used as an exit of the UV light. Further, developing and hard-baking are performed to finalize the housing structure fabrication. The exposed photoresist is developed by using a developer (AZ 440 K diluted 1:3) for 7 minutes, followed by stirring the solution gently, to form a cavity [Fig. 2.4 (d1)]. The sample is hard-baked at 87 °C for 24 hours, then at 100 °C for 20 minutes for better thermal and mechanical stability of the photoresist housing. A scanning electron micrograph of the developed optical cavity is shown in Figure 2.5. Finally, a polymer-metal composite layer is deposited on the housing structure to form a suspended diaphragm [Figure 2.4 (e1)]. In order to form a thin and uniform layer of polymer, a drop of acrylic urethane UV curing polymer (OP-4-20641, DYMAX) is dispensed onto distilled water in a petri dish using a pneumatically controlled dispenser (SL101-110, I & J FISNAR INC.). The polymer film is half cured on the water, lifted up, and covered on a batch of the samples for enhanced device-to-device uniformity. The polymer layer is then fully cured and a chromium adhesion layer plus a silver reflective layer are evaporated onto it. There may be a thin polymer layer left uncured due to exposure to oxygen in

the air, which can be washed away with isopropyl alcohol before the evaporation process for better adhesion. Additional polymer layers can be deposited to prevent the metal layer from oxidizing and corroding. Scanning electron micrographs of the fabricated *co-axial* and *cross-axial* sensors are shown in Figure 2.6. The detailed polymer diaphragm deposition process can be found in reference [33]. For the *cross-axial* sensor fabrication, the optical fiber is polished to form a 45° angled endface, and the polished surface is coated with a chromium and silver layer for enhanced reflection [Figure 2.4 (b2)]. After that, the fabrication process is identical to that of the *co-axial* sensor [Figure 2.4 (c2)-2.4 (e2)].

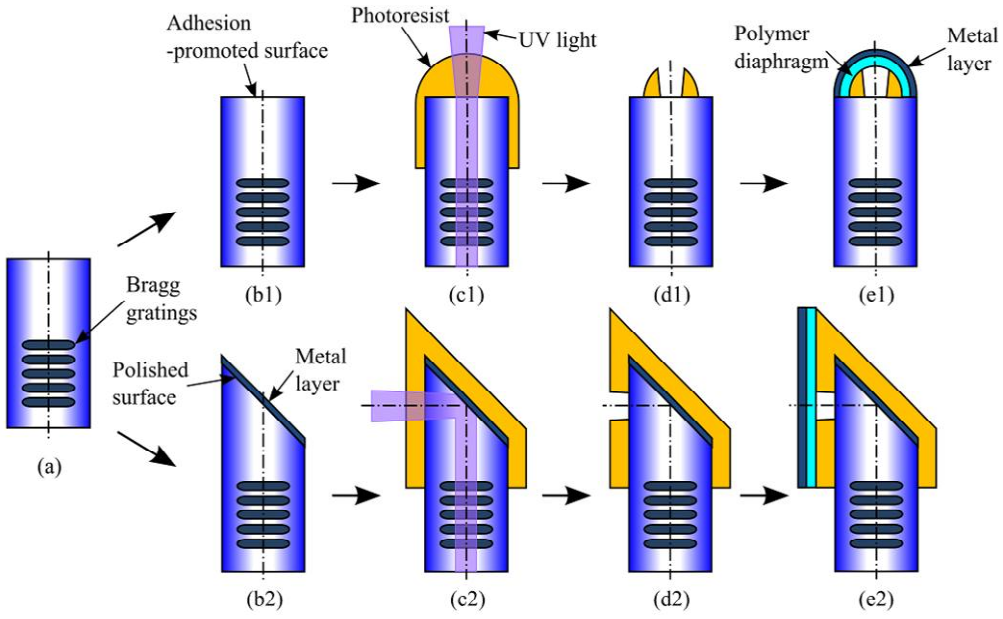

Figure 2.4: Fabrication process of co-axial and cross-axial sensors.

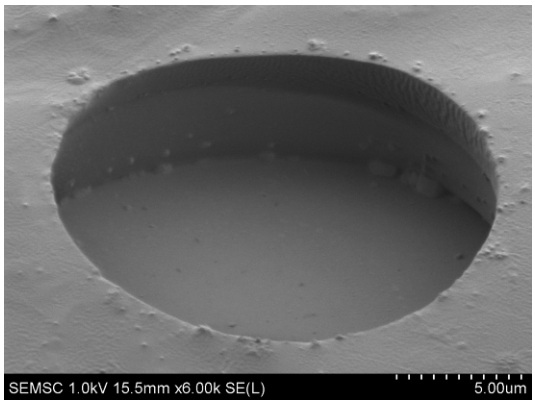

Figure 2.5: A scanning electron micrograph of developed optical cavity.

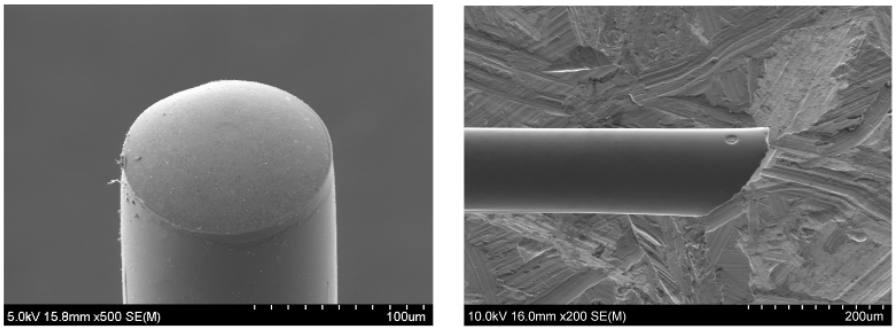

Figure 2.6: Scanning electron micrographs of fabricated sensors: (a) co-axial sensor and (b) cross-axial sensor.

The size of the air cavity is well defined by the beam diameter of the UV light. In the case of the *cross-axial* sensor, the light propagation distance is 65 μm (radius of the optical fiber), which is longer than that of the *co-axial* configuration. This means that the light beam can be diffracted more and a larger cavity can be defined. The cavity diameter was measured to be around 18 μm for the *cross-axial* sensor and

around 12 μm for the *co-axial* sensor. A urethane film with a thickness of 1.3 μm was coated with 0.003 μm of chromium and 0.15 μm of silver and used as a diaphragm for pressure sensing for the *cross-axial* configuration. For the *co-axial* configuration, 1.3 μm of polymer layer and 0.2 μm of silver metal layer were used. In the *cross-axial* configuration, a photoresist cavity with a depth of 13.8 μm was constructed on the fiber side wall, and in the *co-axial* sensor, a cavity with a depth of 23.4 μm was constructed on the fiber endface. The parameters of the sensors and the estimated sensitivities by using a finite element method (FEM) model are summarized in Table 2.2.

Table 2.2 Parameters of co-axial and cross-axial sensors.

	Cross-axial sensor	Co-axial sensor
Silver layer thickness (nm)	150	200
Chromium layer thickness (nm)	3	-
Polymer layer thickness (μm)	1.3	1.3
Cavity diameter (μm)	18	12
Cavity length (μm)	13.8	23.4
Estimated sensitivity (μm/psi)	0.0118	0.0013

The fabricated sensors are composed of a standard optical fiber (cleaved vertically or polished with 45º angle), a positive photoresist cavity, and a metal-polymer

composite diaphragm. The working principle of the sensors is based on FP interferometry and the FP cavity is formed between a cleaved optical fiber end or side wall of the fiber and the reflective surface of the composite diaphragm. The cavity diameter of the sensors, defined by the numerical aperture of the fiber, was measured to be around 18 μm for the *cross-axial* sensor and around 12 μm for the *co-axial* sensor. Given that the cavity diameters are fixed, the sensitivity of the sensors is a function of thickness and stiffness of the diaphragm. The diaphragm can be modeled as an edge-clamped circular plate. The analytical solution for obtaining the center deflection of a monolithic diaphragm is well-known and can be written as [36]

$$y(0) = \frac{3(1-\mu^2)Pa^4}{16Eh^3}, \tag{2.4}$$

where μ is the Poisson's ratio, P is the pressure, a is the radius of the diaphragm, E is the Young's modulus, and h is the thickness of the diaphragm. This equation is useful for calculating center deflection of a single-layer diaphragm, but it cannot be used here to analyze the polymer-metal composite diaphragm. A FEM model was used to predict the sensitivity of sensors with given cavity sizes, film thicknesses, and material properties of the film. Considering all the constraints of the sensor design, sensitivity of each sensor was designed to obtain enough sensitivity for pressure measurement in the pressure range of interest. To get a better estimation of the sensitivities, the elastics modulus of the thin silver film was measured by the two-layer vibrating reed method [79]. The model predicted sensitivities are 0.0118 μm/psi for the *cross-axial* sensor and 0.0013 μm/psi for the *co-axial* sensor.

2.3 Calibration and Evaluation of Sensors

2.3.1 Optical Interrogation System

In the experiment, the sensor (the coaxial or the *cross-axial* sensor) was connected to a broadband optical interrogation system, which provides a spectrum range of 700 to 1000 nm or 1510 to 1590 nm. The broadband interrogation system [Figure 2.8] is composed of an interrogator and a computer with data acquisition hardware for data collection and signal processing [33]. Interference spectra of the two different sensor configurations obtained with the optical interrogation setup are shown in Figure 2.7. The interrogator can be an optical interrogator (SM130, Micron Optics) or an interrogation setup, which comprises a broadband light source (HL-2000 Tungsten Halogen Light Source, Ocean Optics), 2×1 coupler (50/50), and a spectrometer (USB4000, Ocean Optics). A LabVIEW code was used to collect the data from the interrogator (or spectrometer) and calculate the cavity length in real time. The absolute cavity length L of the sensors retrieved from the reflection spectrum of the spectrometer can be written as

$$L = \frac{\lambda_1 \lambda_2}{2nFSR}, \tag{2.5}$$

where λ_1 and λ_2 are any two center wavelengths of adjacent peaks of the reflection spectrum, n is refractive index of the cavity medium, and FSR = $|\lambda_2 - \lambda_1|$ is the free spectral range.

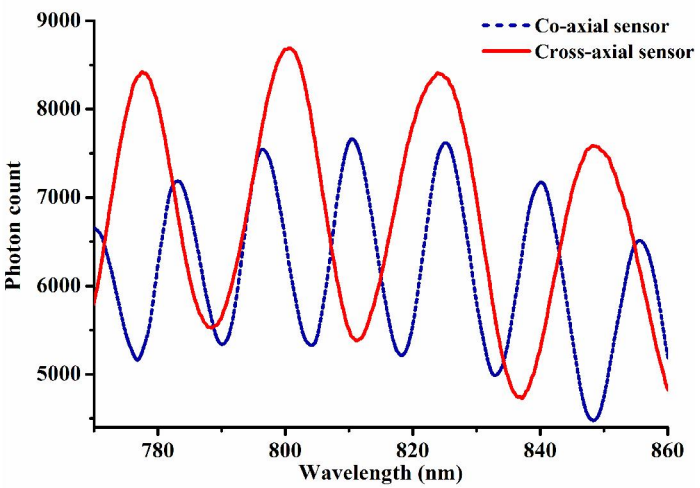

Figure 2.7: Interference spectra of cross-axial and co-axial pressure sensors obtained with the broadband interrogation system.

From selected peaks, the cavity lengths are calculated and averaged for better accuracy. The cavity length L was calculated by averaging several cavity lengths retrieved from the peaks with a good visibility to reduce random errors. After retrieving the absolute cavity length L, the one peak tracing method was used to further reduce the measurement error and decrease data processing time [69].

The experimental arrangement for static pressure measurements is shown in Figure 2.8. A conventional pressure sensor (LL-080-35A, Kulite Semiconductor) was used as a reference. The initial cavity length measurement, one peak tracing process, and pressure measurements were all carried out in real-time, which were controlled by using a LabVIEW program.

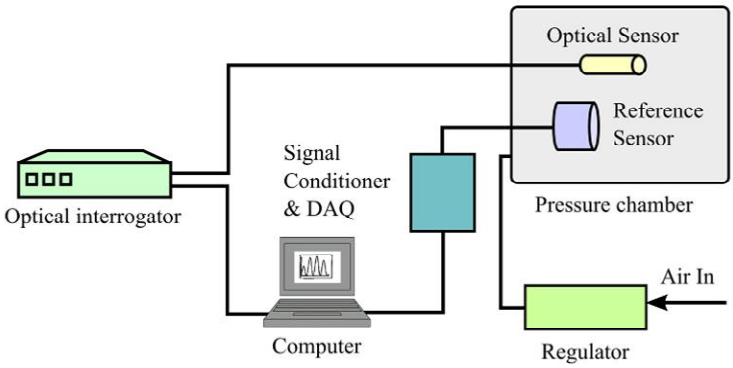

Figure 2.8: Schematic of optical system for static pressure measurements.

Generally, the spectrometer or optical spectrum analyzer has a low data acquisition rate, so it is not suitable for dynamic pressure measurement. A single wavelength reflection interrogation system was employed here for dynamic pressure measurement. This system is composed of a superluminescent diode (SLD) light source (Exalos, EXS13G1-2111) and a photodetector (New Focus, Model 2011) for fast detection of optical intensity changes. The peak wavelength of the SLD is 1300 nm and its coherence length is around 40 μm. The optical path difference of the sensor is around 28 μm. The experimental arrangement for transient pressure measurement is illustrated in Figure 2.9.

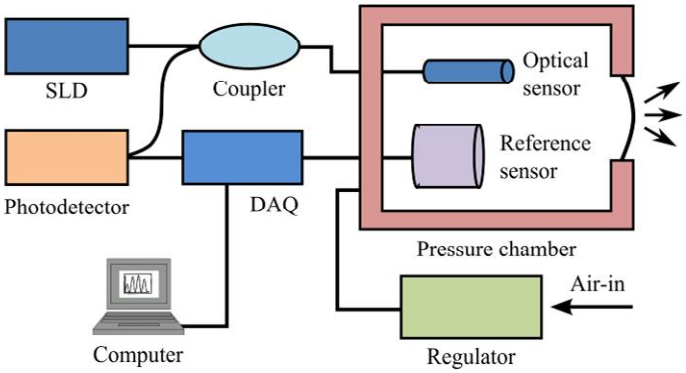

Figure 2.9: Experimental arrangement for transient pressure measurements.

2.3.2 Pressure Sensitivity

Calibration of the sensors was performed in a pressure chamber with a reference pressure sensor to evaluate performance of the optical sensors, as shown in Figure. 2.8. The internal chamber pressure was controlled by a pressure regulator (R-68825-08, Marsh Bellofram), which has a pressure range of 1.7 psi to 60 psi. In the experiments, the pressure in the chamber was first increased and then decreased with a 0.5 psi step within a range of 1.9 psi to 9.4 psi at the room temperature. The calibration results of both the *co-axial* and *cross-axial* sensors are shown in Figure 2.10. It can be seen that both sensors exhibit good linearity (R^2 = 0.997 for the *cross-axial* sensor and R^2 = 0.996 for the *co-axial* sensor) over the measured pressure range. Based on the linear regression analysis of the measured data, the pressure sensitivities were calculated to be 0.0094 μm/psi and 0.0011 μm/psi for the *cross-axial* and *co-axial* sensors, respectively. These results are comparable to those obtained in the numerical simulations (0.0118 μm/psi for the *cross-axial* sensor and 0.0013 μm/psi for the *co-axial* sensor). The slightly lower sensitivity obtained in the experiments are believed to be due to the residual stresses generated during the polymerization and metallization process of diaphragm. The hysteresis errors of the *co-axial* and *cross-axial* sensors are obtained as 7.9 % and 3.1 %, respectively. Note that the *co-axial* sensor has a smaller sensitivity due to its smaller cavity diameter (i.e., diaphragm diameter), and thus it has a smaller full scale cavity length change over the entire measured pressure range, resulting in a larger hysteresis. In the calibrations, the zero

shift and non-linearity of the calibration curves are believed to be due to the variation of the room temperature and random errors of the interrogation systems.

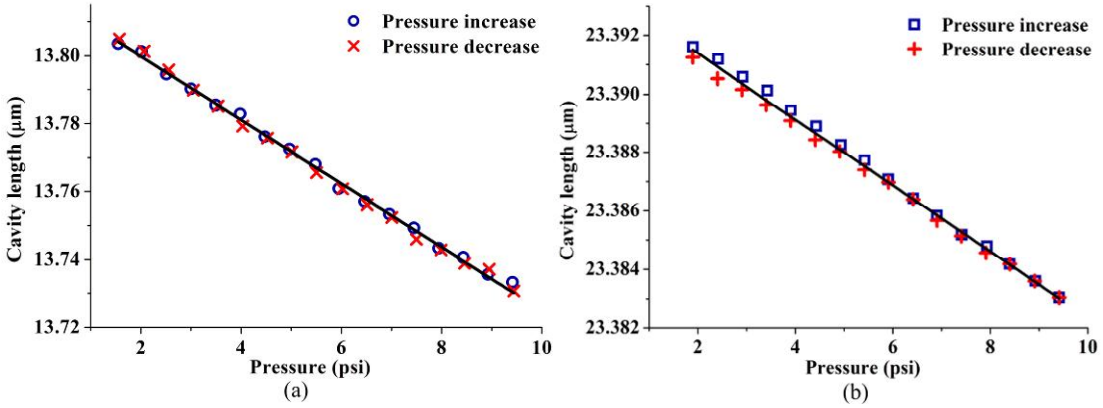

Figure 2.10: Calibration curves for (a) cross-axial sensor and (b) co-axial pressure sensor.

2.3.3 Temperature Sensitivity and Temperature Compensation

As discussed previously, due to the large CTE of the polymer material, the polymer processed optical pressure sensors are expected to have much larger temperature sensitivity than those pressure sensors made of glass or silicon. Therefore, the temperature effects on cavity length change should be evaluated and compensated for in order to obtain accurate pressure measurements. To compensate the temperature effect, the temperature induced sensor cavity length change should be carefully characterized, which can be achieved by measuring the temperature in the vicinity of the pressure sensing area with a FBG and FP cavity length variation with the previously described optical interrogation system. The fabrication process of the pressure sensor with an embedded FBG has been discussed in Section 2.3. In the experiment, the temperature sensitivity of the FBG was obtained by monitoring the Bragg wavelength shift with respect to controlled temperature variations.

Temperature control was achieved by using a thermo controller (Omega Engineering Inc., CN77333), a thermocouple (Omega Engineering Inc., CO1-K), and two polyimide-insulated flexible heaters (Omega Engineering Inc., KH 103/10). The heaters were attached at the vicinity of the pressure sensor to change the temperature locally, while minimizing the heating time and the temperature effect of the reference pressure sensor.

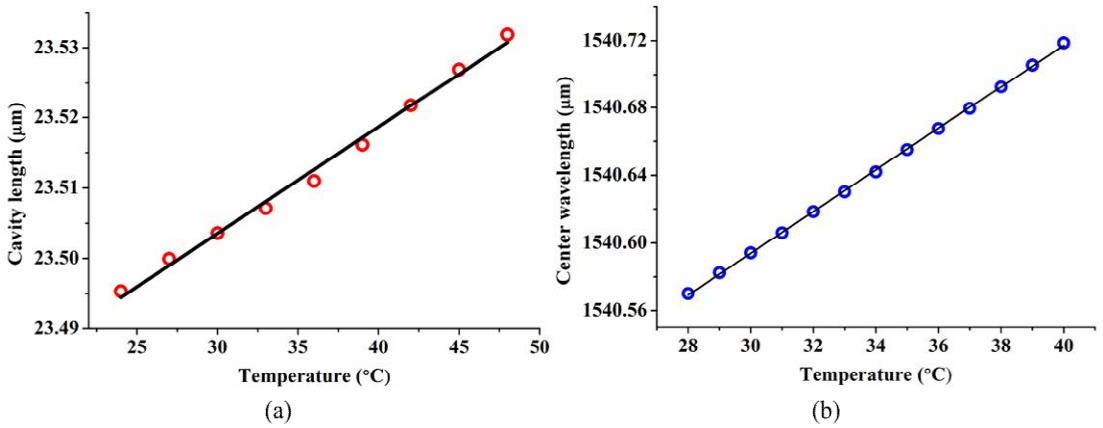

Figure 2.11 (a) Temperature sensitivity of the co-axial pressure sensor and (b) Bragg wavelength shift versus temperature of the embedded FBG.

To demonstrate the temperature compensation, here for proof-of-concept, only the results of the *co-axial* sensor are shown. It is noted that the *cross-axial* sensor also has the capability of temperature compensation. To measure the temperature sensitivity of the *co-axial* optical pressure sensor, the sensor was first heated from 24 °C to 48 °C with an increment of 3 °C under a constant pressure of 1.7 psi. The cavity length was measured at each temperature step. The obtained cavity length changes as a function of temperature is shown in Figure 2.11(a). According to this figure, a linear relationship can be observed with R^2=0.993 and the temperature sensitivity of the FP

pressure sensor can be obtained as 0.0015 μm/°C. Next, the temperature sensitivity of the FBG was calibrated. Figure 2.11(b) shows the result of the measurements with the FBG at a constant pressure level by using an optical interrogator (SM130, Micron Optics) and a custom made LabVIEW code. The measurement was performed by increasing the temperature from 28 °C to 40 °C with an increment of 2 °C. The temperature sensitivity and resolution of the FBG sensor can be obtained as 0.01234 nm/°C and 0.2 °C, respectively. When linear relationships between pressure and cavity length, temperature and cavity length, and temperature and FBG peak wavelength are assumed, the relations can be expressed in a matrix form as the following [80] [81]:

$$\begin{bmatrix} \Delta\lambda_{FBG} \\ \Delta L \end{bmatrix} = \begin{bmatrix} 0 & 0.0123\,nm/°C \\ -1.1\,nm/psi & 1.5\,nm/°C \end{bmatrix} \begin{bmatrix} \Delta P \\ \Delta T \end{bmatrix} = S \begin{bmatrix} \Delta P \\ \Delta T \end{bmatrix}, \tag{2.6}$$

where $\Delta\lambda_{FBG}$ is Bragg wavelength shift of the FBG, ΔL is cavity length change of the pressure sensor, ΔP and ΔT is the pressure change and temperature change, and S is the sensitivity matrix, respectively. Pressure sensitivity of the FBG was regarded as zero since the nominal pressure sensitivity value of the FBG (2.02×10^{-6} MPa^{-1}) is three orders of magnitude smaller than that of the optical pressure sensor. By taking inverse of the sensitivity matrix S, Eq. (2.6) can be rewritten as Eq. (2.7):

$$\begin{bmatrix} \Delta P \\ \Delta T \end{bmatrix} = S^{-1} \begin{bmatrix} \Delta\lambda_{FBG} \\ \Delta L \end{bmatrix} \tag{2.7}$$

Based on Eq. (2.7), by using the optical interrogation system (e.g., the system shown in Figure 2.8) that can measure the FBG peak wavelength shift and the cavity length change of the FP pressure sensor, both the temperature and pressure values can be retrieved simultaneously. Therefore, by using an inherently embedded FBG that can be used to monitor the temperature change during pressure measurements, the temperature effect of the pressure sensor can be compensated and accurate pressure measurements can be achieved. Table 2.3 shows performance comparison of several sensors reported in literature and the sensor developed in this work in terms of temperature compensation capability.

Table 2.3 Performance comparison of temperature compensation of several miniature fiber optic pressure sensors,

Ref.	[59]	[60]	This work
Cavity structure material	Silica	Silica	Positive photoresist
CTE of the material (με/ºC)	0.55 ~ 0.59	0.55 ~ 0.59	≈ 64.36
Pressure range (psi)	0 ~ 200	0 ~ 4351	1.7 ~ 9.5
Temperature range (°C)	25 ~ 250	18 ~ 300	24 ~ 48
Compensation scheme	Passive	Passive & active	Active
*Percentage of thermal error compensation (%)	85	95	95

* Percentage of thermal error compensation = $(e_0-e_c)/e_0*100$. (e_0: pressure error before thermal compensation, e_c: pressure error after thermal compensation)

2.3.4 Dynamic Response

There have been various types of fiber optic pressure sensors that were used for shock wave measurements [43], [44]. Here, to study the performance of the pressure sensors for dynamic pressure measurements, the *cross-axial* sensor is evaluated under time variant pressure conditions. Note that the *co-axial* sensor can also be used for the

same application. For briefness, only the *cross-axial* sensor is tested. Before carrying out the transient pressure measurements, static pressure calibration was first performed by using the experimental arrangement shown in Figure 2.9, but the pressure chamber was arranged to have fixed walls. As shown in Figure 2.11 (a), the static calibration results indicate a good linearity (R^2=0.998) between the output voltage of the photodetector and the applied pressure and the sensitivity of the sensor was obtained to be 0.032 V/psi. The pressure value was retrieved by using the Kulite reference pressure sensor. Further, by using the experimental arrangement shown in Figure 2.9, the dynamic characterization the sensor was performed. In order to study the characteristics of the sensor in response to a drastic pressure change, one of the walls of the pressure chamber was replaced with a thin metal-polymer composite diaphragm. The pressure in the chamber was then elevated gradually until the diaphragm burst. The output signals from the photodetector and the Kulite reference sensor were recorded simultaneously by using a computer with a data acquisition (DAQ) board. For both sensors, the sampling rate was set to be 16 kHz and no filter was applied to avoid filter delay. The burst of the diaphragm generates a shock wave propagating toward the sensors from the open end of the chamber, which results in a sudden pressure drop from around 15 psi to 0 psi in relative pressure.

In Figure 2.11 (b), the transient pressure reading from the *co-axial* pressure sensor is compared with that obtained from the Kulite reference sensor. A good agreement between the optical pressure sensor and reference sensor can be observed. The spikes in the measurement results correspond to a series of reflections of the expansion wave

inside the chamber. The time intervals between the spikes were found to be around 0.00119 s, which is consistent with the theoretically predicated time of 0.00118 s that is obtained by considering the round-trip distance (404 mm) from the sensor head to the diaphragm and the shock wave speed (343.2 m/s). The first natural frequency of the optical pressure sensor diaphragm is 1375.3 kHz based on the FEM simulation of a metal-polymer composite diaphragm with clamped boundary conditions. The Kulite sensor has a 75 kHz natural frequency according to the manufacture provided specifications. Therefore, both sensors have enough bandwidth to pick up the sudden drop of pressure that occurs in a much lower frequency than the natural frequencies of the two sensors. As shown in Figure 2.11 (b), the optical pressure sensor exhibits better performance in terms of detecting reflected shock waves. Fall time was measured when the pressure level drops from 90% to 10% of its maximum level for both sensors. The measured fall times of optical pressure sensor and the Kulite were around 5 ms and 4 ms, respectively. These results demonstrate that the polymer based miniature optical pressure sensors can be applied to the aerodynamic applications such as turbomachinery pressure measurements and unsteady pressure measurements on rotorcraft blades.

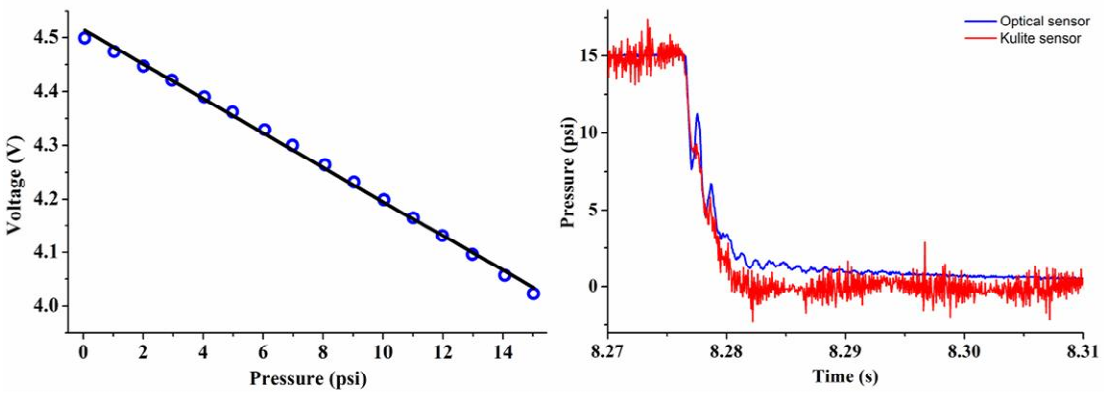

(a) (b)

Figure 2.12 (a) Pressure sensitivity calibration curve of the cross-axial sensor based on intensity measurement and (b) shock tube experimental result.

2.4 Summary

In this chapter, miniature FP pressures sensors fabricated with a novel self-aligned polymer photolithography process are presented. These sensors are created by using a polymer-metal composite diaphragm covered at a cavity fabricated at a fiber tip that is in close proximity of a FBG, rendering the sensors the capability of temperature compensation or simultaneous measurement of pressure and temperature. The fabrication follows simple, repeatable processes and safe procedures, and uses less expensive materials. More importantly, the FP cavity is self-aligned by using optical fiber as a natural mask, which eliminates the need for an external photo mask and tedious optical alignments. This fabrication method can also be used for batch fabrication or wafer scale fabrication with minor modifications to the process. Due to the relatively low stiffness of the polymer-metal composite diaphragm, sensors with extra miniature sizes but a high sensitivity can be obtained. Two types of sensors are developed based on this process: one being a *co-axial* sensor and the other being a

cross-axial sensor. The *co-axial* sensor has a simple design while the *cross-axial* sensor possesses a unique feature of being surface mountable. The experimental studies of these sensors show that both sensors have good linearity over the measured pressure range of 1.9 psi to 9.4 psi. In addition, the dynamic pressure measurement carried out by using the *cross-axial* sensor has suggested that the polymer-based miniature pressure sensors can not only be used for static pressure measurements, but also can be applied to applications that require miniature sensors for dynamic pressure measurements.

Chapter 3 Miniature Temperature Compensated Fabry-Perot Pressure Sensor Created by Using UV-molding process with an Optical Fiber Based Mold

3.1 Introduction

In Chapter 2, a positive photoresist was used for the self-aligned photolithography by using an optical fiber core as an inherent mask. However, the positive photoresist is not a cross-linked polymer even after a hard baking process. Therefore, structures made of this type of polymers do not have good chemical stability, thermal resistance, and biocompatibility. In this chapter, a fiber optic sensor based on a UV-molding process by using UV-curable polymer is presented. Fully-cured UV-curable polymers are cross-linked polymers, which have better chemical, thermal, mechanical, and biocompatible properties than positive photoresists. The UV-molding process also has flexibility in choosing materials due to the vast variety of polymer materials obtained from selecting base polymers and photoinitiators. Therefore, based on application needs, polymer materials with appropriate properties, such as biocompatibility, optical properties, and thermal/mechanical properties can be chosen. Moreover, the pressure sensitivity of the sensor discussed in Chapter 2 was not easy to be tuned to cover a large range because the pressure cavity size is defined by the mode field diameter and numerical aperture of an optical fiber. On the other hand, the optical cavity dimensions made by the UV-molding process can be freely chosen by

fabricating a master pattern with desired dimensions. This makes it easier to tune the sensitivity of the sensor to meet the needs for various applications.

UV-molding process (or UV imprinting process) is one of fabrication processes that make use of a UV curable polymer. The process (see Figure 3.1) usually consists of several steps including master pattern fabrication, mold fabrication, dispensing/exposure, and demolding. If a master pattern is used as a mold, the first step can be omitted. This process has been applied to fabricate various optical elements with small features, which allows for enhanced thermo-mechanical stability, low birefringence, and low-cost [82]. Tanigami *et al*. used the UV-molding method to fabricate Fresnel microlenses on a glass substrate [83]. The fabricated Fresnel lenses demonstrated high thermal stability, low wavefront aberration, and diffraction-limited focusing characteristics. Kunnavakkam *et al*. fabricated a low-cost and low-loss microlens array by using a soft-lithography UV replication process [84]. A mold for the microlens fabrication was replicated from a master pattern, which has the same shape as the final replica. A PDMS soft mold with a rigid glass backing was used to get good releasing property and enhanced shape accuracy. Dannberg *et al*. presented a fabrication method, which makes use of UV-assisted masking and reaction molding in fabricating optical interconnects and optoelectronic elements on wafer-scale [85].

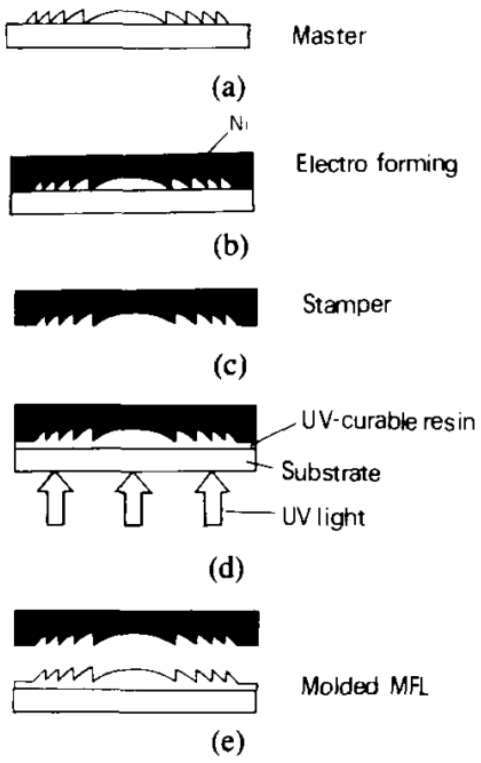

Figure 3.1: Schematic of UV molding process [83].

In the UV-molding process, replication quality is dependent on the quality of the master pattern and the characteristic of the mold surface. The replica can follow the shape of the mold with very good repeatability and accuracy if process parameters such as light intensity level, intensity profile, and pressure applied to the polymer are well controlled [82], [86]. Therefore, it is important to fabricate high quality mold to get desired properties of the final replicated optical elements such as dimensional accuracy and surface roughness. The mold can be directly fabricated by using a conventional semiconductor process, laser machining, or direct micromachining [87], [88]. In addition, the mold can also be replicated from a

master pattern, fabricated by the abovementioned methods, by using electroplating, soft lithography, or UV molding processes. Another important parameter of the mold is the releasing property of the mold surface. During the demolding process after UV exposure, stiction can occur between the mold surface and the replicated polymer. This phenomenon degrades the surface quality and replication accuracy. Moreover, the life time of the mold can be reduced significantly due to the strong adhesion force. One way of reducing the surface energy is to choose a material that has a low surface energy (e.g., nickel or PDMS). Good releasing property can also be obtained by using surface modification of silicon, silica, or metal material with organosilanes [89].

The UV-molding process can be operated at a room temperature under relatively low applied pressure or atmospheric pressure. Furthermore, the components fabricated by the UV-molding process have low birefringence and high repeatability with several tens of nanometers feature size [82,90]. The UV-molding process can be performed in batch fabrication by adopting a wafer scale fabrication technique [85,91].

In addition to the aforementioned advantages of conventional UV molding process, the sensor fabrication process developed in this dissertation work employs a unique optical fiber based mold, which enables a high accuracy, maskless, optical aligning of the sensor cavity during fabrication.

3.2 Sensor Design and Fabrication

In this work, a FP pressure sensor with built-in temperature measurement and compensation capability is designed and fabricated based on a UV-molding process and the metal-polymer composite thin film fabrication method described previously. The schematic of the sensor is shown in Figure 3.2. The cavity structure is made of a cross-linked UV curable polymer, which has good thermal/chemical stability and biocompatibility. The cavity structure is attached to the end of an optical fiber during the molding process, which is well encapsulated in the polymer structure with good reliability. In order to improve the adhesion between the optical fiber and the polymer structure, surface modification with adding a few layers of organosilane molecules can be performed without changing the optical properties of the fiber. The diaphragm of the sensor is deposited in the same way as that described in Chapter 2.

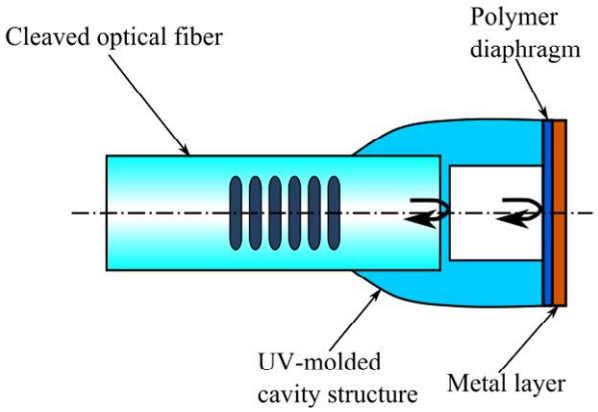

Figure 3.2: Schematic of the UV-molded optical pressure sensor.

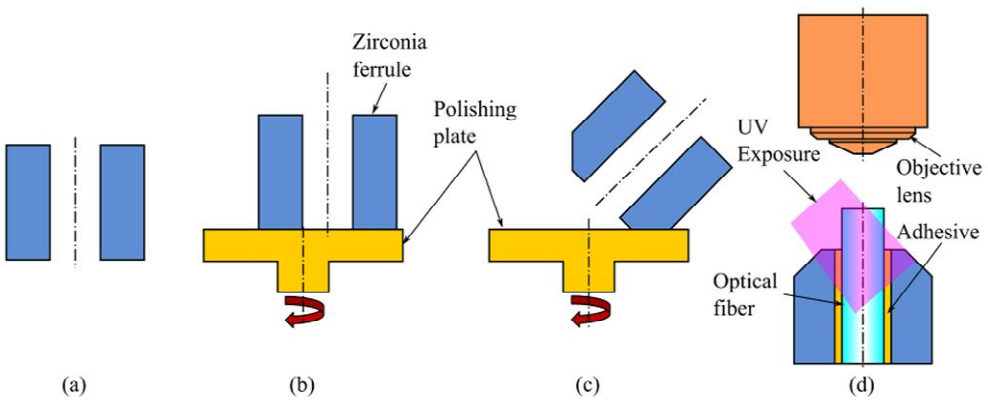

Figure 3.3: Fabrication process of the mold for creating FP cavity.

The sensor fabrication is composed of two steps. The first step is to fabricate a mold that can be used for optical cavity molding. The second step is to perform cavity molding and cover a metal-polymer composite diaphragm over the molded cavity. The detailed fabrication process of the mold is shown in Figure 3.3. A zirconia ferrule (outer diameter: 1 mm, inner diameter: 80 μm) is polished at its end face to obtain a flat and smooth surface, which will be replicated to form the top flat surface of the housing structure. The outer surface of the ferrule adjacent to the polished end face is then polished with an arbitrary angle (≈ 45°) to reduce the outer diameter of the ferrule to be around 200μm, which will define the outer diameter of the fabricated sensors. A SMF with a diameter of 80 μm (3M, FS-SC-3611) is cleaved and inserted into the ferrule by using a 5-axis translation stage. The alignment process is monitored by using an optical profilometer (TMS 1200, Polytec) that has a high vertical measurement resolution of 0.3 nm. When the desired height difference between the fiber and ferrule end face is obtained, a UV adhesive (Dymax, OP-54) is used to fill the gap between the optical fiber and the ferrule. When the gap is

completely filled, the adhesive is cured by using a UV light source (LC5, Hamamatsu). The fabricated mold is then cleaned following a general optical fiber cleaning process and treated with an organosilane to decrease the surface energy of zirconia and silica surface for easiness of releasing during the following molding process. By using commercially available optical elements and assembling technique, a high accuracy, inexpensive mold can be fabricated. The extrusion height (i.e., cavity length) can be precisely controlled with a resolution of less than 1 nm by using the optical profilometer. The fabricated mold has a high durability due to its material characteristics and good surface releasing property with the organosilanes surface treatment, rendering extended lifetime of the mold under harsh molding conditions. Furthermore, the fabricated fiber based mold enables high resolution optical alignment during the molding process of the optical cavity. The optical alignment, i.e., the core-to-core alignment of the optical fibers, will be discussed in detail in the following fabrication process. A microscopic image of the fabricated mold and a scanning electron micrograph (SEM) of the molded optical cavity are shown in Figure 3.4.

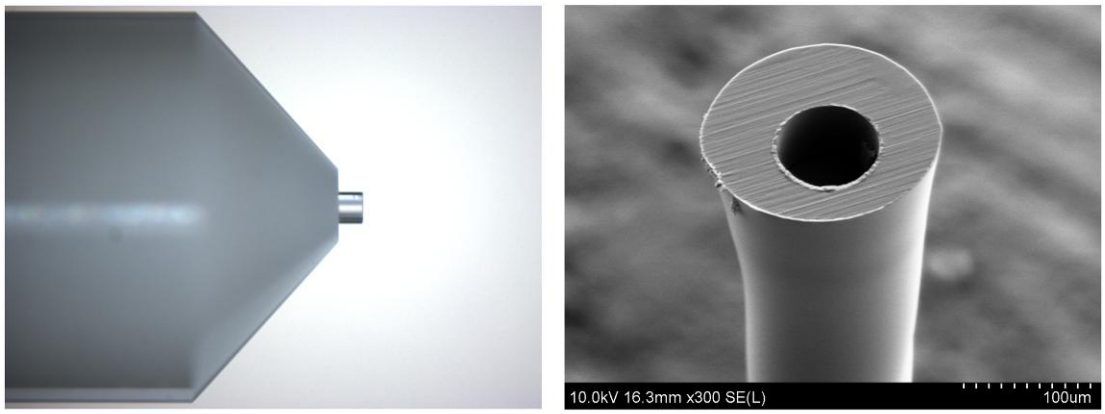

Figure 3.4: (a) Microscopic image of the fabricated mold. (b) SEM of a molded optical cavity.

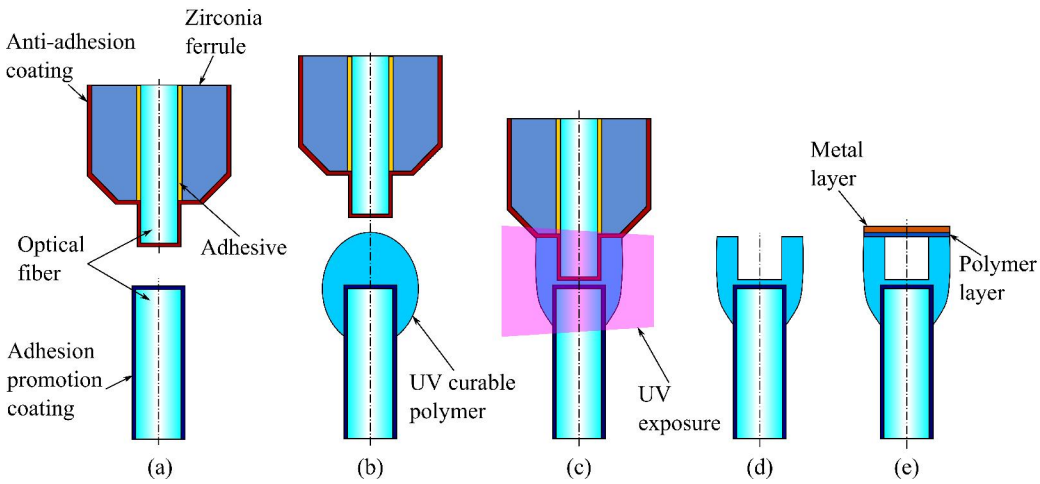

Figure 3.5: Fabrication process of UV-molded fiber optic pressure sensor.

The detailed optical cavity molding and diaphragm covering process of the sensor is illustrated in Figure 3.5. First, an optical fiber (SMF28, Corning) is prepared and aligned to the fabricated mold [Fig. 3.5(a)]. The optical fiber is cleaved (or polished) at one end prior to a general fiber cleaning process. The fiber is then chemically treated with an organosilane to obtain a better adhesion between the optical fiber

endface and the UV-curable polymer. Then, the mold and the fiber are preliminarily aligned on two 5-axis stages by using images captured from two optical microscopes with two charge-coupled device (CCD) cameras positioned with a 90-degree angle separation. Next, the cleaved fiber end is deposited with a UV-curing polymer with a dipping method [Figure 3.5(b)]. The fiber is retracted to ensure enough spacing between the fiber and the mold in the deposition process while being mounted on the stage. Another optical fiber, which has a small polymer drop at the tip, is approached to the chemically treated fiber on the stage until the polymer drop is transferred. After the deposition process, the fiber with the polymer drop is carefully moved toward the mold until it touches the mold surface to minimize the residual polymer layer between the optical fiber and the mold. The final alignment is performed to minimize the misalignment between the mold and the fiber, in which the fiber cores of the mold and the fiber on which the sensor is to be fabricated (i.e., sensing fiber) are aligned by monitoring the coupling intensity. To measure the coupling intensity, light from a SLD (Exalos, EXS13G1–2111) is coupled to the sensing fiber and the coupled light intensity is measured from the fiber in the mold by using a photodetector (New Focus, Model 2011) together with a DAQ board and a computer (see Figure 3.6).

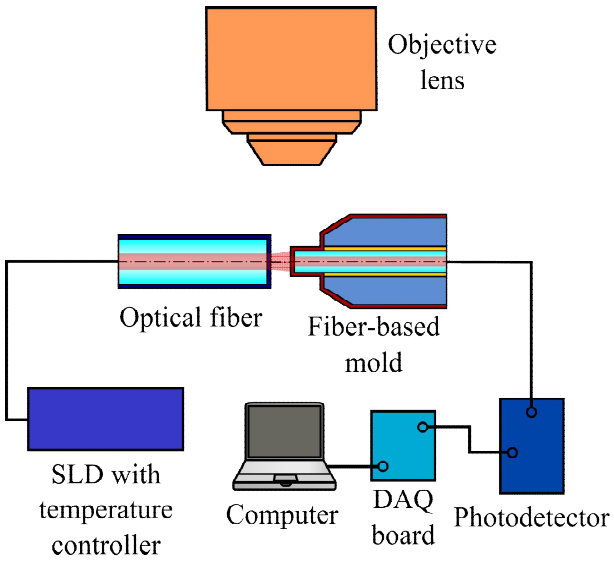

Figure 3.6: Experimental arrangement for optical alignment between the fiber-based mold and the optical fiber.

The relationship between the coupling intensity and the misalignment between two fiber cores is shown in Figure 3.7. It is noted that the accuracy of the alignment is determined by the resolution of the stage (0.5 μm for the stage used in experiment). It is possible to obtain even better alignment accuracy by using a motorized stage with a higher resolution. After a good alignment is achieved, UV-light is exposed to the UV-curing polymer. The mold is then released from the cured polymer to complete the optical cavity molding. This process renders simple sensor fabrication since the optical cavity is fabricated and securely attached to an optical fiber end face with a single process. Further, post-baking is performed to finalize the housing structure fabrication, in which the sample is baked at 150 °C for 5 hours for obtaining better thermal and mechanical stability of the UV-cured polymer housing. The 3D surface topographies of the mold and molded cavity are shown in Figure 3.8. The shrinkage

in diameter and depth during the molding process was measured to be 0.87 % and 0.65 %, respectively (see Figure 3.9). In order to get better accuracy in terms of cavity dimension, the shrinkage factors can be considered in the mold design stage to compensate for the actual shrinkage. Finally, a polymer-metal composite layer is deposited on the housing structure to form a suspended diaphragm [Figure 3.5(e)]. A SEM image of the fabricated sensor and a close-up of the diaphragm are shown in Figure 3.10. Bulging of the diaphragm can be observed in the figures, which is due to the pressure difference of the vacuum chamber of the SEM machine and the sensor air cavity.

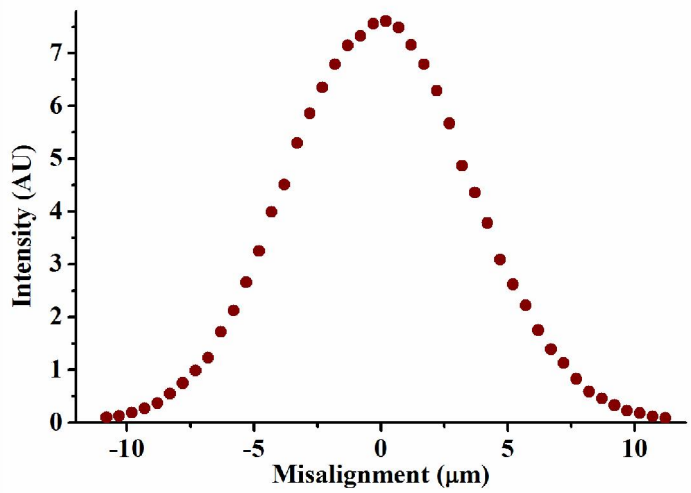

Figure 3.7: Coupled intensity as a function of the misalignment between the sensing fiber and the fiber in the mold during the alignment process. The results were experimentally obtained with a movement step of 0.5 μm from the stage.

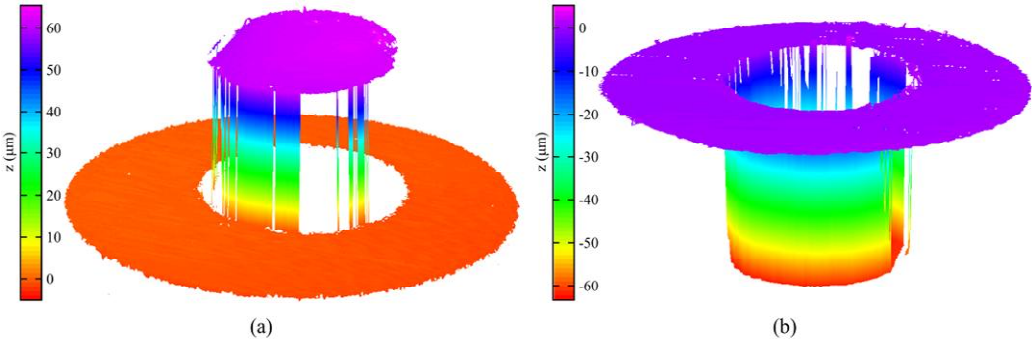

Figure 3.8: 3D surface topology: (a) the mold and (b) molded cavity.

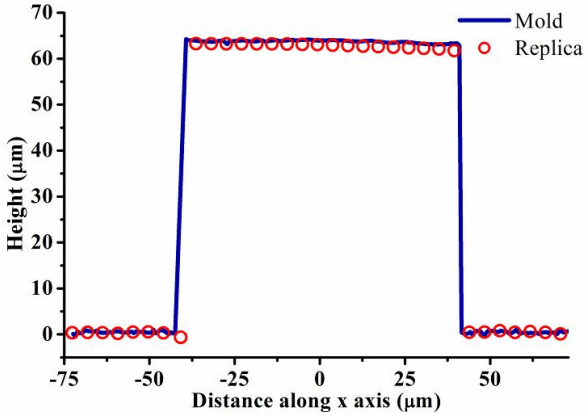

Figure 3.9: Topology comparison of the mold and the replicated cavity.

As can be seen in Figure 3.9, the diameter of the air cavity is well defined by that of the mold (i.e., the optical fiber diameter (80 μm)). The molding process can ensure a good repeatability of sensor fabrication. To verify the repeatability of the cavity molding process, 10 cavity samples were molded and their cavity diameters and depths were measured by using the optical profilometer (TMS 1200, Polytec). Maximum deviation of the cavity depth was found to be 0.12 % with respect to the mean cavity depth (50.34 μm) of the 10 samples. The deviation of the cavity diameter was not able to be detected due to the limitation of the lateral resolution of the

profilometer (~0.1 μm), which is much larger than the vertical resolution of optical profilometer (~0.3 nm). The measured surface profiles of 10 samples are shown in Figure 3.10. The results indicate that the lateral deviation of the cavity diameters is smaller than 0.1 μm for a molded cavity of 80 μm diameter. The repeatability of the cavity molding process can be further enhanced by further optimizing the process parameters such as UV light source intensity and UV curable polymer volume.

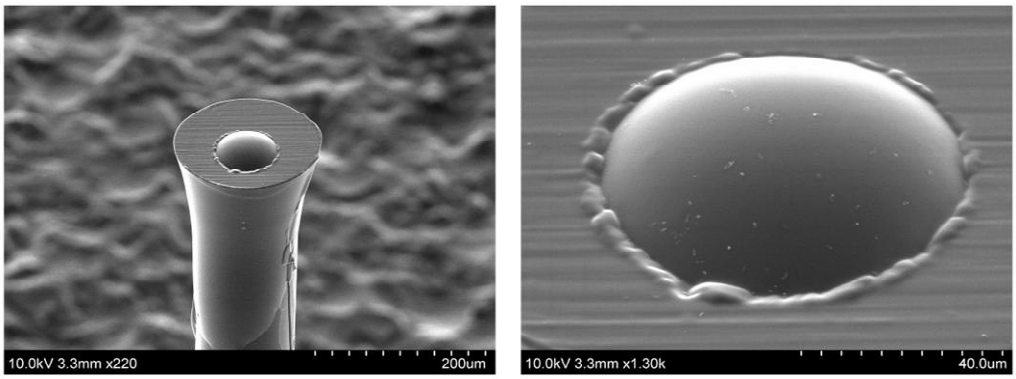

Figure 3.10: SEM images of (a) fabricated sensor and (b) diaphragm close-up.

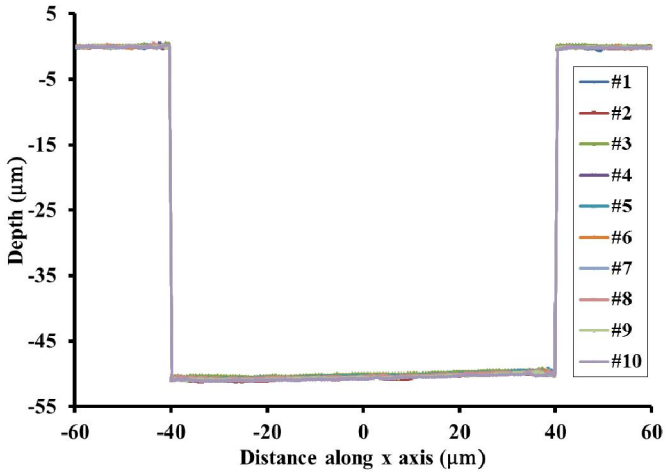

Figure 3.11: Topology comparison of 10 molded cavities.

For a given diameter of the cavity, the sensitivity of the sensors can be easily tuned by changing the thickness of the metal layer in the diaphragm according to the pressure range requirements in different applications. The extrusion height of the mold is chosen to be 64.0 μm so that the wavelength spectrum of the fabricated FP cavity will have enough number of peaks for easiness of optical signal processing. The measured extrusion height (63.6 μm) is slightly smaller than the designed value due to shrinkage of the adhesive during the curing process. The diaphragm of the sensor is made of a urethane acrylate-based film coated with a silver layer. The parameters of the sensor are summarized in Table 3.1. Since the diaphragm can be modeled as an edge-clamped circular plate, a FEM based model was used to predict the sensitivity of the sensor. The model predicated sensitivities is 0.0157 μm/psi.

Table 3.1: Parameters of two representative sensors fabricated by UV molding process

Silver layer thickness (nm)	300
Polymer layer thickness (μm)	1.0
Cavity diameter (μm)	80
Designed cavity length (μm)	64.0
Measured cavity length (μm)	63.6
Estimated sensitivity by FEM (μm/psi)	0.0157

In order to apply the abovementioned fabrication method for batch fabrication, a specially designed fiber holder should be fabricated to ensure the device-to-device uniformity of the fabrication processes. A silicon wafer with etched through holes can be exploited to align and fix fibers that are positioned in an array and leveled to one of the surfaces of the wafer. The guiding holes can be fabricated by using

photolithography and DRIE processes with a positive clearance of 3~5 μm between the hole and the fiber outer diameter. The fibers can be fixed in the holes by using mounting wax during the rest of the processes. Covering the UV curable polymer diaphragm can be performed in a wafer-scale with a good device-to-device uniformity since a uniform polymer layer with a diameter much larger than the wafer can be easily obtained by choosing a proper polymer material and controlling the volume of the polymer dispensed on water surface. Uniformity of metal layer deposition on the polymer diaphragm can be attained by using proper process parameters of a sputtering or evaporation process.

3.3 Calibration and Evaluation of the Sensors

3.3.1 Optical Interrogation System

In the experiment, the fabricated sensor was connected to a broadband optical interrogation system (SM130, Micron Optics) [Figure 3.12(b)], which provides a spectrum range of 1510 to 1590 nm. Representative interference spectra obtained from the sensor at two different temperatures (25 °C and 45 °C) are shown in Figure 3.12(a). The sinusoidal pattern in the spectrum is generated by the interference in the FP cavity and the sharp peak at wavelength of 1522.26 nm is from the FBG integrated in the pressure sensor for temperature measurement and compensation. Both the shift in spectral peaks for the optical pressure sensor and the shift in Bragg wavelength for the FBG can be seen with respect to the temperature change.

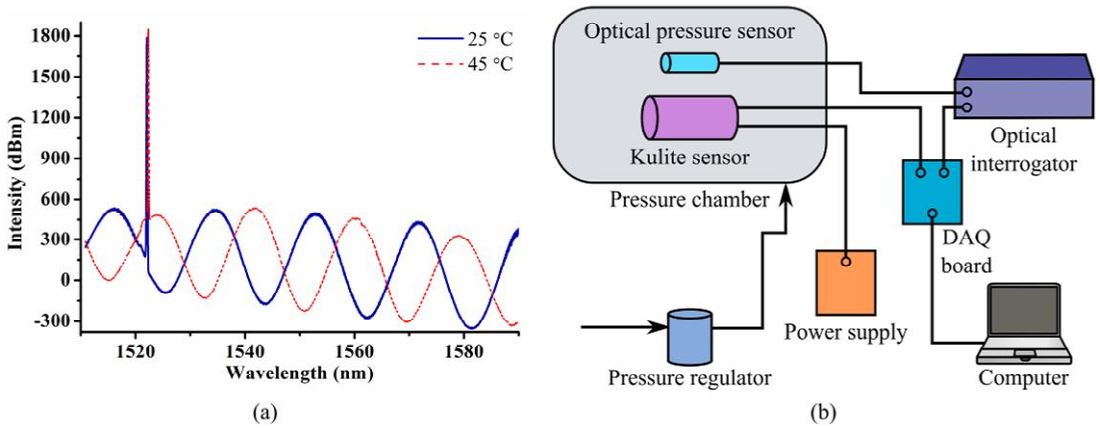

Figure 3.12: (a) Representative interference spectrum obtained by using the fabricated sensor with a built-in Bragg grating. (b) Schematic of the experimental arrangement for pressure measurement.

The absolute cavity length L of the sensor, retrieved from the reflection spectrum of the spectrometer, can be written as

$$L = \frac{\lambda_1 \lambda_2}{2nFSR}, \tag{3.1}$$

where λ_1 and λ_2 are any two center wavelengths of adjacent peaks of the reflection spectrum of the FP cavity, n is refractive index of the cavity medium, and FSR=| λ_2 - λ_1| is the free spectral range. The cavity length L was calculated by averaging several cavity lengths retrieved from a pair of two adjacent peaks with good visibility to reduce the random errors. After retrieving the absolute cavity length, the one peak tracing method was used to further reduce the measurement error and data processing time [69]. The initial cavity length measurement, one peak tracing process, and pressure measurements were all carried out in real-time, which were controlled by a LabVIEW program.

3.3.2 Pressure Sensitivity

Calibration of the sensor was performed in a pressure chamber with a reference pressure sensor to evaluate performance of the optical sensor, as shown in Figure 3.12(b). A conventional pressure sensor (LL-080-35A, Kulite Semiconductor) was used as the reference. The internal chamber pressure was controlled by using a pressure regulator (R-68825-08, Marsh Bellofram), which has a pressure range of 1.7 psi to 60 psi. In the experiments, the pressure in the chamber was first increased and then decreased with a step of 0.4 psi within a range of 1.9 psi to 7.9 psi at a room temperature of 24 °C. The calibration result of the UV-molded pressure sensor is shown in Figure 3.13(a). It can be seen that the sensor exhibits a good linearity (R^2 = 0.9996) over the entire tested pressure range. Based on linear regression analysis of the measured data, the pressure sensitivities were calculated to be 0.0106 μm/psi. This result is slightly smaller than the value obtained from the numerical simulations (0.0157 μm/psi). Residual stresses generated during the polymerization and metallization process of the diaphragm are the possible reasons for the lower measured sensitivity. The hysteresis error of the sensor was obtained as 1.5 %. In the calibrations, the small zero shift and non-linearity of the calibration curves are believed to be due to the room temperature variations and random errors from the interrogation system.

The pressure sensitivity calibration was also performed at different temperatures (e.g., 30°C, 40°C, and 50 °C) to study the effect of temperature on pressure sensitivity using the experimental setup shown in Figure 3.12(b). The results

are shown in Figure. 3.13(b). In all three cases with different temperatures, the measurement results exhibit a good linearity ($R^2 \approx 0.999$) over the measured pressure range. It is noted that there is about 5.4 % of pressure sensitivity variation over the temperature range of 24°C to 50 °C. This deviation of the sensitivity value is believed to be due to the error of the temperature controller, random error of the measurement system, and change of the sensor material properties due to the temperature change.

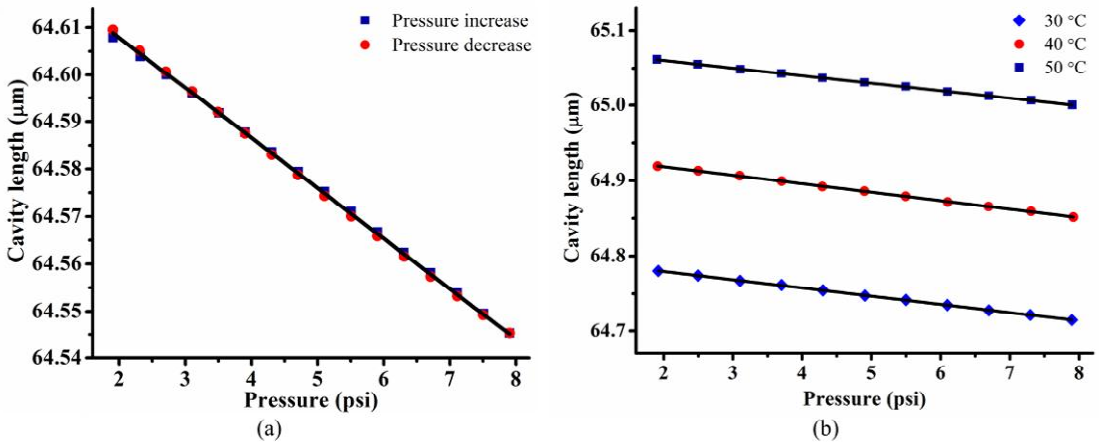

Figure 3.13: Calibration curve of the sensor at a room temperature of 24 °C and (b) calibration curves of the sensor at three difference temperatures (30 °C, 40 °C, and 50 °C).

3.3.3 Temperature Sensitivity and Temperature Compensation

As mentioned previously, due to the large CTE of the polymer material, the polymer processed optical pressure sensors are expected to have much larger temperature sensitivity than that of pressure sensors made of silicon/silica. Therefore, this effect should be evaluated and compensated for in order to obtain accurate pressure measurements. First, the temperature effect on the cavity length change is

investigated. In the experiment, the temperature sensitivity of the UV-molded pressure sensor was obtained by monitoring the optical cavity length change with respect to the controlled temperature variations. The temperature control was achieved by using a thermo controller (Omega Engineering Inc., CN77333), a thermocouple (Omega Engineering Inc., CO1-K), and two polyimide-insulated flexible heaters (Omega Engineering Inc., KH 103/10). The heaters were attached at the vicinity of the pressure sensor to control the temperature locally, while minimizing the heating time and the temperature effect on the reference pressure sensor. To measure its temperature sensitivity, the sensor was first heated from 26 °C to 50 °C with an increment of 3 °C under a constant pressure of 1.9 psi. The cavity length was measured at each temperature step. The obtained cavity length change as a function of temperature is shown in Figure 3.14(a). According to the result, a linear relationship can be observed with R^2=0.9983 and the temperature sensitivity of the FP pressure sensor can be obtained as 0.0158 μm/°C. To compensate for the temperature effects, the temperature at the vicinity of the pressure sensing area can be measured with the FBG embedded in the sensor to relate the temperature to cavity length variations. Figure 3.14(b) shows the measured FBG Bragg wavelengths at a constant pressure level by using the same optical interrogation system and the LabVIEW code. The measurement was performed simultaneously with the temperature sensitivity measurement of the pressure sensor. The temperature sensitivity and the resolution of the FBG sensor was obtained as 0.0120 nm/°C and 0.12 °C, respectively. By using the pressure sensitivity and temperature sensitivity of the FP pressure sensor and

temperature sensitivity of the FBG, temperature compensation as well as simultaneous temperature and pressure measurements can be achieved.

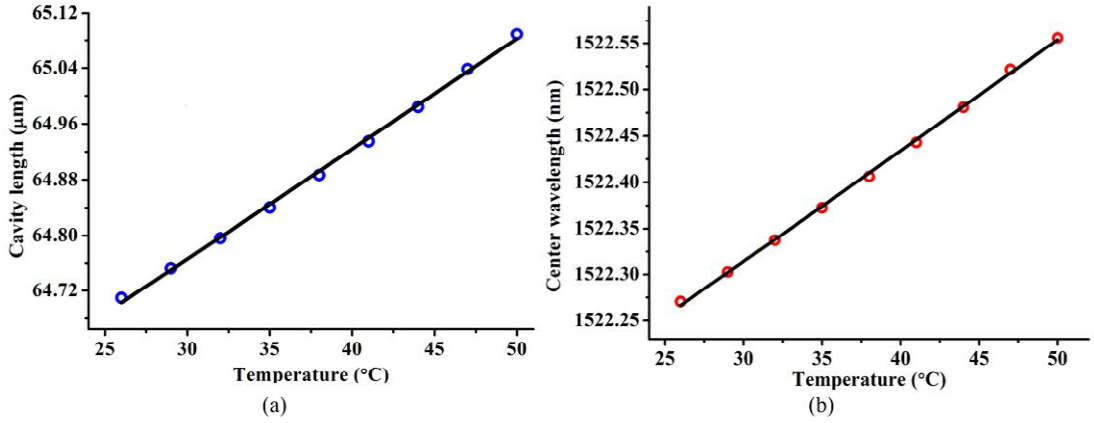

Figure 3.14: (a) Temperature sensitivity of the pressure sensor. (b) Temperature sensitivity of the FBG embedded in the pressure sensor.

Even though there is a small variation in the pressure sensitivity of the sensor at different temperatures (<5.4%), it was shown that the cavity length of the pressure sensor changes linearly with respect to both pressure and temperature, and the Bragg wavelength of the FBG also shifts linearly with respect to temperature. Therefore, in the working temperature range (24~50 °C), these linear relationships can be expressed in a matrix form as the following [81] [73]:

$$\begin{bmatrix} \Delta\lambda_{FBG} \\ \Delta L \end{bmatrix} = \begin{bmatrix} 0 & 0.0120\,nm/°C \\ 10.6\,nm/psi & 15.8\,nm/°C \end{bmatrix} \begin{bmatrix} \Delta P \\ \Delta T \end{bmatrix} = S \begin{bmatrix} \Delta P \\ \Delta T \end{bmatrix}, \tag{3.2}$$

where $\Delta\lambda_{FBG}$ is Bragg wavelength shift of the FBG, ΔL is cavity length change of the pressure sensor, ΔP and ΔT is the pressure change and temperature change, S is the sensitivity matrix, respectively. The pressure sensitivity of the FBG can be neglected

since the nominal pressure sensitivity value of the FBG (2.02×10^{-6} MPa^{-1}) is three orders of magnitude smaller than that of the optical pressure sensor. By taking inverse of the sensitivity matrix S, Eq. (3.2) can be rewritten as:

$$\begin{bmatrix} \Delta P \\ \Delta T \end{bmatrix} = S^{-1} \begin{bmatrix} \Delta \lambda_{FBG} \\ \Delta L \end{bmatrix}. \tag{3.3}$$

Based on Eq. (3.3), by using an optical system (e.g., the system shown in Figure 3.12(b)) that can measure both the Bragg wavelength shift and the cavity length change of the FP pressure sensor, the temperature and pressure values can be retrieved simultaneously. Note that in an application that requires high accuracy pressure measurements, the measurement error due to the pressure sensitivity variation with respect to temperature changes can be reduced by using an formula based on Taylor expansion with nonlinear terms [58]. Another way of reducing this error is to use the support vector regression (SVR) method to obtain an approximate non-linear function in the whole region through a statistical machine learning process [92]. Therefore, by adding an inherently embedded FBG that can be used to monitor the temperature change during pressure measurements, the temperature effect of the pressure sensor can be compensated.

3.4. Pressure Measurements in Biomedical Applications Using Fabricated Sensors

3.4.1 In-Vivo Blood Pressure Measurement in a Swine Study

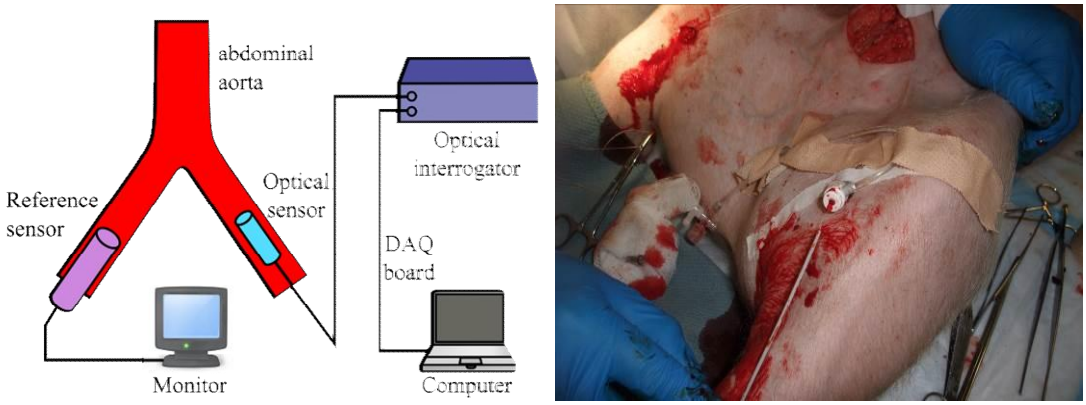

(a) (b)

Figure 3.15: (a) Schematic of the experimental arrangement for blood pressure measurement and (b) a photograph of swine under blood pressure measurement.

An in-vivo swine study was performed to demonstrate the feasibility of using the polymer based FP pressure sensor for blood pressure measurement. In the experiment, the fabricated sensor was connected to a broadband optical interrogation system (SM130, Micron Optics), which provides a spectrum range of 1510 nm to 1590 nm with a sampling rate of 8 Hz. A commercially available invasive blood pressure measurement system (Transpac IV from Braun Medical) was used as the reference for measuring and monitoring the arterial pressure in the right artery. The polymer-based fiber optic pressure sensor was used to measure pressure in the left artery. A catheter was inserted into the left artery first to make a way for insertion of the optical fiber

sensor. The fiber optic sensor was then inserted through the catheter for a depth of 15 cm. The experimental setup and a photograph of the swine under the test are shown in Figure 3.15.

As shown in Figure 3.16, blood pressure pulse (Figure 3.16(b)) was clearly seen in the fiber optic sensor reading, which was consistent with the pressure measurement result obtained from the reference sensor (see Figure 3.16(a)).

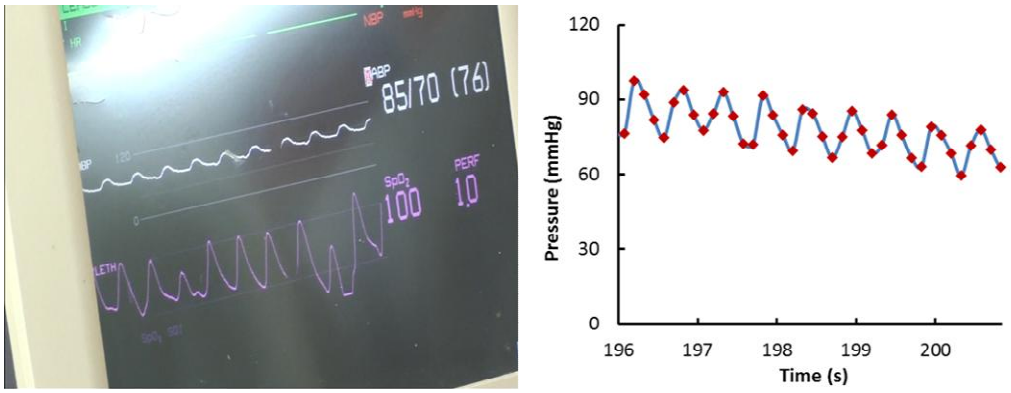

(a) (b)

Figure 3.16: Blood pressure readings from (a) the reference sensor (Transpac IV) and (b) fiber optic sensor.

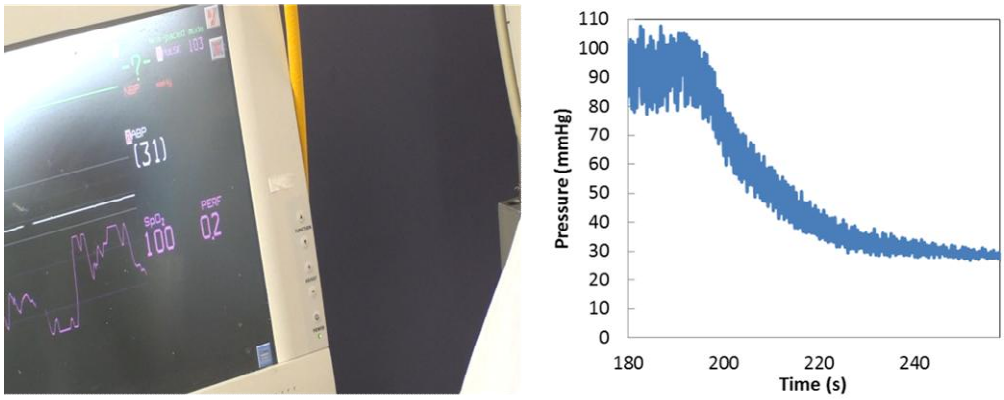

(a) (b)

Figure 3.17: Blood pressure readings from (a) the reference sensor after injecting Beuthanasia and (b) the fiber optic sensor before and after injecting Beuthanasia.

At the end of the swine study, Beuthanasia was administered to the swine through an IV in the ear vein. Consequently, a blood pressure drop was clearly observed along with pulse deceasing from both the fiber optic sensor and the reference sensor, as shown in Figure 3.17. Based on these measurement results, it has been demonstrated that the polymer based fiber optic pressure sensor is highly promising for blood pressure measurements. During the experiment, sensitivity alteration of the sensor was observed. It was possibly due to the force applied on the sensor head while inserting the sensor through the catheter. In order to improve the sensor performance, temperature compensation and sensor protection procedure during insertion can be implemented in the future studies. In addition, an interrogation system with a higher sampling rate can be used to improve the temporal resolution so that a, smoother pressure waveform can be acquired.

3.4.1 In-Vitro Intradiscal Pressure Measurement of a Swine

Here, a UV-molded pressure sensor is used in an in-vitro study for intradiscal pressure measurements of a swine disc. In the experiment, a broadband optical interrogation system (SM130, Micron Optics) was used, which is identical to the one used for the previously described blood pressure measurement. A segment of intervertebral disc harvested from a swine was mounted under a material testing system to apply controlled load (or pressure) to the disc, as illustrated in Figure 3.18.

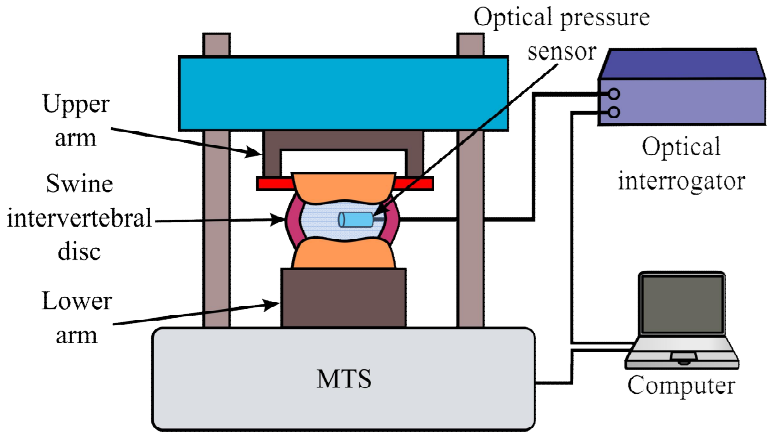

Figure 3.18: Experimental arrangement for swine intervertebral disc pressure measurement.

An UV molded fiber optic pressure sensor was inserted through the disc by using a hollow needle of gauge 29 (outer diameter: 337 μm, inner diameter: 184 μm). A photograph of the disc with the inserted pressure sensor is shown in Figure 3.19(a). After the fiber was inserted, the needle was retracted so that only the sensor was left in the disc. During loading experiment, the disc was initially compressed with a load of 390 N by lowering the upper lam of the material testing system (MTS). The load was then reduced to 195 N and kept for 15 minutes. The same load cycle was

repeated 5 times and the intradiscal pressure was monitored through the sensor inside the disc. In order to mimic the actual load condition in a spin a steel rod was inserted through the upper part of the disc and the load was applied through the rod. Figure 3.19(b) shows the pressure measurement result throughout the load cycles. This result demonstrates that the intradiscal pressure with respect to the load applied to the disc can be successfully measured. It is also noted that due to water absorption of the polymer structure, the polymer cavity of the sensor increases even without applied pressure or under a constant pressure. To improve the performance of the sensor for intradiscal pressure sensing, in the future work, the water absorption issue should be addressed and the sensitivity of the sensor should be properly designed according to the maximum pressure level of the testing.

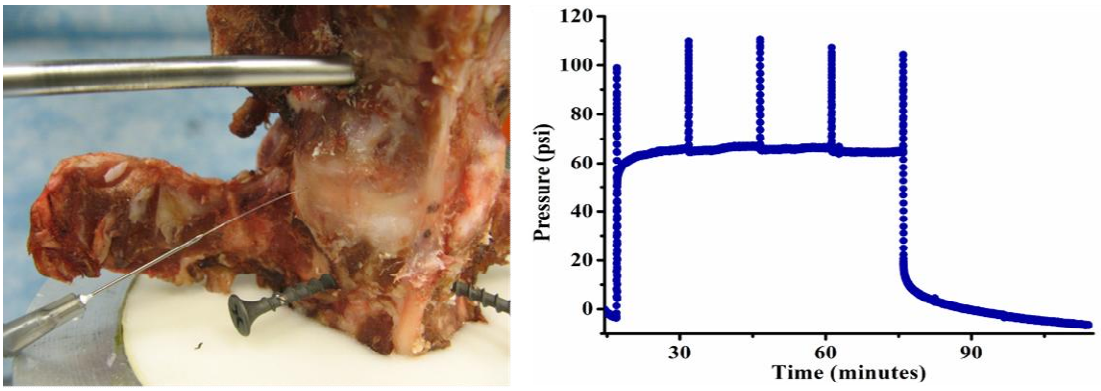

(a) (b)

Figure 3.19: (a) A photograph of the swine intervertebral disc with an inserted fiber optic sensor. (b) Intradiscal pressure measurement result.

3.5 Summary

In this chapter, a miniature FP pressure sensor fabricated with a UV-molding process is presented. The sensor is composed of a UV-molded optical cavity and a polymer-metal composite diaphragm, which is fabricated at the end of a SMF with a pre-written FBG, rendering the sensor the capability of temperature compensation and simultaneous measurement of pressure and temperature. The mold used for UV-molding process is built by assembling a polished ferrule and a cleaved optical fiber, which eliminates the need for a costly semiconductor or direct machining process and enables high accuracy optical alignment of the mold and the sensing fiber. The sensor fabrication follows simple, repeatable processes and safe procedures, and uses less expensive materials and equipment. This fabrication method can also be used for batch fabrication or wafer scale fabrication with minor modifications to the processes. Due to the relatively low stiffness of the polymer-metal composite diaphragm, sensors with extra miniature sizes but a high sensitivity can be obtained. The experimental study of this sensor has shown that the sensor has a good linearity in the designed pressure range. Effective temperature compensation by using the built-in FBG has also been demonstrated. Since the materials used for the sensor housing and diaphragm have good biocompatibility, this sensor will become a favorable choice for biomedical applications such as arterial, intracranial, urethral, or intradiscal pressure measurements. In this work, in-vivo blood pressure measurement in an artery of the swine and in-vitro intradiscal pressure measurement by using the fabricated sensor

have been carried out, which demonstrate that these sensors hold great promise for biomedical applications.

Chapter 4 Hybrid Miniature Fabry-Perot Temperature and Pressure Sensor with Dual Optical Cavities for Simultaneous Pressure and Temperature Measurements

4.1. Introduction

As it is mentioned in the previous chapters, one of the most significant drawbacks of polymer based optical pressure sensors is their relatively large thermal sensitivity compared with silicon/glass based sensors. In the previous chapters, the temperature effect of the pressure sensing cavity was compensated by using a FBG temperature sensor. This method requires an extra temperature sensor, which would be placed at the same location as the pressure sensing region. However, since the embedded FBG has to be positioned at least several millimeters away from the pressure sensing FP cavity to avoid interference effect between the two sensors, it is difficult to obtain the exact temperature at the pressure sensing location. Moreover, adding a FBG sensor to the pressure sensor can be costly due to the fabrication cost of the FBG.

In this chapter, design, fabrication, and experimental study of a hybrid miniature dual-cavity fiber-optic pressure sensor with temperature sensing and temperature compensation capability is presented. As illustrated in Figure 4.1, the sensor employs an intrinsic FP cavity that is adjacent to the pressure sensing cavity to measure temperature selectively. The intrinsic FP cavity is made of SMF and dielectric optical coatings, which is fabricated by using E-beam evaporation, fiber splicing, and

cleaving processes. This design eliminates the need for an additional temperature sensor and enables accurate temperature measurement in the vicinity of the pressure sensing structure. To retrieve both temperature and pressure from the dual cavities, a frequency based demodulation scheme that is capable of acquiring the multiple cavity lengths separately from the spectrum signal is required.

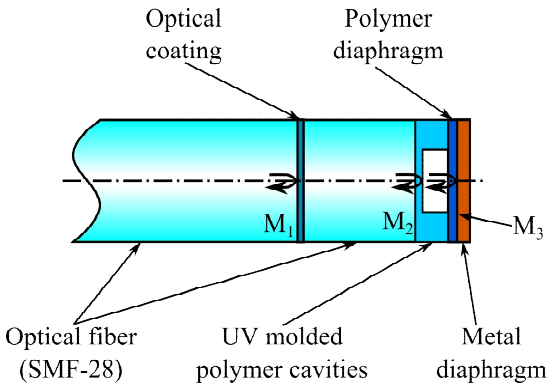

Figure 4.1: Schematic of the hybrid temperature/pressure sensor.

4.2. Sensor Design and Fabrication

In this work, a dual-cavity FP pressure sensor with built-in temperature measurement and compensation capability is designed. One of the cavities was formed between two internal mirrors: one mirror generated from evaporated dielectric films (M_1) and the other being the endface of a short segment of optical fiber (M_2), as shown in Figure 4.1. Since the spliced silica cavity is only sensitivity to temperature, this cavity is used to measure temperature. The other cavity is an air cavity formed between the end surface of the UV-molded cavity (M_2) and a polymer/metal

composite diaphragm (M_3), which is sensitive to both pressure and temperature change.

In order to acquire a good temperature sensing capability, the silica cavity has to be properly designed. The temperature sensitivity of the silica cavity length can be expressed as

$$TS_{silica} = (\frac{\alpha_{n\_silica}}{n_{silica}} + CTE_{silica})L_{silica} = (7.36\mu\varepsilon / °C)\, L_{silica} \quad (4.1)$$

where TS_{silica} is the temperature sensitivity of the silica cavity, α_{n_silica} is the thermo-optic coefficient, CTE_{silica} is the CTE of silica, and L_{silica} is the length of the silica cavity. Since the thermo-optic coefficient (1×10^{-4}/°C) and the CTE of silica (0.55 με/°C) are relatively low, in order to get a reasonable temperature sensitivity, the silica cavity length has to be as long as 1 mm to 3 mm [59,74]. However, a long cavity is not desirable in the design of a miniature fiber-optic sensor. To increase the temperature sensitivity of the sensor without increasing the length of the silica cavity a thin polymer layer (OP-4-20632 UV curable polymer, Dymax), which has a CTE that is 98 times larger (the CTE of the polymer: 54 με/°C) than that of silica and a thermo-optic coefficient of around -4×10^{-5}/°C. Therefore, the overall temperature sensitivity of the sensor can be rewritten as

$$TS_{overall} = (\frac{\alpha_{n\_\text{silica}}}{n_{silica}} + CTE_{silica})L_{silica} + (\frac{\alpha_{n\_polymer}}{n_{polymer}} + CTE_{polymer})L_{polymer} = (7.36\mu\varepsilon/°\text{C})L_{silica} + (28.34\mu\varepsilon/°\text{C})L_{polymer} \quad (4.2)$$

where $TS_{overall}$ is the overall temperature sensitivity of the sensor, $TS_{polymer}$ is the temperature sensitivity of the polymer cavity, α_{n_silica} and $\alpha_{n\_polymer}$ are the thermo-optic coefficients of silica and the UV curable polymer, respectively, CTE_{silica} and $CTE_{polymer}$ are the CTE of silica and the polymer material, respectively, L_{silica} and $L_{polymer}$ is the length of the polymer cavity, respectively. In this work, the silica cavity length and the added polymer thickness was chosen to be 250 μm and 35 μm, respectively, which enables a good temperature sensitivity of 2.8 nm/°C and a good temperature measurement resolution of less than 0.1 °C. In this fiber cavity, the light is guided mostly in a single mode, so that the beam divergence loss is negligible.

In order to obtain accurate measurement with the two optical cavities, the two cavities should also be carefully designed to ensure a good visibility of the multi-frequency interference fringes. Reflected intensities from the two internal mirrors that form the silica FP cavity can be tuned by changing the number of alternating layers of TiO_2 and SiO_2. Furthermore, the parameters used for splicing should be well chosen to obtain proper reflectivity of the first mirror (M_1) for a good spectrum visibility. In this work, the reflectivity of the first mirror was chosen to be 4%, the same as that of the second mirror (M_2) due to the Fresnel reflection between polymer and air. The

reflection between the fiber endface and the UV-curable polymer is negligible because of the small reflective index difference of those two materials.

The sensor is fabricated by using dielectric optical coating, fiber fusion splicing, fiber cleaving, UV-molding process, and metal-polymer composite thin film fabrication. Fabrication of the fiber cavity is very simple, which is composed of evaporation of alternating layers of titanium dioxide and silicon dioxide, splicing a short segment of SMF, and cleaving the fiber endface. The pressure sensing cavity was fabricated by using the UV-molding and metal-polymer composite diaphragm covering processes, which have been described in Section 3.2.

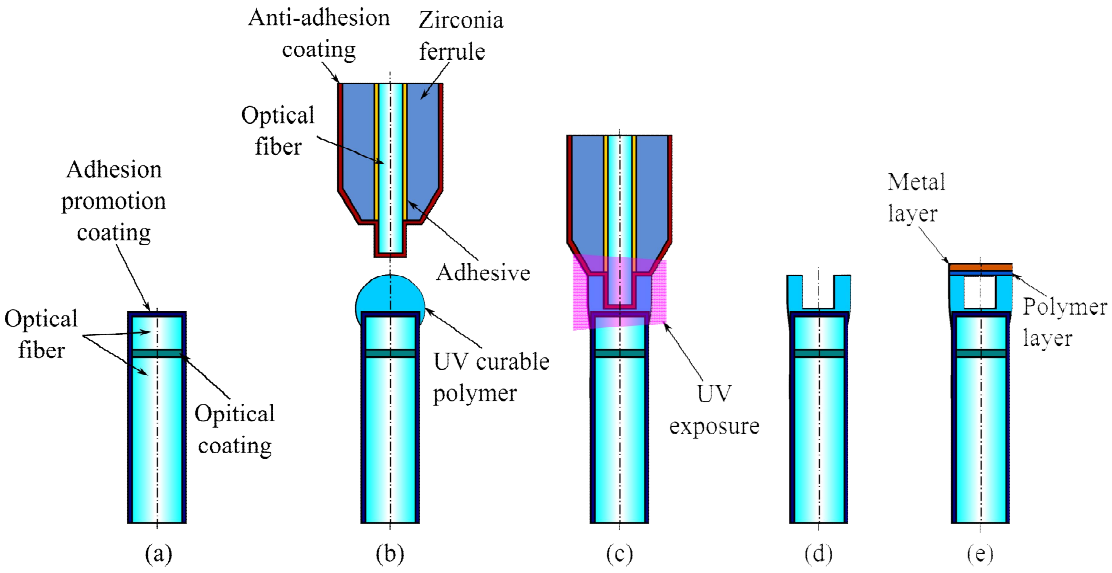

Figure 4.2: Fabrication process of the hybrid UV-molded temperature/pressure sensor.

The sensor fabrication is composed of three steps. The first step is to fabricate the silica optical cavity that is used for temperature measurement and compensation. The second step is to perform cavity molding. Finally, in the third step, a metal-polymer

composite diaphragm is covered over the molded cavity. The detailed fabrication process is shown in Figure 4.2. After a batch of SMFs (Corning, SMF-28e) were prepared by cleaving and cleaning, the fiber endfaces are coated with five alternating layers of TiO_2 and SiO_2, each with a quarter wavelength thickness (at λ = 1550 nm), by using electron beam evaporation. Another optical fiber was then spliced to the fiber with the optical coatings with empirically found conditions to get the designed reflectivity (≈ 5 %). The splicing was performed with a commercial fusion splicer (Hamamatsu, Type-36) with 2 arc count and 0.5s arc duration (a normal condition for SMF: 40 arc and 1.5s arc duration) in order to get desired reflectivity from the fabricated internal mirror [93–95]. The fiber was then cleaved under a microscope around 250 μm away from the spliced plane to form the silica FP cavity. After this, the sensor fabrication follows the exactly same processes as those described in the Chapter 3 for fabricating the UV-molded sensor, which includes adhesion chemical treatment, aligning mold, UV molding of cavity, and deposition of polymer/metal composite diaphragm.

4.3 Calibration and Evaluation of Sensors

4.3.1 Optical Interrogation System

In the experiment, the fabricated sensor was connected to a broadband optical interrogation system, which is consisted of a 2×2 coupler (Gould Fiber Optics), a broadband spectrometer (USB4000, Ocean Optics), and a broadband light source (HL-2000, Ocean Optics). The broadband spectrometer has a large wavelength

bandwidth from 700 nm to 1000 nm, which ensures a good optical frequency resolution during the initial data processing using FFT. The experimental arrangement for pressure and temperature calibration is identical to that described in the previous chapters [Figure 3.12(b)]. The spectrum of the multi-cavity sensor has a combination of distinctive optical frequencies, which are defined by the silica cavity, the air cavity, and the combination of those two cavities. The total intensity of interference can be written as [51]

$$\begin{aligned} I(\lambda) &= \left| A_1 - A_2 \exp\left(-\frac{j4\pi(L_{air})}{\lambda}\right) + A_3 \exp\left(-\frac{j4\pi(L_{air} + n_{silica}L_{silica} + n_{polymer}L_{polymer})}{\lambda}\right)\right|^2 \\ &= A_1^2 + A_2^2 + A_3^2 - 2A_1A_2\cos\left(\frac{4\pi L_{air}}{\lambda}\right) - 2A_2A_3\cos\left(\frac{4\pi(n_{silica}L_{silica} + n_{polymer}L_{polymer})}{\lambda}\right) \\ &\quad + 2A_3A_1\cos\left(\frac{4\pi(L_{air} + n_{silica}L_{silica} + n_{polymer}L_{polymer})}{\lambda}\right), \end{aligned} \quad (4.3)$$

where A_1, A_2, and A_3 are the amplitudes of the reflected electric fields from the internal mirrors, the air cavity bottom, and the composite diaphragm, respectively, n_{silica} and $n_{polymer}$ are the refractive indiecs of the SMF core, the UV-curable polymer, respectively, L_{silica}, $L_{polymer}$, and L_{air} are the lengths of the intrinsic silica cavity, the intrinsic polymer cavity, and the air cavity, respectively, and λ is the wavelength.

Representative interference spectra obtained from the sensor using an optical interrogation system (HL-2000 broadband light source and USB4000 spectrometer from Ocean Optics) are shown in Figure 4.3. The lower frequency in the spectra corresponds to the air cavity and the higher frequencies in the spectra are due to the silica cavity and the combination of silica and air cavities.

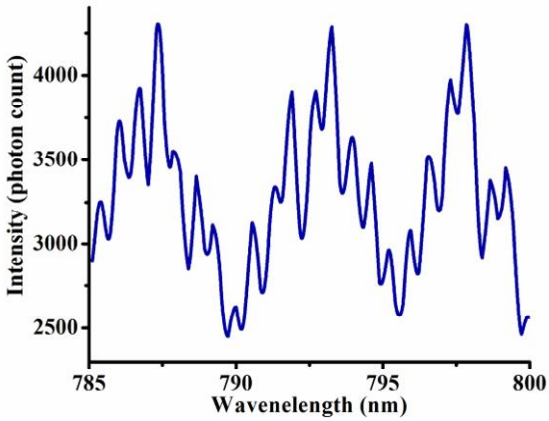

Figure 4.3: An interference spectrum of the fabricated sensor obtained with Ocean Optics USB4000.

In order to retrieve the two cavities independently, optical frequency spectrum based signal processing was adopted. The acquired wavelength spectrum was first converted to the wavenumber domain. Since the obtained wavenumber spectrum is not evenly spaced, cubic spline interpolation and resampling were performed. FFT was then applied to the resampled spectrum and the optical frequencies were determined. The relationship between the measured optical frequency and actual optical cavity length can be described as

$$L = \frac{f}{2n}, \tag{4.4}$$

where f is the optical frequency, L is the optical cavity length, and n is the refractive index of the FP cavity. Figure 4.4 shows FFT result of a sensor wavenumber spectrum. The three peaks shown in the figure correspond to the three optical cavities of the sensor. The cavity lengths obtained from the FFT result are 56.621, 286.069, and 343.265 μm, respectively. These measured optical frequencies are then chosen as

the center frequencies of band-pass Butterworth filters to extract the single frequency signal at the frequency of interest. Figure 4.5 shows the filtered wavelength spectra by using two different band-pass filters whose center frequencies are corresponding to the two peaks (f_1 and f_3) in the FFT result shown in Figure 4.4. After obtaining the spectrum with a single frequency matching to each cavity length, one peak tracing method is used to retrieve the value of the cavity length.

In order to calculate the peak constant to be used in one peak tracing method, the cavity length was calculated from two adjacent peak-wavelengths based on Equation 1.9. By using the one peak tracing method, the cavity length can be measured with a high resolution (0.2 nm with USB4000 spectrometer), which is much higher than that obtained directly from the FFT method (845.1 nm with the same spectrometer).

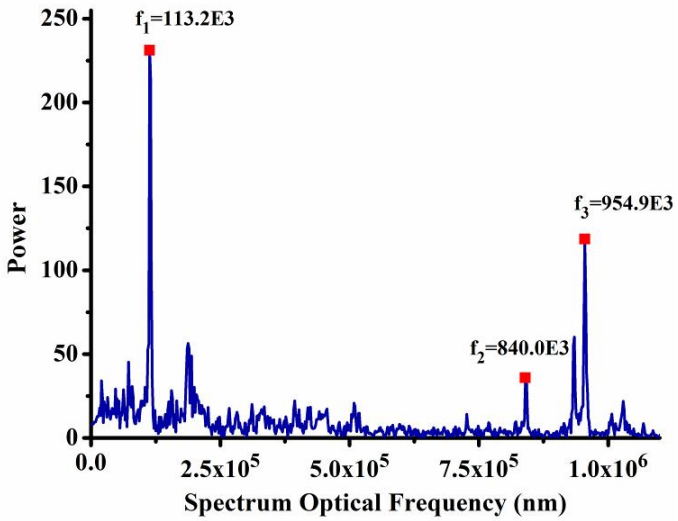

Figure 4.4: FFT result from the wavenumber spectrum of the sensor.

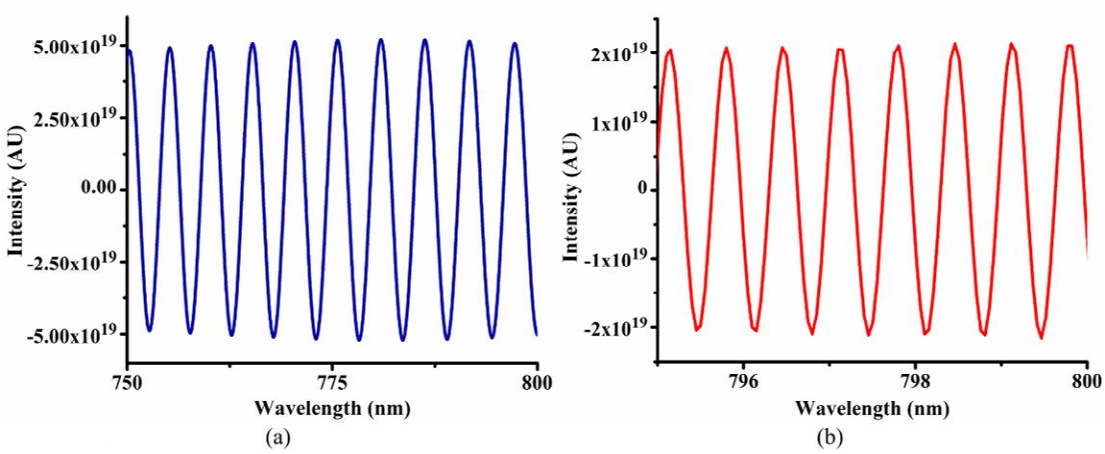

Figure 4.5: Filtered wavelength spectrum for (a) the air cavity and (b) the combined cavity of air and silica fiber.

In literature, a method that uses curve fitting to the filtered spectrum in order to increase the accuracy for determining the cavity length has been reported [70]. However, this method is computationally costly since it needs to utilize the entire spectrum to get a fitted curve and requires iterative calculations. In this work, a novel signal processing scheme is developed, which makes use of selective curve fitting to the filter spectrum and the one peak tracing method. By using this method, the calculation time can be reduced significantly (around 20 times faster according to the simulation) because the curve fitting is only performed at the vicinity of each peak and iteration is not required. Moreover, high resolution measurement can be achieved due to the nature of the one peak tracking method [69]. A detailed description of the one peak tracing method has been described in Section 1.2.3.

A parametric study was carried out to compare the performance of the demodulation scheme developed in this work with that reported in literature in terms

of calculation time and linearity of the fitted curve. In the simulations, a sensor with two cavities with initial cavity lengths of 60 μm and 100 μm were used. In each iteration, both of the two cavity lengths were varied by 0.05 μm with a step of 0.001 μm (i.e., 60.000 μm cavity was increased to 60.050 μm and 100.000 μm cavity to 100.050 μm with 0.001 μm step). The cavity length changes were retrieved from the simulated spectrum by using the conventional spectrum curve fitting and the method developed in this work. R^2 values were calculated as functions of SNR using the two different method. Figure 4.6 shows the comparison of the calculated R^2 values with two different demodulation methods for determination of the two cavities. Both of the methods were able to retrieve the cavity length change very well while the SNR is high. However, when the SNR is low, the one-peak-tracing with band-pass filtering method shows a better resilience to noise over the conventional spectrum curve fitting method. Moreover, it is also noted that the method developed in this work was about 20 times faster than the conventional spectrum curve fitting method; for the one peak tracking with band-pass filtering method, the calculation speed was 0.43s per data point, while for the conventional spectrum curve fitting method, it was 8.46s per data point.

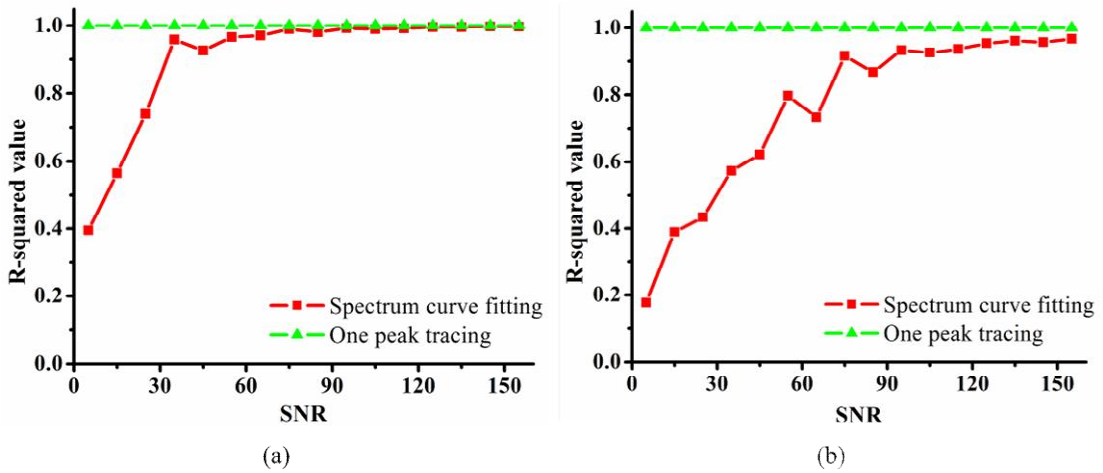

Figure 4.6: Comparison of R^2 values as a function of SNR by using two different demodulation schemes (spectrum curve fitting and one peak tracking of the filtered spectrum) for cavity lengths: (a) 60 μm and (b) 100 μm.

4.3.2 Sensor Calibration

The calibration of the sensor for pressure measurement was performed in a pressure chamber with a reference pressure sensor, as shown in Figure 4.7. A conventional pressure sensor (LL-080-35A, Kulite Semiconductor) was used as the reference. The internal chamber pressure was controlled by using a pressure regulator (Pressure Regulator Type 70, Marsh Bellofram), which has a pressure range of 0 to 30 psi. Temperature control was achieved by using a thermo controller (Omega Engineering Inc., CN77333), a polyimide-insulated flexible thermocouple (Omega Engineering Inc., CO1-K), and two polyimide-insulated flexible heaters (Omega Engineering Inc., KH 103/10). The heaters were place above and below the pressure sensor to control the temperature locally, while minimizing the heating time and the temperature effect of the reference pressure sensor.

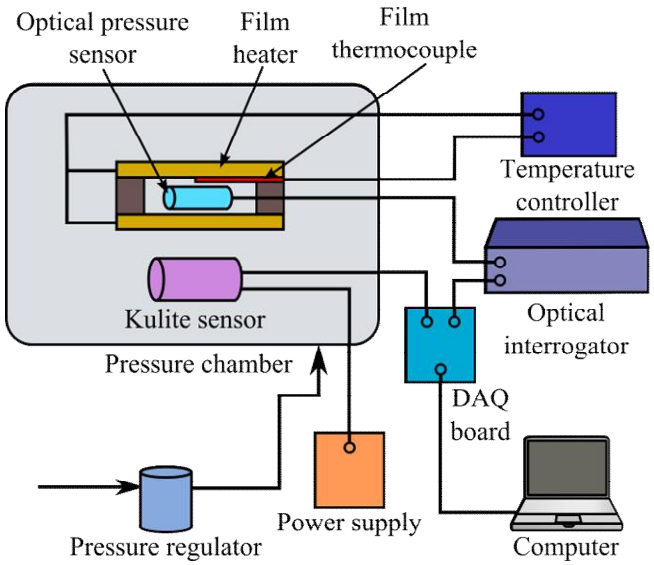

Figure 4.7: Pressure and temperature calibration setup.

In the experiments, the pressure in the chamber was first increased and then decreased with a step of 0.2 psi within a range of 1.0 psi to 4.0 psi at a room temperature of 26 °C. The calibration result of the sensor is shown in Figure 4.8. It can be seen that the sensor exhibits a good linearity (R^2 = 0.9993) over the entire tested pressure range. Based on linear regression analysis of the measured data, the pressure sensitivities were calculated to be 0.084 μm/psi. This result is slightly smaller than the value obtained from the numerical simulations (0.100 μm/psi). Residual stresses generated during the polymerization and metallization process of the diaphragm are the possible reasons for the lower measured sensitivity. Furthermore, the sputtering process induced a curvature in the diaphragm, which further reduces the pressure sensitivity. The hysteresis error of the sensor is obtained to be 2.3 %. In the calibrations, the small zero drift and non-linearity of the

calibration curves are believed to be due to temperature variations from the temperature controller and random errors from the interrogation system.

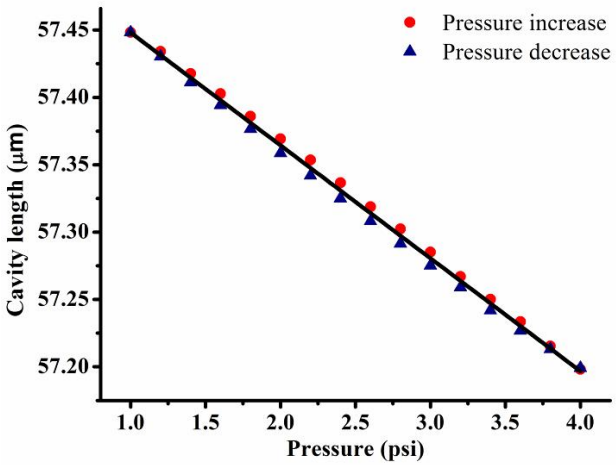

Figure 4.8: Pressure calibration curves of the sensor at 26.0 ℃.

To evaluate the temperature effect, the pressure sensitivity calibration for both the air cavity and the silica cavity was performed at different temperatures (e.g., 26 °C, 34 °C, 42 °C, and 50 °C) by using the experimental setup shown in Figure 4.7. The pressure calibration result of the air cavity is shown in Figure 4.9(a). In all four cases, the measurement results show good linearity ($R^2 > 0.9994$) over the measured pressure range. However, it is noted that there is temperature dependency of the pressure sensitivities. This deviation of the sensitivity value is believed to be due to the property change of the polymer layer in the polymer/metal composite diaphragm. In Figure 4.9(b), the pressure sensitivities of the silica cavity at the four different temperatures are shown. It can be seen that due to the high elastic modulus of silica (71.7 GPa), the cavity length change of the temperature sensing cavity with respect to

pressure was negligible in the pressure range of 1.0 psi to 4.0 psi at all four temperatures. The slight fluctuations of the cavity length are believed to be due to the random noise from the measurement system and temperature fluctuations from the temperature controller.

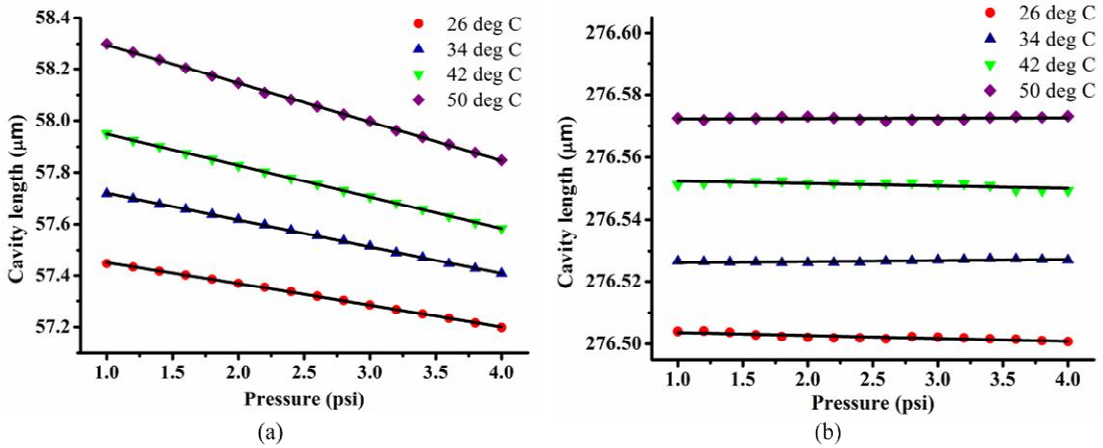

Figure 4.9: Pressure calibration curves: (a) air cavity and (b) silica cavity at four different temperatures (26.0 °C, 34.0 °C, 42.0 °C, and 50.0 °C).

4.3.3 Temperature Sensitivity and Temperature Compensation

As discussed previously, the silica FP cavity in the fabricated sensor can be used as a temperature sensor due to its linear response to temperature change and low pressure sensitivity. On the other hand, the temperature reading from the silica cavity can be used to compensate for the relatively large temperature drift of the pressure sensing cavity due to the large CTE of polymer material and air expansion in the polymer cavity. To evaluate the temperature sensing performance of the silica cavity and the temperature compensation capability of the sensor, temperature calibration of

the two cavities was performed in the pressure chamber with a temperature controller, as shown in Figure 4.7.

First, the temperature sensitivity of the air cavity was evaluated. In the experiment, the temperature sensitivity of the cavity was measured by monitoring the cavity length change of the air FP cavity with respect to the temperature change. To measure the temperature sensitivity, the sensor was heated from 26 °C to 50 °C with an increment of 2 °C under four different pressure levels (1.0 psi, 2.0 psi, 3.0 psi, and 4.0 psi). The cavity lengths were recorded as a function of temperature at each pressure level. The obtained temperature calibration results of the air FP cavity are shown in Figure 4.10(a). According to the result, a linear relationship between the air cavity length and temperature can be observed with a good linearity ($R^2_{average} = 0.9939$). The temperature sensitivity of the silica FP cavity was found to be almost the same at different pressure levels, which was measured to be 0.0137 μm/°C.

Next, the temperature sensitivity and temperature resolution of the silica FP cavity were investigated. Using the same experimental arrangement and method, the temperature calibration results for the silica cavity at several different pressures are obtained, as shown in Figure 4.10(b). The calibration results exhibit a good linearity ($R^2_{average} = 0.9990$) and the silica cavity is found again to be not sensitive to the pressure change. The temperature sensitivity and resolution of the FP pressure sensor were obtained as 0.0028 μm/°C and 0.10 °C, respectively. The sensitivity of the silica cavity is 26 times larger than that of the dual cavity sensor reported by Pevec and

Donlagic [74], even though the silica FP cavity length used in this work (276.5 μm) is much smaller than that of the previous work (~1 mm). By using the polymer material, a high temperature sensitivity (as well as a high resolution) was achieved with a smaller form factor compared to a sensor with a pure silica material.

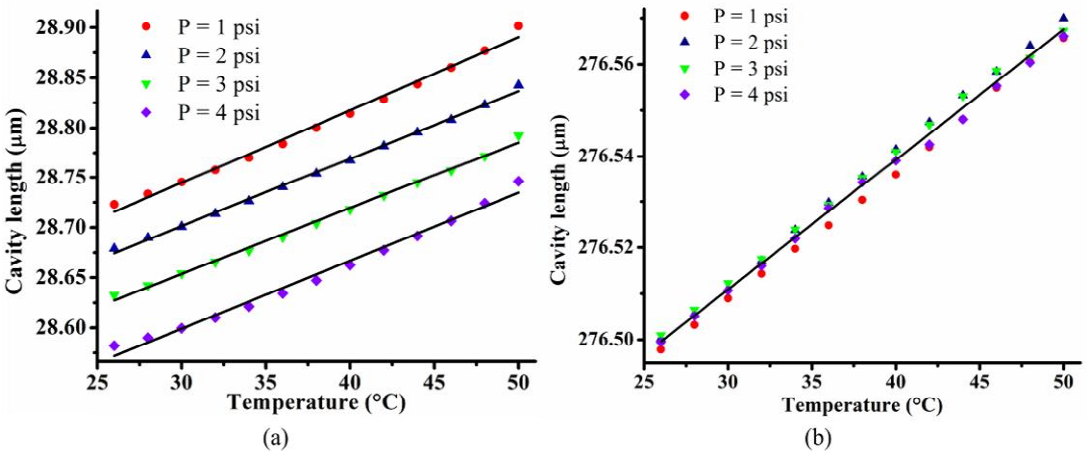

Figure 4.10: Temperature calibration curves: (a) air cavity and (b) silica cavity at four different pressure levels of 1.0 psi, 2.0 psi, 3.0 psi, and 4.0 psi.

In order to compensate for the temperature effect of the pressure sensing cavity, temperature readings from the silica cavity are used along with the temperature sensitivity of the pressure sensing cavity. It is noted that the pressure sensitivity of the sensor varies from 84.0 nm/psi to 150.0 nm/psi in the temperature range of 26 °C to 50 °C. This large sensitivity change is believed to be due to softening of the polymer layer in the polymer/metal composite diaphragm. Since in this sensor, the portion of the polymer layer in the composite diaphragm is larger than that in the sensor developed in Chapter 3, the temperature induced pressure sensitivity change also

becomes larger than that in the previous sensor. The pressure sensitivity as a function of the temperature is shown in Figure 4.11.

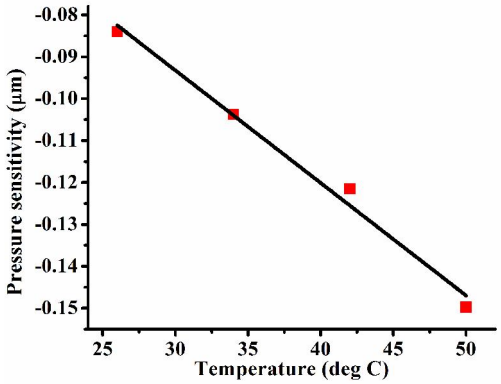

Figure 4.11: Pressure sensitivity of the pressure sensing cavity as a function of temperature.

By using the relationship between the pressure sensitivity and the temperature, the pressure sensitivity can be measured at any temperature, which can be obtained as

$$PS_{air\ cavity} = -(0.00269T + 0.01265)\mu m / psi\,, \tag{4.5}$$

where $PS_{air\ cavity}$ is the pressure sensitivity of the air cavity and T is the temperature. The measured pressure sensitivity can then be used to compensate the temperature effect at each measurement. As shown in Figures 4.9 and 4.10, the lengths of the air and the silica cavities change linearly with respect to both pressure and temperature ($R^2_{average} = 0.994$). Therefore, these linear relationships can be expressed in a matrix form as the following [81] [73]:

$$\begin{bmatrix} \Delta L_{silica} \\ \Delta L_{air} \end{bmatrix} = \begin{bmatrix} 0 & 0.0028\,\mu m/°C \\ PS_{air\ cavity} & 13.6\,nm/°C \end{bmatrix} \begin{bmatrix} \Delta P \\ \Delta T \end{bmatrix} = S \begin{bmatrix} \Delta P \\ \Delta T \end{bmatrix}, \tag{4.6}$$

where ΔL_{silica} is cavity length change of the silica cavity, ΔL_{air} is cavity length change of the air cavity, ΔP and ΔT is the pressure change and temperature change, respectively. Pressure sensitivity of the silica cavity can be ignored, according to the results shown in Figure 4.9 (b). By taking the inverse of the sensitivity matrix S, Eq. (4.6) can be rewritten as:

$$\begin{bmatrix} \Delta P \\ \Delta T \end{bmatrix} = S^{-1} \begin{bmatrix} \Delta \lambda_{FBG} \\ \Delta L \end{bmatrix} \tag{4.7}$$

Based on Eq. (4.7), by using an optical system (e.g., the system shown in Figure 4.7), which can measure both FP cavity length changes, temperature and pressure values can be retrieved simultaneously.

4.4 Summary

In this chapter, a hybrid dual optical cavity fiber optic pressure and temperature sensor is presented. The sensor, which is made at the end of a SMF, is composed of an E-beam deposited dielectric coating, a segment of an optical fiber, a UV-molded optical cavity, and a polymer-metal composite diaphragm. The intrinsic silica cavity formed between several layers of dielectric optical coating and an optical fiber endface renders the sensor the capability of temperature compensation and simultaneous pressure and temperature measurement. The fabrication of the extrinsic air cavity was performed by using a UV molding process. It was found that the large thermal expansion of the polymer material contributes to the high temperature sensitivity of the sensor. Experimental studies of this sensor have shown that the

sensor has good linearity for pressure measurement in the designed pressure range. Effective temperature compensation by using the embedded intrinsic silica cavity has also been demonstrated. Furthermore, a signal processing method has been developed, which enables to resolve multiple cavity lengths for multiplexed FP sensors or a FP sensor with multiple cavities. Compared with the methods reported in literature, this method renders much shorter calculation time, higher resolution, and better resilience to noise.

Chapter 5 Summary and Future Work

5.1 Summary of Dissertation Work

Optical pressure sensors have been widely used in many applications due to their inherent advantages over conventional sensors. Most of current fiber optic pressure sensors are built with glass/silicon materials due to the good chemical and thermal stability of the materials. However, the fabrication of these sensors is usually costly and involves strong acid based etching and high temperature fusion bonding. Further, the high modulus of elasticity of glass/silicon materials can limit the sensitivity of the sensors since it is difficult to obtain a thin diaphragm (< 1μm) with these materials. On the other hand, a polymer based fiber optic pressure sensor is easy to fabricate by using conventional polymer processing (e.g., photolithography and imprinting lithography). A sensor diaphragm made of polymer or polymer-metal composite has much smaller stiffness than a silicon diaphragm. A high sensitivity can thus be obtained easily with a diaphragm of the same thickness and size. Moreover, there is a large variety of polymer materials that can be selected based on specific requirements of applications, which include temperature stability, chemical stability, and biocompatibility. However, one of the most significant drawbacks of polymer-based sensors is its large temperature dependency. Therefore, temperature compensation becomes critical for achieving accurate pressure measurements with those sensors.

In this dissertation work, three types of polymer based FP fiber-optic pressure sensors for a static or quasistatic measurement with temperature compensation

capability have been designed, fabricated, and studied. The first type of sensor is based on self-aligned and maskless photolithography, the second is based on a unique UV-molding process with an optical fiber based mold, and the third is based on a UV-molding and silica fusion bonding processes. The performance of all three types of sensors has been characterized through extensive experimental studies. The first type of sensor has been studied under both static and dynamic pressures. The second type of sensor has been successfully demonstrated for in-vivo blood pressure measurement and intradiscal pressure measurement. All three sensors have temperature compensation capability. The two types of sensors employ a FBG as a temperature sensor to simultaneously measure pressure and temperature as well as provide temperature compensation. The third type of sensor employs a hybrid dual FP cavity structure for simultaneous temperature and pressure measurement and temperature compensation. All three types of sensors discussed in this dissertation have the water absorption issue due to the polymer cavity structure. This phenomenon results in drifts of pressure reading especially in a water-rich environment. Therefore, this issue should be handled correctly by using a polymer material with low water absorption or a hydrophobic material coating.

The original contributions in this dissertation work are summarized as follows.

Contribution 1: A polymer fiber optic pressure sensor based on self-aligned photolithography with temperature sensing/compensation capability has been developed.

The sensor makes use of a unique fabrication method, in which the optical fiber is used as a waveguide for a photolithography. This fabrication method eliminates a need for an expensive UV exposure and alignment system and enables a high accuracy self-aligned process. Based on this fabrication method, two types of miniature fiber optic pressure sensors with a built-in FBG for temperature compensation have been developed: one being a co-axial sensor and the other being a cross-axial sensor. The experimental results have successfully demonstrated that the fabricated sensors can be used for static and dynamic pressure measurements with temperature sensing/compensation capabilities.

Contribution 2: Enhance understanding of a Fabry-Perot cavity fabricated on the sidewall of an optical fiber has been achieved.

Optical analysis on a co-axial sensor has been performed by using the transfer matrix method and the generalized Collins integral. The effect of the curvature in one of the partial mirror on the optical intensity and the visibility of the interference have been investigated for achieving a better understanding of the co-axial FP sensor. This optical analysis can help develop design guidelines for a co-axial FP sensor to obtain better performance.

Contribution 3: Polymer based fiber optic pressure sensors fabricated by using a UV molding process with temperature sensing/compensation capability have been developed.

A UV molding method has been used to fabricate a fiber optic FP pressure sensor for the first time. An optical fiber based mold for the cavity replication has been developed, which enables high accuracy alignment between the fabricated mold and the sensing optical fiber. This fabrication method renders a low cost, repeatable, and eco-friendly process, which can be further adapted to achieve batch fabrication of high performance polymer based fiber optic pressure sensors. The sensor has been demonstrated to have a good linearity and resolution in the designed pressure range. Temperature compensation has also been demonstrated successfully by using a built-in FBG. In-vivo blood pressure measurement and in-vitro intradiscal pressure measurement of a swine with the fabricated sensor have been carried out, which demonstrate that these sensors hold great promise for biomedical applications.

Contribution 4: A hybrid dual cavity FP pressure sensor with temperature sensing/compensation capability has been developed.

The sensor employs a unique dual cavity structure, which includes an intrinsic silica cavity formed between a dielectric coating and the endface of a short optical fiber segment, and a UV-molded pressure sensing cavity. The silica cavity is located adjacent to the pressure sensing cavity and used as a temperature sensor. By using the dual cavity design, the overall length of the sensor is only around 300 μm, which is much smaller than the other two types of sensors with a FBG temperature sensor (~ 1cm). Experimental studies of the sensor have shown that a high temperature

sensitivity and a high pressure sensitivity can be obtained owing to low elastic modulus and high thermal expansion of the polymer material.

Contribution 5: An optical demodulation method has been developed, which enables fast and high accuracy signal interrogation for multiplexed FP sensors or a multi-cavity FP sensor.

This demodulation method is based on combination of frequency filtering, selective curve fitting, and one peak tracing**.** Based on simulation results, this method has been demonstrated to be able to effectively resolve multiple FP cavity lengths with a much better accuracy, a shorter calculation time, and less noise dependency, compared with the method reported in literature. This demodulation method has been successfully applied in the experiments for interrogation of the hybrid fiber optic pressure sensor with dual FP cavities.

5.2 Future Work

Upon the completion of this dissertation work, the future work is suggested as follows.

1) **Develop a surface mountable sensor with distributed sensing capability by using the UV molding process.**

The UV molding method can be used to fabricate a surface mountable co-axial sensor by using the optical alignment scheme discussed in Chapter 3. Multiple surface mountable sensors can be connected in series by using the 45° partial mirrors

in the sensors. Therefore, a surface mountable FP sensor array, which can be used for distributed pressure sensing can be designed and fabricated. To the best knowledge of the author, a distributed pressure sensor array with multiple FP cavities and surface mountable capability has never been reported. The interrogation of the sensor array can be performed by using demodulation method developed in Chapter 4. This future study will open the door for new applications of FP fiber optic pressure sensors in biomedical and industrial fields.

2) **Carry out studies to address the water absorption problem of the polymer structure.**

The water absorption of the polymer structure is one of the most significant drawbacks of the polymer based pressure/temperature sensor, which affects pressure reading while the polymer based sensors are in a water-based solution or a water-rich environment. However, this issue has not been addressed in this dissertation since the issue requires a good amount of research effort by itself. The issue can be resolved or alleviated by covering the polymer structure with a metal or a dielectric material. In order to prevent the water absorption, the polymer surface should be completely coated with a suitable material. Therefore, it is recommended to use plating or dipping method to achieve the desired waterproof condition. Electro/electroless plating of metal or solution based hydrophobic dielectric coating can be good candidates to achieve the prevention of water absorption.

3) **Develop a wafer scale batch fabrication method for polymer based sensors.**

In this dissertation work, three different types of sensors were developed. However, in order to push these sensors for commercialization, not only the performance of the sensors should be comparable to the commercial available counterparts but also the fabrication cost should be much lower. A low cost fabrication process can enable the sensors to be disposable, which can be a great advantage for sensors used in biomedical applications. Wafer scale batch fabrication of the sensors will significantly reduce the fabrication cost of the sensors, improve the uniformity of the sensors, and enable the technology to be used as disposable sensors for medical application. To achieve the wafer scale batch fabrication, investigation into the mounting method of fibers in a wafer, wafer-to-wafer alignment schemes, and modification of processes for wafer scale process.

4) **Develop a statistical sensor calibration model based on machine learning process for simultaneous temperature and pressure measurement.**

It was shown that the hybrid temperature/pressure sensor has large sensitivity variations over the measured temperature range. In order to reduce overall measurement error, a statistical sensor calibration model should be developed, which can accommodate nonlinear behaviors of the sensor. A regression based model can be used with a measured data set to obtain a model with a better accuracy. It is expected that these models can predict temperature and pressure with a better accuracy than the linear model, especially when a sensor exhibits a large deviation from the linear approximation.

Appendix A: Matlab codes and LabView code

A.1. Matlab codes for intensity calculation of the surface mountable sensor

File name: FirstBeam_Reflected_Intensity_Profile_along_x_axis.m

```
clc
clear all
close all

%Parameters
R = 62.5;
D = 30;
n1=1.4682;
n2=1.0003;
lamda1 = 1.55/n1;
lamda2 = 1.55/n2;
wx= 4.6;
wy= 4.6;
k1 = 2*pi/lamda1;
R1 = ((n1-n2)/(n1+n2))^2;
T1 = 1-R;

L1 = 62.499999999999;
L2 = 62.499999999999;

x2 = -20:0.001:20;
y2 = 0;

A1 = -1i*exp(1i*k1*(L1+L2))*sqrt(R)/lamda1/((L1*R-
2*L1*L2+L2*R)*(L1+L2))^0.5;
B1 = 1i*pi/lamda1*(R-2*L2)/(L1*R-2*L1*L2+L2*R)-1/wx^2;
C1 = 1i*pi/lamda1/(L1+L2)-1/wy^2;
D1 = 1i*pi/lamda1/(R-2*L1)/2*L1/(R-L1);
E1 = 1i*pi/lamda1/2/L1;
F1 = -1i*pi*R/lamda1/L1/(R-L1);
G1 = -1i*pi/lamda1/L1;

E_2 = pi*A1/(B1*C1)^0.5*exp((D1-F1^2/4/B1)*x2.^2+(E1-
G1^2/4/C1)*y2.^2);
I_2 = R1*abs(E_2).^2;
max_intensity = max(I_2);

disp(['Maximum intensity: ' num2str(max_intensity)])

figure('Position',[20 50 600 350]);
plot(x2,I_2,'-r', 'linewidth', 3)
xlabel('Position along x axis (um)')
```

```
ylabel('Normalized intensity')
```

File name: FirstBeam_Reflected_Intensity_Profile_along_y_axis.m

```
clc
clear all
close all

%Parameters
R = 62.5;
D = 30;
n1=1.4682;
n2=1.0003;
lamda1 = 1.55/n1;
lamda2 = 1.55/n2;
wx=4.6;
wy=4.6;
k1 = 2*pi/lamda1;
R1 = ((n1-n2)/(n1+n2))^2;
T1 = 1-R;

% L1 = 62.499999999999;
% L2 = 62.499999999999;
L1 = 62.499999999999;
L2 = 62.499999999999;

x2 = 0;

y2 = -20:0.001:20;

A1 = -1i*exp(1i*k1*(L1+L2))*sqrt(R)/lamda1/((L1*R-
2*L1*L2+L2.*R)*(L1+L2))^0.5;
B1 = 1i*pi/lamda1*(R-2*L2)/(L1*R-2*L1*L2+L2*R)-1/wx^2;
C1 = 1i*pi/lamda1/(L1+L2)-1/wy^2;
D1 = 1i*pi*(R-2*L1)/2/lamda1/L1/(R-L1);
E1 = 1i*pi/2/lamda1/L1;
F1 = -1i*pi*R/lamda1/L1/(R-L1);
G1 = -1i*pi/lamda1/L1;

E_2 = pi*A1/(B1*C1)^0.5*exp((D1-F1^2/4/B1)*x2.^2+(E1-
G1^2/4/C1)*y2.^2);
I_2 = R1*abs(E_2).^2;
max_intensity = max(I_2);

disp(['Maximum intensity: ' num2str(max_intensity)])

figure('Position',[20 50 600 350]);
plot(y2,I_2,'-b', 'linewidth', 3)
xlabel('Position along y axis (um)')
ylabel('Normalized intensity')
```

File name: FirstBeam_Intensity_analysis_z_axis_R.m

```
clc
clear all
close all

%Parameters
r = 62.5;
D = 30;
n1=1.4682;
n2=1.0003;
lamda1 = 1.55/n1;
lamda2 = 1.55/n2;
wx=4.6;
wy=4.6;
k1 = 2*pi/lamda1;
R = ((n1-n2)/(n1+n2))^2;
T = 1-R;

l1 = 62.499999999999;
l2 = 0:0.1:70;

x2 = 0;
y2 = 0;
%y2 = -20:0.005:20;

% First beam - Cylindrical mirror

A2 = -i*exp(i*k1.*(l1+l2))*sqrt(r)/lamda1./((l1*r-
2*l1.*l2+l2.*r).*(l1+l2)).^0.5;
B2 = i*pi/lamda1*(r-2*l2)./(l1*r-2*l1*l2+l2*r)-1/wx^2;
C2 = i*pi/lamda1./(l1+l2)-1/wy^2;
D2 = i*pi*(r-2*l1)/2/lamda1/l1/(r-l1);
E2 = i*pi/2/lamda1/l1;
F2 = -i*pi*r/lamda1/l1/(r-l1);
G2 = -i*pi/lamda1/l1;

EF2 = pi.*A2./(B2.*C2).^0.5.*exp((D2-F2^2/4./B2).*x2^2+(E2-
G2^2/4./C2).*y2^2);
I2 = R*abs(EF2).^2;
max(I2)

figure('Position',[300 360 600 310]);
hold on
plot(l2,I2,'-m', 'linewidth', 3)

% First beam - Flat mirror

A3 = -i*exp(i*k1.*(l1+l2))/lamda1./(l1+l2);
B3 = i*pi/lamda1./(l1+l2)-1/wx^2;
C3 = i*pi/lamda1./(l1+l2)-1/wy^2;
```

```
D3 = i*pi/lamda1./(l1+l2);
E3 = i*pi/lamda1./(l1+l2);
F3 = -i*pi/lamda1./(l1+l2);
G3 = -i*pi/lamda1./(l1+l2);

EF3 = pi.*A3./(B3.*C3).^0.5.*exp((D3-F3.^2/4./B3).*x2^2+(E3-
G3.^2/4./C3).*y2^2);
I3 = R*abs(EF3).^2;
max(I3)
plot(l2,I3,'--g', 'linewidth', 3)

% First beam - Spherical mirror

A4 = -i*exp(i*k1.*(l1+l2))/lamda1./((1-2.*l2/r)*l1+l2);
B4 = (i*pi/lamda1).*(-1*(1-2.*l2/r)./(-l1*r+2*l1.*l2-r.*l2)*r-
(1/wx^2));
C4 = (i*pi/lamda1)*-1.*(1-2.*l2/r)*r./(-l1*r+2*l1.*l2-l2.*r)-
(1/wy^2);
D4 = (i*pi/lamda1)*-1*(-2/r*l1+1)./(-l1*r+2*l1.*l2-r.*l2)*r;
E4 = (i*pi/lamda1)*-1*(-2/r*l1+1)*r./(-l1*r+2*l1.*l2-l2.*r);
F4 = (i*pi/lamda1)*2./(-l1*r+2*l1.*l2-l2.*r)*r;
G4 = (i*pi/lamda1)*2*r./(-l1*r+2*l1.*l2-l2.*r);

EF4 = pi.*A4./(B4.*C4).^0.5.*exp((D4-F4.^2/4./B4).*x2^2+(E4-
G4.^2/4./C4).*y2^2);
I4 = R*abs(EF4).^2;
max(I4)

plot(l2,I4,'--b', 'linewidth', 3)
xlabel('Position along z axis (um)')
ylabel('Normalized intensity')
vline(0,'-.b','mirror surface');
vline(31.25,'-.b','focus of mirror');
vline(62.5,'-.b','center of fiber');
%hline(1,'-.r');
legend('Curved mirror','Flat mirror', 'Spherical mirror',1)
```

A.2. Matlab codes for one peak tracing to retrieve cavity length from a single optical cavity

File name: Best_R2_main_code.m

```
clear; close all; clc;
pressure_list = [685 725 765 805 845 885 925 965 1005 1045 1085 1125
1165]';
file_ext = 'ProcSpec';
span_arr = 60:1:90; % Span for curve fitting to find a peak
wavelength from each peak
```

```
for k = 1:length(span_arr)
    [cavity(:,k),R2_arr(k)] = ...

calCavityLength_Ver2_7_up_total(pressure_list,file_ext,span_arr(k));
    clc;
    disp(['Percentage completed: ' num2str(100*k/length(span_arr))
'%']);
end
figure('Position',[700 300 400 300])
plot(span_arr,R2_arr,'bo','MarkerSize',4)
xlabel('Span')
ylabel('R sqaured')
[R2_max,index] = max(R2_arr);
cavity_opt = cavity(:,index);
hold on
plot(span_arr(index),R2_arr(index),'rx','MarkerSize',8,'MarkerFaceCo
lor','r')
text(span_arr(index),R2_arr(index),num2str(R2_max));

disp(['Cavity length having the best R2(' num2str(R2_max) '):'])
for k = 1:length(pressure_list);

fprintf(1,'%10.4f\t%10.5f\t\n',pressure_list(k),cavity_opt(k)*1e6);
end

figure('Position',[200 300 400 300])
plot(pressure_list,cavity_opt,'bo','MarkerSize',5)
hold on
p_res = polyfit(pressure_list,cavity_opt,1);
plot(pressure_list,polyval(p_res,pressure_list),'r-','LineWidth',2)
xlabel('Pressure')
ylabel('Cavity length')
```

File name: calCavityLength_Ver2_7_total

```
function [cavity,R2] =
calCavityLength_Ver2_7(pressure_list,file_ext,span,output_file)
%   Calculate the cavity length of a Fabry-Perot sensor based on the
%   spectrum analyzer results. For trasmitting type, double the
%   returned value.
%
%   The responses of the sensor to various pressures are stored in
%   an ascii file with the file name of ###.ext, where ### is the
%   pressure value and ext is the file extension name, e.g.
%   100.ProcSpec. It's assumed the first and second columns in this
%   file are the wavelengths and intensity, respectively. The
%   calculated cavity length along with the corresponding pressure
%   value will be exported to an external file for post processing,
%   if a third argument is provided.
%
```

```
%   Syntax: cavity =
%   calCavityLength(pressure_list,file_ext,output_file)
%       pressure_list is a vector of pressure values, file_ext is
%   theextension name of the stored data, and output_file is the
%   file for exporting the resulls.
%
%   Upon execution, this program displays the raw data, asks the
%   user to specified two points defining the usable wavelength
%   range, and calculates the cavity length from the identified
%   peaks.
%

tol = 3/100;        % Tolerance used for identifying the peaks,
                    % which is a percentage of the range (max-min)
correction_factor_lower = -0.25;
correction_factor_upper = -0.15;
%correction_factor_upper = -0.2;
pressure_list = pressure_list(:);
n_press = length(pressure_list);
pref_fixed_range = 'Yes';
%pause_time = 0;
for k = 1:n_press

    % load the raw data
    file_name = [num2str(pressure_list(k)) '.' file_ext];
    data = load(file_name);
    wavelength = data(:,1);
    intensity = data(:,2);

% Specify the wavelength range
    if (~strcmp(pref_fixed_range,'Yes') || (k == 1))
        x(1)  = 724.34;
        x(2)  = 970.11;
        xmin = min(x);
        xmax = max(x);
        lambda_min = find(wavelength>=xmin,1,'first');
        lambda_max = find(wavelength>=xmax,1,'first');
        wavelength = wavelength(lambda_min:lambda_max);
        intensity = intensity(lambda_min:lambda_max);
    else
        x(1)  = x(1)+correction_factor_lower;
        x(2)  = x(2)+correction_factor_upper;
        xmin = min(x);
        xmax = max(x);
        lambda_min = find(wavelength>=xmin,1,'first');
        lambda_max = find(wavelength>=xmax,1,'first');
        wavelength = wavelength(lambda_min:lambda_max);
        intensity = intensity(lambda_min:lambda_max);
    end

    delta = (max(intensity)-min(intensity))*tol;
```

```
    [peaks_index,valleys] = peakdet(intensity,delta);
    peaks = wavelength(peaks_index(:,1));
    n_peaks = size(peaks,1);
    for kk = 1:n_peaks
        index_min = max(peaks_index(kk,1)-span,1);
        index_max = min(peaks_index(kk,1)+span,length(wavelength));
        lambda = wavelength(index_min:index_max);
        amp = intensity(index_min:index_max);
        peak_rough = peaks(kk,1);
        p = polyfit(lambda-peak_rough,amp,2);
        peak_offset = -p(2)/2/p(1);
        peaks(kk,1) = peak_rough+peak_offset;
        peaks(kk,2) = polyval(p,peak_offset);
    end

% calculate the cavity length
    n_peaks = size(peaks,1);
    L_sum = 0;
    for m = 1:n_peaks-1
       L_sum = L_sum+1/(1/peaks(m,1)-1/peaks(m+1,1))/2/10^9;
    end
    cavity(k) = L_sum/(n_peaks-1);
end
cavity = cavity(:);
p_res = polyfit(pressure_list,cavity,1);

%   Calcualte R-squared
cavity_fitted = polyval(p_res,pressure_list);
cavity = cavity(:);
cavity_fitted = cavity_fitted(:);
R2 = 1 - sum((cavity-cavity_fitted).^2) / sum((cavity-
mean(cavity)).^2);

%   Write the calculation results to an external file
if (nargin > 3)
    fid = fopen(output_file,'w');
    for k = 1:n_press

fprintf(fid,'%10.4f\t%10.5f\t\n',pressure_list(k),cavity(k)*1e6);
    end
    fclose(fid);
end

end
```

A.3. Matlab codes for one peak tracing to retrieve cavity lengths from multi-cavity optical sensor

File name: USB4000_one_peak_method_code_Ver8.m

```
clc; clear all; close all

tic
%% General parameters
    pressure_list = 1:16;
    FFT_peak_tolerance = 0.12;      % Tolerance for peak finding
from FFT result
    added_points = 100;    % Number of added point for interpolation

% Short cavity - parameters
    tolerance1 = 0.3;     % Tolerance for peak finding from the
shoter cavity spectrum
    bandwidth1 = 12e3;
    span1 = 45;           % Peak finding span for the shorter cavity
    pause_time1 = 0.0;      % Pause after showing fitting curve for
the shorter cavity
    lambda_min1_ini = 704.01;  % Lower bound of wavelength for the
shorter cavity
    lambda_max1_ini = 995.01;  % Upper bound of wavelength for the
shorter cavity
    lambda_min1_fin = 704.01;  % Lower bound of wavelength for the
shorter cavity
    lambda_max1_fin = 995.01;  % Upper bound of wavelength for the
shorter cavity
    estimated_peak1 = 104790;

% Long cavity - parameters
    tolerance2 = 0.2;     % Tolerance for peak finding from the
longer cavity spectrum
    bandwidth2 = 11.75e3;
    span2 = 20;           % Peak finding span for the longer cavity
    pause_time2 = 0.0;      % Pause after showing fitting curve for
longer cavity
    lambda_min2_ini = 704.01;    % Lower bound of wavelength for the
longer cavity
    lambda_max2_ini = 995.01;    % Upper bound of wavelength for the
longer cavity
    lambda_min2_fin = 704.01;    % Lower bound of wavelength for the
longer cavity
    lambda_max2_fin = 995.01;    % Upper bound of wavelength for the
longer cavity
    estimated_peak2 = 954943;

% List of data set
    L1 = transpose(pressure_list);
    L2 = transpose(pressure_list);
    number_pressure_list = length(pressure_list);
    file_ext = 'ProcSpec';

%% Km finding process

% Import spectrum from the first data set for choosing a km
```

```
    file_name = [num2str(pressure_list(5)) '.' file_ext];
    data = load(file_name);
    wavelength = data(:,1);
    intensity = data(:,2);

% Plot the data
    fig_h1 = figure('Position', [10 425 600 295]);
    figure(fig_h1)
    plot(wavelength,intensity,'b-','LineWidth',2);
    xlabel('Wavelength (nm)')
    ylabel('Intensity')
    title('Original data')

% Interpolation of the signal
    wavenumber = 1./wavelength;
    intensity = intensity-mean(intensity); % Eliminating DC
component from the spectrum
    wavenumber_max = max(wavenumber);
    wavenumber_min = min(wavenumber);
    number_point = (added_points+1).*(length(wavenumber)-1)+1;
    wavenumber_interpolated =
linspace(wavenumber_max,wavenumber_min,number_point); % many x
values for plotting
    intensity_interpolated =
spline(wavenumber,intensity,wavenumber_interpolated); % generate y
values based on spline interpolation
    wavenumber_delta = wavenumber_interpolated(1)-
wavenumber_interpolated(2);
    Fs = 1/wavenumber_delta;
% Plotting of the interpolated spectrum
    fig_h2 = figure('Position', [10 425 600 295]);
    figure(fig_h2)
    plot(wavenumber_interpolated,intensity_interpolated,'g-
','LineWidth',2);
    xlabel('Wavenumber (nm-1)')
    ylabel('Intensity')
    title('Interpolated data')

%% Applying pre-filter to removed the first peak
   f_pre = 2.437e4/2 + 10e+3;                % Cutoff frequency
   [b,a] = butter(2,f_pre/(Fs/2),'high');    % Applying butterworth
filter
   intensity_interpolated = filtfilt(b,a,intensity_interpolated);

% FFT of the signal to find frequences from the spectrum
    WN_ITP = length(wavenumber_interpolated);             % Length
of signal
    NFFT1 = 2^nextpow2(WN_ITP);                           % Next
power of 2 from length of y
    Y1 = fft(intensity_interpolated,NFFT1)/WN_ITP;
    Y1_amp = (2*abs(Y1(1:NFFT1/2)));
    Fs = WN_ITP/(wavenumber_max-wavenumber_min);
```

```
    f1 = Fs/2*linspace(0,1,NFFT1/2);

% Plot FFT result
    fig_h3 = figure('Position', [630 425 600 295]);
    figure(fig_h3)
    plot(f1,Y1_amp)
%    set(gca,'xlim',[0 1e6])
    set(gca,'xlim',[0 1e6],'yscale','log')
    title('Amplitude Spectrum of wavenumber spectrum')
    xlabel('Optical frequency')
    ylabel('|Y(f)|')
    hold on
% Find peaks from FFT result and plot them
    delta = (max(Y1_amp)-min(Y1_amp))*FFT_peak_tolerance;
    peaks = peakdet(Y1_amp,delta);
    index = peaks(:,1);
    f1_peaks = f1(index);

    [cst_peak1 cst_index1] = min(abs(f1_peaks - estimated_peak1));
    [cst_peak2 cst_index2] = min(abs(f1_peaks - estimated_peak2));

    FFT_peaks1(1) = f1_peaks(cst_index1);
    FFT_peaks2(1) = f1_peaks(cst_index2);
    %FFT_peaks2(k) = f1_peaks(3);
    Y1_peaks = Y1_amp(index);

plot(f1_peaks,Y1_peaks,'rs','MarkerSize',4,'MarkerFaceColor','r')
    for n = 1:length(index)
        text(f1_peaks(n),Y1_peaks(n),num2str(f1_peaks(n)))
    end

%% Applying filter to the spectrum
    f0 = f1_peaks(cst_index1)/2;
    f_lb0 = f0*2 - bandwidth1/2;
    f_ub0 = f0*2 + bandwidth1/2;
    f1 = f1_peaks(cst_index2)/2;
    f_lb1 = f1*2 - bandwidth2/2;
    f_ub1 = f1*2 + bandwidth2/2;

    % Butterworth filter
    [z0,p0,k0] = butter(2,[f_lb0 f_ub0]/(Fs/2));
    [sos0,g0] = zp2sos(z0,p0,k0);
    INT_filtered1 = filtfilt(sos0,1,intensity_interpolated);
    [z1,p1,k1] = butter(2,[f_lb1 f_ub1]/(Fs/2));
    [sos1,g1] = zp2sos(z1,p1,k1);
    INT_filtered2 = filtfilt(sos1,1,intensity_interpolated);

%% Short cavity - Plot of filtered spectrum, peak finding, cavity
length calculation, and km calculation
    wavelength1 = 1./wavenumber_interpolated;
    intensity1 = INT_filtered1;
    wavelength_min1 = find(wavelength1>=lambda_min1_ini,1,'first');
```

```
    wavelength_max1 = find(wavelength1>=lambda_max1_ini,1,'first');
    wavelength1 = wavelength1(wavelength_min1:wavelength_max1);
    intensity1 = intensity1(wavelength_min1:wavelength_max1);

    delta1 = (max(intensity1)-min(intensity1))*tolerance1;
    [peaks_index1,valleys_index1] = peakdet(intensity1,delta1);
    peaks1 = wavelength1(peaks_index1(:,1));
    peak_intensity1 =intensity1(peaks_index1(:,1));
    n_peaks1 = size(peaks1,2);

    fig_h6 = figure('Position', [10 45 600 295]);
    figure(fig_h6)
    plot(wavelength1,intensity1,'b-','LineWidth',2)
    xlabel('Wavelength (nm)')
    ylabel('Intensity')
    hold on


plot(peaks1,peak_intensity1,'rs','MarkerSize',4,'MarkerFaceColor','r
')

    pre_L_sum1 = 0;
    for pp = 1:n_peaks1-1
        pre_L_sum1 = pre_L_sum1+1/(1/peaks1(1,pp)-
1/peaks1(1,pp+1))/2/10^3;
    end
    pre_measured_L1 = pre_L_sum1/(n_peaks1-1);

    km1_initial = pre_measured_L1./peaks1*1000;
    n_km1_initial = length(km1_initial);
    km1_final = km1_initial(floor(n_km1_initial/2));

%% Long cavity - Plot of filtered spectrum, peak finding, cavity
length calculation, and km calculation
    wavelength2 = 1./wavenumber_interpolated;
    intensity2 = INT_filtered2;
    wavelength_min2 = find(wavelength2>=lambda_min2_ini,1,'first');
    wavelength_max2 = find(wavelength2>=lambda_max2_ini,1,'first');
    wavelength2 = wavelength2(wavelength_min2:wavelength_max2);
    intensity2 = intensity2(wavelength_min2:wavelength_max2);

    delta2 = (max(intensity2)-min(intensity2))*tolerance2;
    [peaks_index2,valleys_index2] = peakdet(intensity2,delta2);
    peaks2 = wavelength2(peaks_index2(:,1));
    peak_intensity2 =intensity2(peaks_index2(:,1));
    n_peaks2 = size(peaks2,2);

    fig_h9 = figure('Position', [630 45 600 295]);
    figure(fig_h9)
    plot(wavelength2,intensity2,'g-','LineWidth',2)
    xlabel('Wavelength (nm)')
    ylabel('Intensity')
```

```
    hold on


plot(peaks2,peak_intensity2,'rs','MarkerSize',4,'MarkerFaceColor','r
')

    pre_L_sum2 = 0;
    for qq = 1:n_peaks2-1
        pre_L_sum2 = pre_L_sum2+1/(1/peaks2(1,qq)-
1/peaks2(1,qq+1))/2/10^3;
    end
    pre_measured_L2 = pre_L_sum2/(n_peaks2-1);

    km2_initial = pre_measured_L2./peaks2*1000;
    n_km2_initial = length(km2_initial);
    km2_final = km2_initial(floor(n_km2_initial/2));


%% One-peak tracking for caivity length tracing
for k = 1:number_pressure_list
% Importing spectrum data from measured files
    file_name = [num2str(pressure_list(k)) '.' file_ext];
    data = load(file_name);
    wavelength = data(:,1);
    intensity = data(:,2);

    fig_h1 = figure('Position', [10 425 600 295]);
    figure(fig_h1)
    plot(wavelength,intensity,'b-','LineWidth',2);
    xlabel('Wavelength (nm)')
    ylabel('Intensity')
    title('Original data')

%% Interpolation of the signal and plot
    wavenumber = 1./wavelength;
    intensity = intensity-mean(intensity); % Eliminating DC
component from the spectrum
    wavenumber_max = max(wavenumber);
    wavenumber_min = min(wavenumber);
    number_point = (added_points+1).*(length(wavenumber)-1)+1;
    wavenumber_interpolated =
linspace(wavenumber_max,wavenumber_min,number_point); % many x
values for plotting
    intensity_interpolated =
spline(wavenumber,intensity,wavenumber_interpolated); % generate y
values based on spline interpolation
    wavenumber_delta = wavenumber_interpolated(1)-
wavenumber_interpolated(2);
    Fs = 1/wavenumber_delta;

%% Plot the interpolated data (interpolated wavenumber vs.
intensity)
```

```
    fig_h2 = figure('Position', [10 425 600 295]);
    figure(fig_h2)
    plot(wavenumber_interpolated,intensity_interpolated,'g-
','LineWidth',2);
    xlabel('Wavenumber (nm-1)')
    ylabel('Intensity')
    title('Interpolated data')

%% Applying pre-filter to removed the first peak
   f_pre = 2.437e4/2 + 10e+3;              % Cutoff frequency
   [b,a] = butter(2,f_pre/(Fs/2),'high');  % Butterworth filter
   intensity_interpolated = filtfilt(b,a,intensity_interpolated);

%% FFT of the signal to find frequences from the spectrum
    WN_ITP = length(wavenumber_interpolated);             % Length
of signal
    NFFT1 = 2^nextpow2(WN_ITP);                           % Next
power of 2 from length of y
    Y1 = fft(intensity_interpolated,NFFT1)/WN_ITP;
    Y1_amp = (2*abs(Y1(1:NFFT1/2)));
    Fs = WN_ITP/(wavenumber_max-wavenumber_min);
    f1 = Fs/2*linspace(0,1,NFFT1/2);

%% Plot FFT result
    fig_h3 = figure('Position', [630 425 600 295]);
    figure(fig_h3)
    plot(f1,Y1_amp)
    set(gca,'xlim',[0 1e6],'yscale','log')
    title('Amplitude Spectrum of wavenumber spectrum')
    xlabel('Optical frequency')
    ylabel('|Y(f)|')
    hold on

%% Find peaks from FFT result & plot peaks
    delta = (max(Y1_amp)-min(Y1_amp))*FFT_peak_tolerance;
    peaks = peakdet(Y1_amp,delta);
    index = peaks(:,1);
    f1_peaks = f1(index);
    [cst_peak1 cst_index1] = min(abs(f1_peaks - estimated_peak1));
    [cst_peak2 cst_index2] = min(abs(f1_peaks - estimated_peak2));

    FFT_peaks1(k) = f1_peaks(cst_index1);
    FFT_peaks2(k) = f1_peaks(cst_index2);
    %FFT_peaks2(k) = f1_peaks(3);
    Y1_peaks = Y1_amp(index);


plot(f1_peaks,Y1_peaks,'rs','MarkerSize',4,'MarkerFaceColor','r')
    for n = 1:length(index)
        text(f1_peaks(n),Y1_peaks(n),num2str(f1_peaks(n)))
    end
```

```
%% Applying filter to the spectrum
    f0 = f1_peaks(cst_index1)/2;
    f_lb0 = f0*2 - bandwidth1/2;
    f_ub0 = f0*2 + bandwidth1/2;
    f1 = f1_peaks(cst_index2)/2;
    f_lb1 = f1*2 - bandwidth1/2;
    f_ub1 = f1*2 + bandwidth1/2;

    [z0,p0,k0] = butter(2,[f_lb0 f_ub0]/(Fs/2));              %
Applying Butterworth filter
    [sos0,g0] = zp2sos(z0,p0,k0);
    INT_filtered1 = filtfilt(sos0,1,intensity_interpolated);
    [z1,p1,k1] = butter(2,[f_lb1 f_ub1]/(Fs/2));              %
Applying Butterworth filter
    [sos1,g1] = zp2sos(z1,p1,k1);
    INT_filtered2 = filtfilt(sos1,1,intensity_interpolated);

%% Short cavity - finding rough cavity length and km using two-peak
method
    wavelength3 = 1./wavenumber_interpolated;
    intensity1 = INT_filtered1;
    wavelength_min1 = find(wavelength3>=lambda_min1_fin,1,'first');
    wavelength_max1 = find(wavelength3>=lambda_max1_fin,1,'first');
    wavelength3 = wavelength3(wavelength_min1:wavelength_max1);
    intensity1 = intensity1(wavelength_min1:wavelength_max1);

    delta1 = (max(intensity1)-min(intensity1))*tolerance1;
    [peaks_index1,valleys_index1] = peakdet(intensity1,delta1);
    peaks1 = wavelength3(peaks_index1(:,1));
    peak_intensity1 =intensity1(peaks_index1(:,1));
    n_peaks1 = size(peaks1,2);

    fig_h6 = figure('Position', [10 45 600 295]);
    figure(fig_h6)
    plot(wavelength3,intensity1,'b-','LineWidth',2)
    xlabel('Wavelength (nm)')
    ylabel('Intensity')
    hold on

plot(peaks1,peak_intensity1,'rs','MarkerSize',4,'MarkerFaceColor','r
')

    L_sum1 = 0;
    for ppp = 1:n_peaks1-1
        L_sum1 = L_sum1+1/(1/peaks1(1,ppp)-
1/peaks1(1,ppp+1))/2/10^3;
    end
    pre_measured_L1 = L_sum1/(n_peaks1-1);

    km1 = pre_measured_L1./peaks1*1000;
    [min_diff1, closest_km1_index] = min(abs(km1-km1_final));
    kk(k) = closest_km1_index;
```

```
%% Short cavity - Curve fitting to a chosen peak
    index_p_min1 = max(peaks_index1(kk(k),1)-span1,1);
    index_p_max1 =
min(peaks_index1(kk(k),1)+span1,length(wavelength3));
    lambda_p_1 = wavelength3(index_p_min1:index_p_max1);
    amp_p_1 = intensity1(index_p_min1:index_p_max1);
    peak_rough1 = peaks1(1,kk(k));
    p1 = polyfit(lambda_p_1-peak_rough1,amp_p_1,2);
    peak_offset1 = -p1(2)/2/p1(1);
    accu_peaks1(1,k) = peak_rough1+peak_offset1;
    accu_peaks1(2,k) = polyval(p1,peak_offset1);
    measured_L1(k) = km1_final*accu_peaks1(1,k)/1e3;
%% Short cavity - Ploting curve fitted curve with origianl data
points
    fig_h7 = figure('Position',[10 425 600 295]);

plot(lambda_p_1,amp_p_1,'bo','MarkerSize',6,'MarkerFaceColor','b');
    hold on
    plot(lambda_p_1,polyval(p1,lambda_p_1-peak_rough1),'m--
','LineWidth',2)
    xlabel('Wavelength (nm)')
    ylabel('Intensity')
    lhandle1 = vline(accu_peaks1(1,k),'r-
.',num2str(accu_peaks1(1,k)));
    set(lhandle1,'LineWidth',2);
    figure(fig_h6)
    hold on

plot(accu_peaks1(1,k),accu_peaks1(2,k),'rs','MarkerSize',4,'MarkerFa
ceColor','r')

text(accu_peaks1(1,k),accu_peaks1(2,k),num2str(accu_peaks1(1,k)))
    pause(pause_time1)
    fprintf(1,'%10.4f\n',accu_peaks1(1,k));
    close(fig_h7)

%% Long cavity - finding rough cavity length using two-peak method
    wavelength2 = 1./wavenumber_interpolated;
    intensity2 = INT_filtered2;
    wavelength_min2 = find(wavelength2>=lambda_min2_fin,1,'first');
    wavelength_max2 = find(wavelength2>=lambda_max2_fin,1,'first');
    wavelength2 = wavelength2(wavelength_min2:wavelength_max2);
    intensity2 = intensity2(wavelength_min2:wavelength_max2);
    % Peak finding
    delta2 = (max(intensity2)-min(intensity2))*tolerance2;
    [peaks_index2,valleys_index2] = peakdet(intensity2,delta2);
    peaks2 = wavelength2(peaks_index2(:,1));
    peak_intensity2 =intensity2(peaks_index2(:,1));
    n_peaks2 = size(peaks2,2);
    % Plotting
    fig_h9 = figure('Position', [630 45 600 295]);
    figure(fig_h9)
    plot(wavelength2,intensity2,'g-','LineWidth',2)
```

```
    xlabel('Wavelength (nm)')
    ylabel('Intensity')
    hold on

plot(peaks2,peak_intensity2,'rs','MarkerSize',4,'MarkerFaceColor','r
')

    L_sum2 = 0;

    for qqq = 1:n_peaks2-1
        L_sum2 = L_sum2+1/(1/peaks2(1,qqq)-
1/peaks2(1,qqq+1))/2/10^3;
    end
    pre_measured_L2 = L_sum2/(n_peaks2-1);

    km2 = pre_measured_L2./peaks2*1000;
    [min_diff2, closest_km2_index] = min(abs(km2-km2_final));
    rr(k) = closest_km2_index;
%% Long cavity - Curve fitting to a chosen peak
    index_p_min2 = max(peaks_index2(rr(k),1)-span2,1);
    index_p_max2 =
min(peaks_index2(rr(k),1)+span2,length(wavelength2));
    lambda_p_2 = wavelength2(index_p_min2:index_p_max2);
    amp_p_2 = intensity2(index_p_min2:index_p_max2);
    peak_rough2 = peaks2(1,rr(k));
    p2 = polyfit(lambda_p_2-peak_rough2,amp_p_2,2);
    peak_offset2 = -p2(2)/2/p2(1);
    accu_peaks2(1,k) = peak_rough2+peak_offset2;
    accu_peaks2(2,k) = polyval(p2,peak_offset2);
    measured_L2(k) = (km2_final*accu_peaks2(1,k)/1e3-
measured_L1(k))/1.52;

%% Ploting curve fitted curve with origianl data points
    fig_h10 = figure('Position',[630 425 600 295]);

plot(lambda_p_2,amp_p_2,'bo','MarkerSize',6,'MarkerFaceColor','b');
    hold on
    plot(lambda_p_2,polyval(p2,lambda_p_2-peak_rough2),'m--
','LineWidth',2)
    xlabel('Wavelength (nm)')
    ylabel('Intensity')
    lhandle1 = vline(accu_peaks2(1,k),'r-
.',num2str(accu_peaks2(1,k)));
    set(lhandle1,'LineWidth',2);
    figure(fig_h9)
    hold on

plot(accu_peaks2(1,k),accu_peaks2(2,k),'rs','MarkerSize',4,'MarkerFa
ceColor','r')

text(accu_peaks2(1,k),accu_peaks2(2,k),num2str(accu_peaks2(1,k)))
    pause(pause_time2)
```

```
    fprintf(1,'%10.4f\n',accu_peaks2(1,k));
    close(fig_h10)
    close all
    clc
    disp(['Percentage completed: '
num2str(100*(k/number_pressure_list)) '%']);
end

%% Short cavity - cavity length plot
    fig_h11 = figure('Position', [10 320 600 295]);
    figure(fig_h11)
    plot(L1/1e3,measured_L1,'bo','MarkerSize',5)
    hold on
    L1 = transpose(L1);
    fit_line_s = polyfit(L1/1e3,measured_L1,1);
    plot(L1/1e3,polyval(fit_line_s,L1/1e3),'r-','LineWidth',2)
    xlabel('Input cavity length (micron)')
    ylabel('Calculated cavity length (micron)')
    measured_L1_T = measured_L1(:);
    fitted_L1 = polyval(fit_line_s,L1/1e3);
    fitted_L1 = fitted_L1(:);
    R2_value_s = 1 - sum((measured_L1_T-
fitted_L1).^2)/sum((measured_L1_T-mean(measured_L1_T)).^2);

%% Long cavity - cavity length plot
    fig_h12 = figure('Position', [630 320 600 295]);
    figure(fig_h12)
    plot(L2/1e3,measured_L2,'bo','MarkerSize',5)
    hold on
    L2 = transpose(L2);
    fit_line_l = polyfit(L2/1e3,measured_L2,1);
    plot(L2/1e3,polyval(fit_line_l,L2/1e3),'r-','LineWidth',2)
    xlabel('Input cavity length (micron)')
    ylabel('Calculated cavity length (micron)')
    measured_L2_T = measured_L2(:);
    fitted_L2 = polyval(fit_line_l,L2/1e3);
    fitted_L2 = fitted_L2(:);
    R2_value_l = 1 - sum((measured_L2_T-
fitted_L2).^2)/sum((measured_L2_T-mean(measured_L2_T)).^2);

%% Elapsed time measurement
toc
t = toc;
```

A.4. LabView code for one-peak-tracing from SM130 spectrum

Front panel

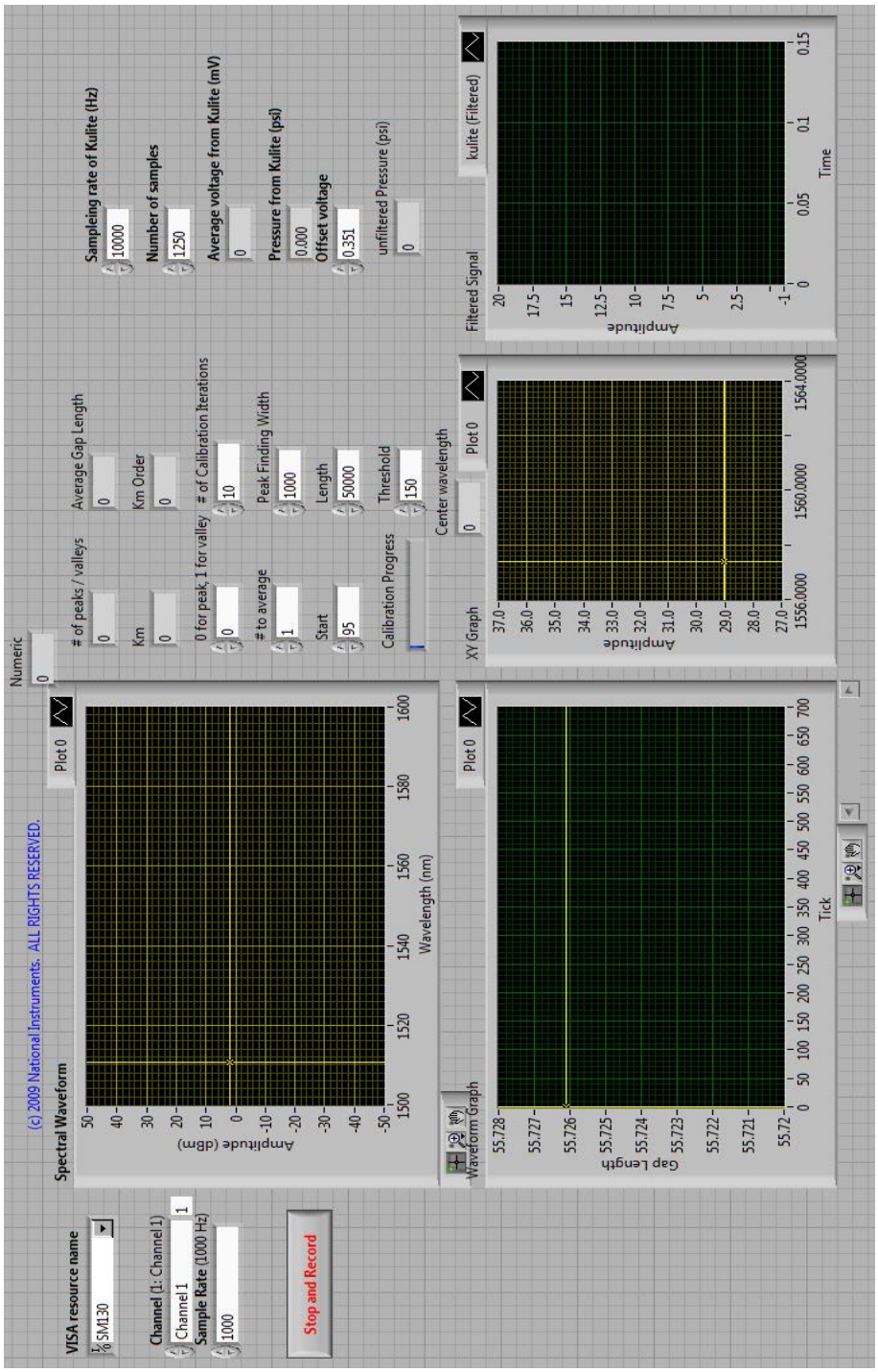

Block diagram

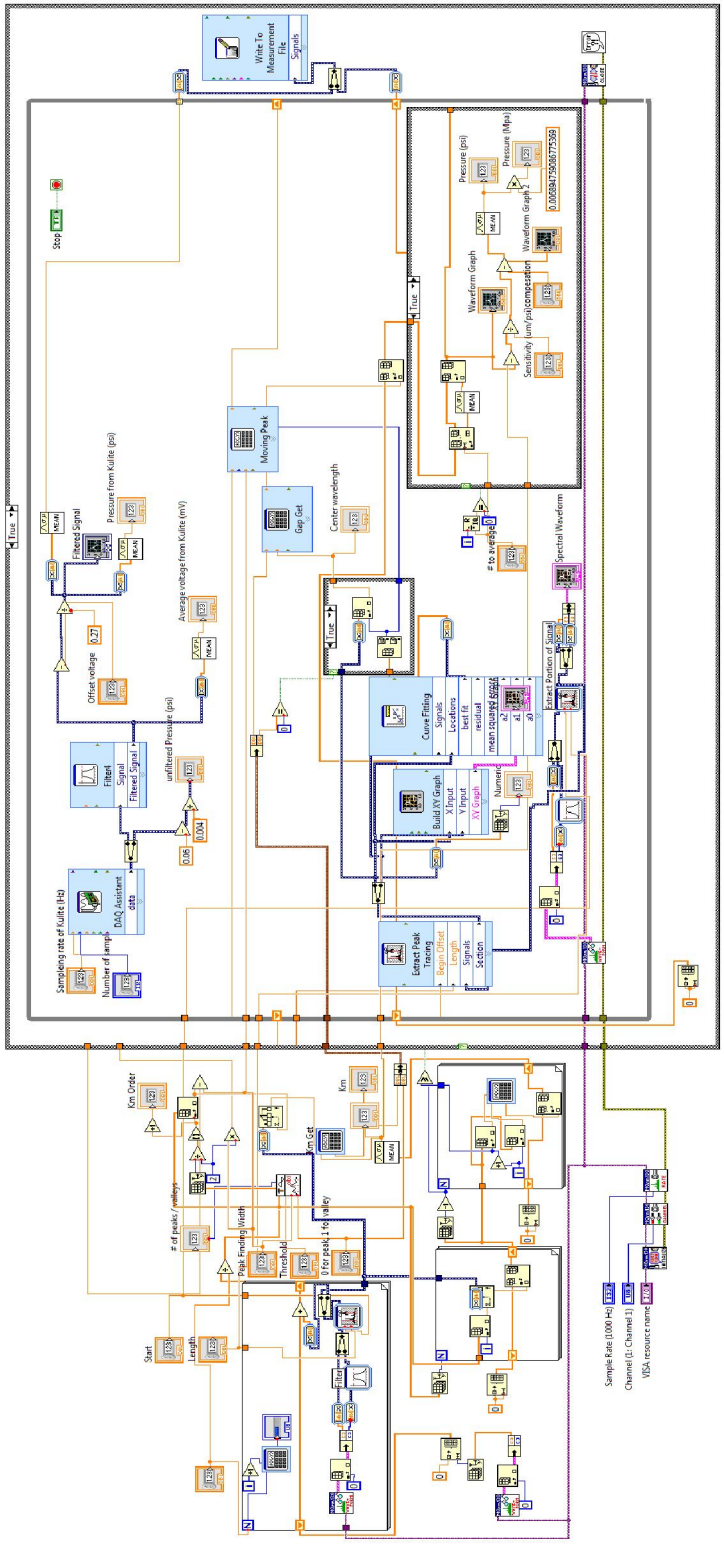

References

1. Y. Rao and D. A. Jackson, "Recent progress in fibre optic low-coherence interferometry," Meas. Sci. Technol. **7**, 981–999 (1996).

2. Y. Rao, "Recent progress in fiber-optic extrinsic Fabry–Perot interferometric sensors," Opt. Fiber Technol. **12**, 227–237 (2006).

3. D. Donlagic and E. Cibula, "All-fiber high-sensitivity pressure sensor with SiO2 diaphragm," Opt. Lett. **30**, 2071–2073 (2005).

4. K. S. Chiang and B. C. B. Chu, "High-sensitivity pressure sensor using a shielded polymer-coated fiber Bragg grating," IEEE Photonics Technology Letters **13**, 618–619 (2001).

5. Y. Liu, Y. Ztiang, and K. Seng, "Simultaneous pressure and temperature measurement with polymer-coated fibre Bragg grating," Electronics Letters **36**, 564–566 (2000).

6. Y. Zhang, F. Dejun, Z. Liu, Z. Guo, X. Dong, K. S. Chiang, and C. B. C. B., "High-Sensitivity Pressure Sensor Using a Shielded Polymer-Coated Fiber Bragg Grating," IEEE Photonics Technology Letters **13**, 618–619 (2001).

7. H.-J. Sheng, M.-Y. Fu, T.-C. Chen, W.-F. Liu, and S.-S. Bor, "A Lateral Pressure Sensor Using a Fiber Bragg Grating," IEEE Photonics Technology Letters **16**, 1146–1148 (2004).

8. C. R. Dennison, P. M. Wild, D. R. Wilson, and P. a Cripton, "A minimally invasive in-fiber Bragg grating sensor for intervertebral disc pressure measurements," Measurement Science and Technology **19**, 085201 (2008).

9. D. Wang, M. Cao, C. Li, D. Li, Y. Chen, X. Xu, J. Xu, Y. Li, Z. Wan, and B. Wang, "Fiber Bragg Grating Liquid Level Sensor with Double Pressure and Temperature Sensitivities," Procedia Engineering **15**, 704–709 (2011).

10. W. Jung, S. Kim, K. Kim, E. Kim, and S. Kang, "High-sensitivity temperature sensor using a side-polished single-mode fiber covered with the polymer planar waveguide," IEEE Photonics Technology Letters **13**, 1209–1211 (2001).

11. R. Gibson, J. Kvavle, R. Selfridge, and S. Schultz, "Improved sensing performance of D-fiber/planar waveguide couplers.," Optics express **15**, 2139–2144 (2007).

12. X. Dai, S. J. Mihailov, and C. Blanchetiere, "Optical evanescent field waveguide Bragg grating pressure sensor," Optical Engineering **49**, 024401 (2010).

13. E. J. Eklund and A. M. Shkel, "Factors affecting the performance of micromachined sensors based on Fabry–Perot interferometry," Journal of Micromechanics and Microengineering **15**, 1770–1776 (2005).

14. J. H. Jerman, D. J. Clift, and S. R. Mallinson, "A Miniature Fabry-Perot Interferometer with a Corrugated Silicon Diaphragm Support," Sensors and Actuators A: Physical 140–144 (1990).

15. B. Halg, "A silicon pressure sensor with an interferometric optical readout," in *Solid-State Sensors and Actuators, 1991. Digest of Technical Papers, Tranducers `91., 1991 International Conference On* (1991), pp. 682–684.

16. R. a Wolthuis, G. L. Mitchell, E. Saaski, J. C. Hartl, and M. a Afromowitz, "Development of medical pressure and temperature sensors employing optical spectrum modulation," IEEE transactions on bio-medical engineering **38**, 974–81 (1991).

17. Y. Kim and D. Neikirk, "Micromachined Fabry-Perot Cavitv Pressure Transducer," IEEE PHO'JDMCS TECHNOLOGY LETTERS **7**, 1471–1473 (1995).

18. V. Bhatiay, K. A. Murphyz, R. O. Clausy, M. E. Jonesz, J. L. Gracez, T. A. Tranz, and J. A. Greenez, "Optical fibre based absolute extrinsic Fabry–Perot interferometric sensing system," Meas. Sci. Technol. **7**, 58–61 (1996).

19. J. Han, "Novel fabrication and characterization method of Fabry–Perot microcavity pressure sensors," Sensors And Actuators **75**, 168–175 (1999).

20. E. Cibula and D. Donlagić, "Miniature fiber-optic pressure sensor with a polymer diaphragm," Appl. Opt. **44**, 2736–2744 (2005).

21. X. Wang, J. Xu, Y. Zhu, K. L. Cooper, and A. Wang, "All-fused-silica miniature optical fiber tip pressure sensor.," Optics letters **31**, 885–887 (2006).

22. K. L. Cooper and G. R. Pickrell, "High-temperature fiber-tip pressure sensor," Journal of Lightwave Technology **24**, 861–869 (2006).

23. É. Pinet, E. Cibula, and D. Đonlagić, "Ultra-miniature all-glass Fabry-Pérot pressure sensor manufactured at the tip of a multimode optical fiber," in *Proceedings of SPIE* (2007), p. 67700U–1~67700U–8.

24. Y. Ge, M. Wang, and H. Yan, "Optical MEMS pressure sensor based on a mesa-diaphragm structure.," Optics express **16**, 21746–52 (2008).

25. Y. Ge, M. Wang, X. Chen, and H. Rong, "An optical MEMS pressure sensor based on a phase demodulation method," Sensors and Actuators A: Physical **143**, 224–229 (2008).

26. E. Cibula, S. Pevec, B. Lenardic, E. Pinet, and D. Donlagic, "Miniature all-glass robust pressure sensor.," Optics express **17**, 5098–106 (2009).

27. J. Ma, J. Ju, L. Jin, and W. Jin, "A Compact Fiber-tip Micro-cavity Sensor for High Pressure Measurement," IEEE Photonics Technol. Lett. **23**, 1561–1563 (2011).

28. D. Chen, X. Cheng, and H. Y. Tam, "Hydrostatic pressure sensor based on a gold-coated thin-core fiber modal interferometer and ripple shift measurement," Optics Communications (2012).

29. D. Wu, T. Zhu, G.-Y. Wang, J.-Y. Fu, X.-G. Lin, and G.-L. Gou, "Intrinsic fiber-optic Fabry–Perot interferometer based on arc discharge and single-mode fiber," Applied Optics **52**, 2670 (2013).

30. Y. Wang, D. N. Wang, C. Wang, and T. Hu, "Compressible fiber optic micro-Fabry-Pérot cavity with ultra-high pressure sensitivity," Optics Express **21**, 14084 (2013).

31. K. Totsu, Y. Haga, and M. Esashi, "Ultra-miniature fiber-optic pressure sensor using white light interferometry," J. Micromech. Microeng. **15**, 71–75 (2005).

32. E. S. Olson, "Observing middle and inner ear mechanics with novel intracochlear pressure sensors," J. Acoust. Soc. Am. **103**, 3445–3463 (1998).

33. S. Nesson, M. Yu, X. Zhang, and A. H. Hsieh, "Miniature fiber optic pressure sensor with composite polymer-metal diaphragm for intradiscal pressure measurements," J. Biomed. Opt. **13**, 044040 (2008).

34. O. Tohyama, M. Kohashi, M. Sugihara, and H. Itoh, "A fiber-optic pressure microsensor for biomedical application," Sensors And Actuators **66**, 150–154 (1998).

35. R. Melamud, A. a. Davenport, G. C. Hill, I. H. Chan, F. Declercq, P. G. Hartwell, and B. L. Pruitt, "Development of an SU-8 fabry-perot blood pressure sensor," 18th IEEE International Conference on Micro Electro Mechanical Systems, 2005. MEMS 2005. 810–813 (2005).

36. W. N. MacPherson, J. M. Kilpatrick, J. S. Barton, and J. D. C. Jones, "Miniature fiber optic pressure sensor for turbomachinery applications," Rev. Sci. Instrum. **70**, 1868–1874 (1999).

37. M. J. Gander, W. N. MacPherson, J. S. Barton, R. L. Reuben, J. D. C. Jones, R. Stevens, K. S. Chana, S. J. Anderson, and T. V. Jones, "Embedded micromachined fiber-optic Fabry-Perot pressure sensors in aerodynamics applications," IEEE Sens. J. **3**, 102–107 (2003).

38. J. Zhou, S. Dasgupta, H. Kobayashi, J. M. Wolff, H. E. Jackson, and J. T. Boyd, "Optically interrogated MEMS pressure sensors for propulsion applications," Optical Engineering **40**, 598 (2001).

39. J. Xu, X. Wang, K. L. Cooper, and A. Wang, "Miniature all-silica fiber optic pressure and acoustic sensors," Opt. Lett. **30**, 3269–3271 (2005).

40. F. Guo, T. Fink, M. Han, L. Koester, J. Turner, and J. Huang, "Fabry–Perot interferometric fiber-tip sensor based on a thin silver diaphragm," Optics Letters **37**, 1505–1507 (2012).

41. P. Morris, A. Hurrell, A. Shaw, E. Zhang, and P. Beard, "A Fabry–Pérot fiber-optic ultrasonic hydrophone for the simultaneous measurement of temperature and acoustic pressure," Journal of the Acoustical Society of America **125**, 3611–3622 (2009).

42. M. G. Diaphragm, J. Ma, H. Xuan, H. L. Ho, W. Jin, Y. Yang, and S. Fan, "A Fiber-Optic Fabry-Perot Acoustic Sensor with Multi-Layer Graphene Diaphragm," 1–4 (2013).

43. W. Parkes, V. Djakov, J. S. Barton, S. Watson, W. N. MacPherson, J. T. M. Stevenson, and C. C. Dunare, "Design and fabrication of dielectric diaphragm pressure sensors for applications to shock wave measurement in air," Journal of Micromechanics and Microengineering **17**, 1334–1342 (2007).

44. N. Wu, W. Wang, Y. Tian, X. Zou, M. Maffeo, J. Chen, and X. Wang, "Low-cost rapid miniature optical pressure sensors for blast wave measurements," Optics express **19**, 10797–10804 (2011).

45. N. Wu, X. Zou, Y. Tian, J. Fitek, M. Maffeo, C. Niezrecki, J. Chen, and X. Wang, "An ultra-fast fiber optic pressure sensor for blast event measurements," Measurement Science and Technology **23**, 055102 (2012).

46. X. Zou, N. Wu, Y. Tian, C. Niezrecki, J. Chen, and X. Wang, "Rapid miniature fiber optic pressure sensors for blast wave measurements," Optics and Lasers in Engineering **51**, 134–139 (2013).

47. B. Qi, "Fiber optic pressure and temperature sensors for oil down hole application," Proceedings of SPIE **4578**, 182–190 (2002).

48. S. Aref, H. Latifi, M. Zibaii, and M. Afshari, "Fiber optic Fabry–Perot pressure sensor with low sensitivity to temperature changes for downhole application," Opt. Commun. **269**, 322–330 (2007).

49. T. Bae, R. A. Atkins, H. F. Taylor, and W. N. Gibler, "An Interferometric Fiber Optic Sensor Embedded in a Spark Plug for In-Cylinder Pressure Measurement in Engines," IEEE 419–422 (2002).

50. D. C. Abeysinghe, S. Dasgupta, H. E. Jackson, and J. T. Boyd, "Novel MEMS pressure and temperature sensors fabricated on optical fibers," J. Micromech. Microeng. **229**, 229–235 (2002).

51. Y. Zhu and A. Wang, "Miniature fiber-optic pressure sensor," IEEE Photonics Technology Letters **17**, 447–449 (2005).

52. W. Wang, N. Wu, Y. Tian, C. Niezrecki, and X. Wang, "Miniature all-silica optical fiber pressure sensor with an ultrathin uniform diaphragm," Optics express **18**, 9006–9014 (2010).

53. F. Interferometer, W. Wang, Q. Yu, F. Li, X. Zhou, and X. Jiang, "Temperature-Insensitive Pressure Sensor Based on All-Fused-Silica Extrinsic Fabry – Pérot Optical," IEEE Sens. J. **12**, 2425–2429 (2012).

54. G. Voskerician, "Biocompatibility and biofouling of MEMS drug delivery devices," Biomaterials **24**, 1959–1967 (2003).

55. M. Stangegaard, Z. Wang, J. P. Kutter, M. Dufva, and a. Wolff, "Whole genome expression profiling using DNA microarray for determining biocompatibility of polymeric surfaces," Molecular BioSystems **2**, 421 (2006).

56. G. M. Whitesides, "The origins and the future of microfluidics.," Nature **442**, 368–73 (2006).

57. T. Li and Z. Suo, "Ductility of thin metal films on polymer substrates modulated by interfacial adhesion," International Journal of Solids and Structures **44**, 1696–1705 (2007).

58. J. Ma, W. Tang, and W. Zhou, "Optical-fiber sensor for simultaneous measurement of pressure and temperature: analysis of cross sensitivity," Appl. Opt. **35**, 5206–5209 (1996).

59. J. Xu, X. Wang, K. L. Cooper, G. R. Pickrell, and A. Wang, "Miniature temperature-insensitive Fabry–Pérot fiber-optic pressure sensor," IEEE Photonics Technol. Lett. **18**, 1134–1136 (2006).

60. Q. Wang, L. Zhang, C. Sun, and Q. Yu, "Multiplexed fiber-optic pressure and temperature sensor system for down-hole measurement," IEEE Sens. J. **8**, 1879–1883 (2008).

61. N. Hodgson and H. Weber, *Optical Resonators: Fundamentals, Advanced Concepts and Applications* (Springer, 1977).

62. J. Ma, W. Jin, H. L. Ho, and J. Y. Dai, "High-sensitivity fiber-tip pressure sensor with graphene diaphragm.," Optics letters **37**, 2493–5 (2012).

63. R. A. Wolthuis, G. L. Mitchell, E. Saaski, J. C. Hartl, and M. A. Afromowitz, "Development of medical pressure and temperature sensors employing optical spectrum modulation," IEEE Trans. Biomed. Eng. **38**, 974–981 (1991).

64. G. Hill, R. Melamud, A. Davenport, F. Declercq, I. Chan, P. Hartwell, and B. Pruitt, "SU-8 MEMS Fabry-Perot pressure sensor," Sens. Actuators, A **138**, 52–62 (2007).

65. W. Wang, N. Wu, Y. Tian, X. Wang, C. Niezrecki, and J. Chen, "Optical pressure/acoustic sensor with precise Fabry-Perot cavity length control using angle polished fiber," Opt. Express **17**, 16613–16618 (2009).

66. S. Watson, M. J. Gander, W. N. MacPherson, J. S. Barton, J. D. C. Jones, T. Klotzbuecher, T. Braune, J. Ott, and F. Schmitz, "Laser-machined fibers as Fabry-Perot pressure sensors," Appl. Opt. **45**, 5590–5596 (2006).

67. F. Xu, D. Ren, X. Shi, C. Li, W. Lu, L. Lu, L. Lu, and B. Yu, "High Sensitivity Fabry-Perot Interferometric Pressure Sensor Based on a Nano-thick Silver Diaphragm," Optics letters **37**, 133–135 (2012).

68. K. T. V. Grattan and B. T. Meggitt, *Optical Fiber Sesnor Technology*, First edit (Chapman & Hall, 1995), p. 499.

69. B. Qi, G. R. Pickrell, J. C. Xu, P. Zhang, Y. H. Duan, W. Peng, Z. Y. Huang, W. Huo, H. Xiao, R. G. May, and A. Wang, "Novel data processing techniques for dispersive white light interferometer," Opt. Eng. **42**, 3165–3171 (2003).

70. F. Shen and A. Wang, "Frequency-estimation-based signal-processing algorithm for white-light optical fiber Fabry-Perot interferometers.," Applied optics **44**, 5206–14 (2005).

71. T. Liu and G. F. Fernando, "A frequency division multiplexed low-finesse fiber optic Fabry–Perot sensor system for strain and displacement measurements," Review of Scientific Instruments **71**, 1275 (2000).

72. Y. Jiang, "Fourier Transform White-Light Interferometry for the Measurement of Fiber-Optic Extrinsic Fabry–Pérot Interferometric Sensors," IEEE Photonics Technology Letters **20**, 75–77 (2008).

73. T. Liu, G. F. Fernando, Y. J. Rao, D. A. Jackson, L. Zhang, and I. Bennion, "Simultaneous strain and temperature measurements in composites using a multiplexed fiber Bragg grating sensor and an extrinsic Fabry-Perot sensor," in *Proc. of SPIE* (1977), Vol. 3042, pp. 203–212.

74. S. Pevec and D. Donlagic, "Miniature all-fiber Fabry–Perot sensor for simultaneous measurement of pressure and temperature," Appl. Opt. **51**, 4536–4541 (2012).

75. R. Melamud, A. A. Davenport, G. C. Hill, I. H. Chan, F. Declercq, P. G. Hartwell, B. L. Pruitt, S. De Microtechnique, E. Polytechnique, and F. De Lausanne, "Development of an SU-8 Fabry-Perot blood pressure sensor," in *Micro Electro Mechanical System, 2005. MEMS 2005. 18th IEEE International Conference* (2005), pp. 810–813.

76. W. A. Brantley, "Calculated elastic constants for stress problems associated with semiconductor devices," Jour **44**, 534–535 (1973).

77. C. Coefficients, "Young's Modulus, Shear Modulus, and Poisson's Ratio in Silicon and Germanium," Journal of Applied Physics **36**, 163–156 (1965).

78. V. L. Streeter and E. B. Wylie, *Fluid Mechanics*, 8th ed. (McGraw-Hill, 1985), pp. 351–353.

79. R. Whiting, M. Angadi, and S. Tripathi, "Evaluation of elastic moduli in thin-film/substrate systems by the two-layer vibrating reed method," Materials Science and Engineering B **30**, 35–38 (1995).

80. T. Liu, G. F. Fernando, Z. Y. Zhang, and K. T. V. Grattan, "Simultaneous strain and temperature measurements in composites using extrinsic Fabry–Perot interferometric and intrinsic rare-earth doped fiber sensors," Sensors and Actuators A: Physical **80**, 208–215 (2000).

81. K. Bremer, E. Lewis, B. Moss, G. Leen, S. Lochmann, and I. Mueller, "Conception and preliminary evaluation of an optical fibre sensor for simultaneous measurement of pressure and temperature," J. Phys. Conf. Ser. **178**, 012016 (2009).

82. S. M. Kim and S. Kang, "Replication qualities and optical properties of UV-moulded microlens arrays," J. Phys. D: Appl. Phys. **36**, 2451–2456 (2003).

83. M. Tanigami, S. Ogata, S. Aoyama, T. Yamashita, and K. Imanaka, "Low-wavefront aberration and high-temperature stability molded micro Fresnel lens," IEEE Photonics Technol. Lett. **1**, 384–385 (1989).

84. M. V. Kunnavakkam, F. M. Houlihan, M. Schlax, J. a. Liddle, P. Kolodner, O. Nalamasu, and J. a. Rogers, "Low-cost, low-loss microlens arrays fabricated by soft-lithography replication process," Applied Physics Letters **82**, 1152 (2003).

85. P. Dannberg, L. Erdmann, A. Krehl, C. Wachter, and A. Brauer, "Integration of optical interconnects and optoelectronic elements on wafer-scale," Mater. Sci. Semicond. Process. **3**, 437–441 (2000).

86. J. Lim, M. Choi, H. Kim, and S. Kang, "Fabrication of hybrid microoptics using UV imprinting process with shrinkage compensation method," Jpn. J. Appl. Phys. **47**, 6719–6722 (2008).

87. S. Ahn, M. Choi, H. Bae, J. Lim, H. Myung, H. Kim, and S. Kang, "Design and fabrication of micro optical film by ultraviolet roll imprinting," Jpn. J. Appl. Phys. **46**, 5478–5484 (2007).

88. B. Kim, M. Choi, H. Kim, J. Lim, and S. Kang, "Elimination of flux loss by optimizing the groove angle in modified Fresnel lens to increase illuminance uniformity, color uniformity and flux efficiency in LED illumination," Opt. Express **17**, 17916–27 (2009).

89. B. Arkles, "Tailoring surfaces with silanes," Chemtech **7**, 766–778 (1977).

90. J. Lee, S. Park, K. Choi, and G. Kim, "Nano-scale patterning using the roll typed UV-nanoimprint lithography tool," Microelectron. Eng. **85**, 861–865 (2008).

91. J. Duparré, P. Dannberg, P. Schreiber, A. Bräuer, and A. Tünnermann, "Artificial apposition compound eye fabricated by micro-optics technology," Appl. Opt. **43**, 4303–4310 (2004).

92. X. Hu, D. Liang, J. Zeng, and G. Lu, "A long period grating for simultaneous measurement of temperature and strain based on support vector regression," J. Intell. Mater. Syst. Struct. **21**, 955–959 (2010).

93. M. N. Inci, S. R. Kldd, J. S. Barton, and J. D. C. Jones, "Fabrication of single-mode fibre optic Fabry-Perot interferometers using fusion spliced titanium dioxide optical coatings," Meas. Sci. Technol. **3**, 678–684 (1992).

94. H. Y. Choi, K. S. Park, S. J. Park, U.-C. Paek, B. H. Lee, and E. S. Choi, "Miniature fiber-optic high temperature sensor based on a hybrid structured Fabry-Perot interferometer.," Optics letters **33**, 2455–7 (2008).

95. C. E. Lee, W. N. Gibler, R. a. Atkins, and H. F. Taylor, "In-line fiber Fabry-Perot interferometer with high-reflectance internal mirrors," Journal of Lightwave Technology **10**, 1376–1379 (1992).